Effect of cathode microstructure on erosion of copper cathodes-an experimental study

Lakshminarayana Rao

Department of Chemical Engineering

McGill University, Montreal

September 2007

A thesis submitted to McGill University in partial fulfillment of the requirements of the degree of Doctor of Philosophy

Your file Votre référence
ISBN: 978-0-494-50964-7
Our file Notre référence
ISBN: 978-0-494-50964-7

Dedicated To
Amma - Appa

Copyright letters

I, Dr. Richard J. Munz, hereby give copy right clearance of the following papers, of which I am a co-author, in the doctoral thesis of Lakshminarayana Rao.

- Chapter 4: **Rao, L** and Munz, R. J. Arc velocity and erosion studies on annealed and hard drawn copper cylinders in a magnetically rotated atmospheric pressure arc. *Journal of Physics D: Applied Physics.*

- Chapter 5: **Rao, L** and Munz, R. J. Effect of surface roughness on erosion rates of pure copper coupons in pulsed vacuum arc system *Journal of Physics D: Applied Physics.*

- Chapter 6: **Rao, L.,** Munz, R. J. and Meunier, J-L. Vacuum arc velocity and erosion rate measurements on nanostructured plasma and HVOF spray coatings. *Journal of Physics D: Applied Physics*, **40** (14), 4192-4201 (2007).

- Chapter 7: **Rao, L** and Munz, R. J. Effect of cathode microstructure on arc velocity and erosion rate of cold cathodes in a magnetically rotated atmospheric pressure arc. *Journal of Physics D: Applied Physics.*

- Chapter 8: D'Sa K., **Rao, L** and Munz, R. J. Effect of cathode microstructure on arc velocity and erosion rate of cold-sprayed copper cathodes in a magnetically rotated atmospheric pressure arc *Journal of Thermal Spray Technology.*

- Chapter 9: **Rao, L.,** Munz, R. J. and Coulombe, S. Observation of atmospheric pressure arc on a cold cathode *Applied Physics Letters.*

- Chapter 10: **Rao, L.,** Reddy N.K., Coulombe, S., Meunier, J-L., and Munz, R. J. Carbon nanotubes as nanoparticles collector. *Journal of Nanoparticle Research*, **9** (4) , 689-695 (2007).

Prof. Richard J. Munz
Department of Chemical Engineering
McGill University
Montreal, Quebec, Canada.

I, Dr. Jean-Luc Meunier, hereby give copy right clearance of the following papers, of which I am a co-author, in the doctoral thesis of Lakshminarayana Rao.

- Chapter 6: **Rao, L.,** Munz, R. J. and Meunier, J-L. Vacuum arc velocity and erosion rate measurements on nanostructured plasma and HVOF spray coatings. *Journal of Physics D: Applied Physics*, **40** (14), 4192-4201 (2007).

- Chapter 10: **Rao, L.,** Reddy N.K., Coulombe, S., Meunier, J-L., and Munz, R. J. Carbon nanotubes as nanoparticles collector. *Journal of Nanoparticle Research*, **9** (4), 689-695 (2007).

Prof. Jean-Luc Meunier
Department of Chemical Engineering
McGill University
Montreal, Quebec, Canada.

I, Dr. Sylvain Coulombe, hereby give copy right clearance of the following papers, of which I am a co-author, in the doctoral thesis of Lakshminarayana Rao.

- Chapter 9: **Rao, L.,** Munz, R. J. and Coulombe, S. Observation of atmospheric pressure arc on a cold cathode *Applied Physics Letters.*

- Chapter 10: **Rao, L.,** Reddy N.K., Coulombe, S., Meunier, J-L., and Munz, R. J. Carbon nanotubes as nanoparticles collector. *Journal of Nanoparticle Research*, **9** (4) 689-695 (2007).

In addition, I also permit Lakshminarayana Rao to use figures 3.2 and 3.3, from my PhD thesis in his literature review chapter.

Prof. Sylvain Coulombe
Department of Chemical Engineering
McGill University
Montreal, Quebec, Canada.

I, Mr. Keith D'Sa, hereby give copy right clearance of the following papers, of which I am a co-author, in the doctoral thesis of Lakshminarayana Rao.

- Chapter 8: D'Sa K., **Rao, L** and Munz, R. J. Effect of cathode microstructure on arc velocity and erosion rate of cold-sprayed copper cathodes in a magnetically rotated atmospheric pressure arc *Journal of Thermal Spray Technology.*

Keith D'Sa
Undergraduate student
Department of Chemical Engineering
McGill University
Montreal, Quebec, Canada.

I, Mr. Naveen Krishna Reddy, hereby give copy right clearance of the following paper, of which I am a co-author, in the doctoral thesis of Lakshminarayana Rao.

- Chapter 10: **Rao, L.,** Reddy N.K., Coulombe, S., Meunier, J-L., and Munz, R. J. Carbon nanotubes as nanoparticles collector. *Journal of Nanoparticle Research,* **9** (4), 689-695 (2007).

Naveen Krishna Reddy
Graduate Student
Department of Chemische ing. Technieken
W. de Croylaan 46
B-3001 Heverlee, Leuven
Belgium.

Assignment of copyright - IOP Publishing Limited

Quoting from IOP website:

Author Rights

IOP grants the Named Authors the rights specified in 3.2 and 3.3. All such rights must be exercised for non-commercial purposes, if possible should display citation information and IOP's copyright notice, and for electronic use best efforts must be made to include a link to the on-line abstract in the Journal. Exercise of the rights in 3.3 additionally must not use the final published IOP format but the Named Author's own format (which may include amendments made following peer review).

The rights are

- To make copies of the Article (all or part) for teaching purposes
- **To include the Article (all or part) in a research thesis or dissertation;**
- To make oral presentation of the Article (all or part) and to include a summary and/or highlights of it in papers distributed at such presentations or in conference proceedings; and all proprietary rights other than copyright.

The additional rights are to

- Use the Article (all or part) without modification in personal compilations or publications of a Named Author's own works (provided not created by third party publisher);
- Include the Article (all or part) on a Named Author's own personal web site;
- Include the Article (all or part) on web sites of the Institution (including its repository) where a Named Author worked when research for the Article was carried out; and
- Include the Article (all or part) on third party web sites including e-print servers, but not on other publisher's web sites.

Abstract

The erosion of copper cathodes having different microstructures ranging from hundreds of nm to tens of μm were studied in both pulsed vacuum arcs and continuous running magnetically rotated atmospheric pressure arcs. Cathodes having different grain sizes were formed by various thermal spray and heat treatment methods namely, high-velocity oxygen fuel (HVOF) method, atmospheric pressure plasma spraying (PS), vacuum plasma spraying (VPS), cold spraying (CS) and annealing techniques.

The coatings produced were characterized for their chemical composition, oxide content, microstructure, porosity and thermal conductivity. Arc velocity and erosion measurements were performed on these cathodes. The results show that, the cathodes having smaller grain sizes show higher arc velocities and hence give lower erosion rates. Annealed HVOF, CS coatings and as-sprayed VPS coatings which had grains sizes from 4 to 0.9 μm gave up to 60% higher arc velocities and up to 70% lower erosion rates than Cu cathodes having grains sizes from 20 to 23 μm.

As sprayed HVOF and CS coatings spalled severely due to their poor coating adhesion strength, as well as low electrical and thermal conductivities. However annealing these coatings in inert atmosphere improved their properties and reduced spalling. Annealing conditions, which gave minimum or no spalling of the coatings, were determined. The effect of coating initial thickness on erosion rates was also determined.

Microstructural analysis of the coated cathodes after erosion experiments show that the initial grain size of the coatings remain intact even after erosion experiments.

Résumé

L'érosion créée par deux types d'arcs, pulsés sous vide et continus en rotation contrôlé magnétiquement à pression atmosphérique, sur des cathodes de cuivre dont la microstructure variait de quelques centaines de nanomètres jusqu'à quelques dizaines de micromètres fut étudiée. Les variations dans les tailles de grain des cathodes furent produites par différents types de pulvérisations thermiques et de traitements thermiques comme par exemple la méthode de projection HVOF (high-velocity oxygen fuel), la pulvérisation par plasma sous vide (VPS) et à pression atmosphérique (PS), la pulvérisation à froid (CS) et le recuit thermique.

Les paramètres des différents revêtements comme leur composition chimique, leur taux d'oxygène, leur microstructure, leur porosité et leur conductivité thermique furent caractérisés. La vitesse des arcs et le taux d'érosion furent mesurés sur ces cathodes. Les résultats montrent que pour les cathodes avec une taille de grain plus petite, la vitesse des arcs est plus grande et donc le taux d'érosion plus petit. Les revêtements HOVF et CS recuits de même que les revêtements VPS sans post-traitement ont des tailles de grain variant de 4 à 0,9 μm et donnent des vitesses d'arcs jusqu'à 60% plus grandes et jusqu'à 70% moins d'érosion comparativement aux cathodes de cuivre avec des tailles de grain de 20 à 23 μm.

À l'opposé, les revêtements HVOF et CS sans post-traitement sont sévèrement dénudés suite l'exposition aux arcs à cause de la faible force d'adhésion du revêtement et de la faiblesse de leurs conductivités électrique et thermique. Par contre, en recuisant ces couches sous atmosphère inerte, leurs propriétés s'améliorent et le dénudement est réduit. Nous avons aussi déterminé les conditions nécessaires de recuit pour obtenir un minimum ou une absence de dénudement du revêtement. L'effet de l'épaisseur initiale de la couche sur le taux d'érosion a aussi été déterminé.

L'analyse de la microstructure des cathodes avec revêtement après érosion montre que la taille initiale des grains demeure intacte même après l'érosion.

Acknowledgments

I am very grateful to all the people who have helped me through my studies during this PhD. I had 3 years of unlimited fun, both inside and outside lab, met incredible people and learnt a great deal of stuff. Thanks a lot for all of you who have shaped me to what I am today.

I would like to express my most sincere thanks to Professor Richard Munz, my research supervisor and my guru, for every help that he and his family has given to me. "I am very hard to convince", these were his words which inspired me when ever I planned an experiment. Dr. Munz, without your thoughtful guidance, discussions, support, ethics, honesty, kindness, and patience, this thesis would never have been written. I am proud, I could convince you and I am graduating under your supervision.

Many thanks are due to Professor Jean-Luc Meunier and Professor Sylvain Coulombe of plasma group McGill for their time in answering my most unusual questions. They had their doors open for me whenever I wanted (Although, Dr.Meunier would say I just have 2 minutes for you Rao and then spend the next 30 minutes discussing on my questions). I consider myself very lucky for having discussions with the two most fabulous people in the department. Thank you for all the help.

I would also like to sincerely thank Dr. Christian Moreau and Dr. Jean-Gabriel Legoux of Industrial Materials Institute, National Research Council, Canada, for their valuable suggestions and discussions throughout the project. Special thanks are due for Dr. M. Brochu of the Department of Mining and Materials Engineering Mcgill for answering all my unusual questions.

Many thanks to the non-academic staff that helped me carry out my research activities: Mr. Jean-Francois Alarie, Mr. Mario Lamontagne, Mr. Frederic Belval and Mr. Sylvain Belanger of IMI for help in preparation/characterization of coatings. I would also like to thank Mr. Frank Caporuscio, Mr. Luciano Cusmich, Mr. Gerald Lepkyj, the people in the

workshop, Mr. Alain Gagnon, Mr. Roberto Tariello, Mr. David, the ever smiling and helpful store keeper Ms. Melanie Gorman and analytical chemist Mr. Ranjan Roy for their technical support. I would also like to thank Ms. Monique Riendeau for X-ray diffraction training, and Ms. Helen Campbell for SEM training.

I thank the past and present members of the plasma group at McGill with special mention to Ian, Frederic, Ramona, Carole, Val, Joelle, Jason, Ed, Liping, Denis and Faysal for their company, advice and support. Special thanks to Frederic and Emilie Marion for their help in the abstract translation. Also, I would like to thank Jean-Michel, Leron and Keith for their help in numerous stages of my work.

I am very grateful to a have a wonderful company of friends both back home and here, who are with me in my joy and in my sorrow. Thank you guys, for bearing with me, especially Jittu, Naveena, Roman and Drac. Samir-Shivangi, thanks a lot for all the delicious paratas, you guys are wonderful hosts and you guys make me feel at home each time I visit you. Parmeet, Ashish, Luci, Shiva and Hemanth, I thank you for your company.

My parents, appa and amma who taught me how to dream and my sister, Lakshmi and Bhavaji, who encouraged me in every step I took towards making my dreams a reality, I cannot express in words how important you are for me.

Finally, I wish to acknowledge the financial support provided by the Natural Science and Engineering Research Council of Canada (NSERC), Fonds de Recherche sur la Nature et Technologies (FQRNT), and McGill internal fee waivers and funding.

Table of contents

List of figures

List of tables

Chapter 1 Introduction

1.1 Problem definition and project scope

Thermal plasma technology has proven to be integral in the development of new materials, surface and waste treatments [1]. Some current research in this field is focused on design and development of plasma torches/reactors with long electrode lifetimes and reproducible working conditions. Cathode erosion still limits the application of plasma technology to processes relying on torches with cold cathodes in tubular geometry. This erosion leads to relatively short operating life times of the cathode which in turn increases the operating costs of these processes via electrode cost and the cost of process down time to replace electrodes. Cathode erosion also contaminates the process stream by erosion products. Thus extensive research is dedicated to understanding and control cathode erosion.

Among the many factors which effect cathode erosion, arc residence time on the cathode (or arc velocity) and heat removal from the cathode are very important [2]. Higher arc velocities imply lower arc residence time, less melting and vaporization of the cathode material and hence lower erosion rates. Better cooling of the cathode also prevents excessive melting and vaporization of the cathode material. Arc velocity is in turn affected by the external magnetic field used to rotate the arc, the presence or absence of an oxidizing plasma gas, the O content and the microstructure of the cathode [2-10].

From anecdotal and some experimental evidence on cathode erosion, it has been hypothesized that cathode microstructure influences arc velocity and erosion rate [6-12]. To date no systematic study of cathode microstructure on arc velocity and erosion rate has been carried out. This study is the primary focus of this thesis.

In addition to high thermal and electrical conductivity of copper and its alloys, their ready availability, cheap material cost and ease of characterization make them very common cathode material. In this work, pure copper was chosen as the cathode material.

1.2 Thesis objectives

The overall objective of this thesis is to quantify the effect of microstructure on arc velocity and erosion rate of copper cathodes in atmospheric pressure and vacuum arc systems. Specifically, the following objectives were formulated

1. To modify existing apparatus and develop appropriate data logging and analysis tools to facilitate the erosion and velocity measurements required.
2. To form copper cathodes having different grain sizes ranging from nano meters to micro meters by thermal spray, cold spray and heat treatment techniques. To characterize these cathodes for their microstructure and thermal properties both before and after exposure to the arcs.
3. To conduct erosion studies on these cathodes using inert and reactive plasma gases.

1.3 Thesis outline

This thesis is a manuscript-based thesis and is divided into 12 chapters. Each journal article constitutes a chapter. Chapters 4 through 8 cover the experimental work on quantifying the effect of microstructure on arc velocities and erosion rate. Chapter 9 reports on additional experimental work conducted for better understanding of the magnetically rotated atmospheric pressure plasma arcs. Chapter 10 discusses the applications of erosion by-products.

Due to the nature of a manuscript-based thesis, care has been taken to minimize repetition and facilitate a fluent reading. At the beginning of each chapter a brief chapter introduction (before the "Abstract") is given before the manuscript is presented. Each chapter will have its pertaining literature review, introduction and references related to the subject discussed. In addition to the literature review presented in each chapter, a concise literature review (Chapter 3) has been added to introduce the reader to cathode erosion, arc velocity and factors affecting them. Literature review chapter is aimed at giving a clear understanding of the project and to fill the unavoidable gaps left by the compressed writing style necessary in manuscripts. Further, the integrity of the articles

has been preserved as much as possible and they are presented in full in their respective chapters. The thesis requirements established by McGill University mandate that a separate literature review chapter (Chapter 3) must be included, even in the case of manuscript-based thesis. Therefore, some overlap should be expected between the contents of Chapter 3 and the individual article introductions in Chapters 4 through 10.

The references contained in each manuscript are listed in numerical format at the end of each chapter and any other references used in this thesis are listed in brackets and numerically cited at the end of each chapter under "References". Finally, the experimental techniques and methodologies used in this work are described in each chapter as needed.

Chapter 1: Introduction

This chapter includes a thesis introduction, a definition of the scope of the thesis and a statement of objectives. The thesis outline is described.

Chapter 2: Contributions of authors

A description of the work carried out by the authors of the manuscripts is stated.

Chapter 3: Literature review

The literature review is divided into three major parts. First, a brief introduction on electric discharges, vacuum plasma and atmospheric pressure plasmas and their applications are given. Second, the arc-electrode phenomena are discussed without detailed mathematics. Cathode erosion is defined. In third and last section, factors affecting arc velocity are discussed in brief. A very brief discussion is given only on factors which are directly related to this work.

Chapter 4: Erosion of annealed and hard drawn Cu cathodes in continuous running atmospheric pressure magnetically rotated arcs

The experimental setup and the experimental procedure used to measure arc velocity and arc erosion in a continuous running atmospheric pressure, magnetically rotated arc

system is described. The arc erosion rates and arc velocity results for both hard drawn and annealed Cu tubes having grain sizes in tens of micrometers range are presented. The microstructural analysis of the hard drawn and annealed cathodes before and after erosion is presented. In this set of experiments, the external electrode was used as the cathode.

Chapter 5: Erosion of Cu cathodes with different surface roughness and surface pattern in pulsed vacuum arcs

Though surface roughness is not exactly microstructure, it is closely related. Hence the effect of surface roughness was studied in this chapter. Methods to form cathodes with different surface roughness and patterns are presented along with characterization of surface roughness using surface profilometer and scanning electron microscope. The vacuum erosion behavior of these cathodes is presented along with the analysis of the arc trace left on these cathodes. The results obtained are correlated to the nature of arc movement.

Chapter 6: Erosion of nanostructured Cu coatings in pulsed vacuum arcs

Characterization of the powders used to make thermal spray coatings is presented. The atmospheric pressure plasma spray (PS) and high velocity oxygen fuel (HVOF) techniques used to obtain nanostructured coatings are described. Characterization of the coatings formed by these two techniques for grain size, grain orientation, coating porosity and thermal conductivity are presented. The pulsed vacuum arc setup and experimental procedure used to obtain vacuum arc velocity and erosion rates of these coatings are described. The results obtained are compared with erosion rates of massive Cu with relatively large grain sizes. Crater size analysis on arc traces formed on nanostructured coatings is also presented. Microstructural changes of the coatings after erosion are given.

Chapter 7: Erosion of nanostructured Cu coatings in continuous running atmospheric pressure magnetically rotated arcs

Arc velocity and arc erosion rates of pure massive Cu cathodes having grains in the range of tens of micrometers in central cathode geometry are presented. Similar results are also presented for as-sprayed HVOF sprayed cathodes, vacuum plasma sprayed and annealed

HVOF coated cathodes having grain sizes ranging from hundreds of nano meters to a few micrometers. Effect of initial coating thickness on erosion rate is presented. The results obtained are compared with massive Cu cathodes. Microstructural changes of the coatings after erosion are given. In this set of experiments, the internal electrode was used as the cathode.

Chapter 8: Erosion of cold sprayed Cu coatings in continuous running atmospheric pressure magnetically rotated arcs

Characterization of the powders used to make cold spray coatings is presented. Cold spray technique used to obtain coatings having grains of a few micrometer size but free from oxide content are described. Characterization of the cold spray coatings for grain size, O content and coating porosity are presented. Arc velocity and arc erosion rates of these cold sprayed cathodes in their as-sprayed state and annealed state are presented. The results obtained are compared with massive Cu. Microstructural changes of the coatings after erosion are given. In this set of experiments, the internal electrode was used as the cathode.

Chapter 9: Observation of atmospheric pressure arc

High temporal and high spatial resolution charge coupled device (CCD) and complementary metal–oxide–semiconductor (CMOS) camera pictures of the atmospheric arc at different external magnetic field are presented. The arc root attachment and arc displacement results are presented. A correlation between arc rotational velocity and arc voltage is presented. In this set of experiments, the external electrode was used as the cathode.

Chapter 10: Carbon nanotubes as nanoparticle collector

Use of carbon nano tubes to collect and study nano particles formed as a by product in the continuous arc system is presented. Different applications of the carbon nano tubes having nano particles dispersed on them are presented. In this set of experiments, the external electrode was used as the cathode.

Chapter 11: Conclusions and original contributions

This chapter summarizes the major contributions enumerated in this study and states the original contributions of this thesis.

Chapter 12: Future work and recommendations.

Finally, the recommendations for future research endeavors are discussed.

1.4 References

1. Boulos M I, P Fauchais and E Pfender 1994 Thermal plasma fundamentals and applications Vol. 1 Plenum press New York.
2. Szente R N 1989 Erosion of plasma torch electrodes PhD Thesis Department of Chemical Engineering McGill University Montreal Canada.
3. Guile A E and Hitchcock A H 1981 Effect of transverse magnetic field on erosion rate of cathodes of rotating arcs *Proc. IEE* **128** 117-122.
4. Szente R N, R J Munz and Drouet M G 1987 Effect of low concentrations of a diatomic gas in argon on erosion of copper electrodes in a magnetically rotated arc *Plasma Chemistry and Plasma Processing* 7 349-364.
5. George A P and Hare A L 1983 Arc heater operating characteristics on oxygen and nitrogen, an interim report *Proc. ISPC-6* IUPAC Montreal A-5-2 144-147.
6. Porto D R, C W Kimblin and Tuma R J 1982 *Journal of applied physics* **53** 4740-4749.
7. Fu Y H and Smeets R P P 1989 The influence of contact surface microstructure on vacuum arc stability and voltage *IEEE Transactions on plasma science* **17** 5 727-729
8. Fu Y H 1989 The influence of cathode surface microstructure on DC vacuum arcs *J. Phys. D: Appl. Phys* **22** 94-102.
9. Fu Y H and Smeets R P P 1989 The influence of contact surface microstructure on vacuum arc stability and voltage *IEEE Transactions on plasma science* **17** 5 727-729.
10. Juttner B, Pursch H and Shilo V A 1984 The influence of surface roughness and surface temperature on arc spots movement in vacuum *J. Phys. D: Appl. Phys* **17** L31-L34.
11. Wang Y, Zhang C, Zhang H, Ding B and Lu K 2003 Effect of the microstructure of electrode materials on arc cathode spot dynamics *J. Phys. 8D: Appl. Phys.* **36** 2649-2654.

12. Zhang C, Yang Z, Wang Y and Ding B 2003 Cathode spot propagation on the surface of amorphous, nanocrystalline and crystalline $Cu_{60}Zr_{28}Ti_{12}$ cathodes *Physics Letters A* **318** 435–439.

Chapter 2 Contributions of authors

This chapter describes the author's contributions to the manuscripts that are incorporated in the thesis. All manuscripts report experimental work, manuscripts 4 through 8 are on quantifying the effect of microstructure on erosion behavior of copper cathodes. Chapters 9 and 10 are work related to atmospheric pressure plasma arcs. Chapters 5 and 6 are on pulsed vacuum arcs whereas the rest of the chapters are on continuous running atmospheric pressure magnetically rotated arcs. Except for chapter 8, I planned and carried out the all the experimental work and wrote the first draft of all papers. I contributed to modifications as the work evolved.

1 **Rao, L** and Munz, R. J. Arc velocity and erosion studies on annealed and hard drawn copper cylinders in magnetically rotated atmospheric pressure arcs. *Journal of Physics D: Applied Physics* (submitted) (Chapter 4)

2 **Rao, L** and Munz, R. J. Effect of surface roughness on erosion rates of pure copper coupons in pulsed vacuum arc system *Journal of Physics D: Applied Physics* (accepted) (Chapter 5)

3 **Rao, L.,** Munz, R. J. and Meunier, J-L. Vacuum arc velocity and erosion rate measurements on nanostructured plasma and HVOF spray coatings. *Journal of Physics D: Applied Physics*, **40** (14) , 4192-4201 (2007) (Chapter 6)

4 **Rao, L** and Munz, R. J. Effect of cathode microstructure on arc velocity and erosion rate of cold cathodes in magnetically rotated atmospheric pressure arcs. *Journal of Physics D: Applied Physics* (submitted) (Chapter 7)

I planned and carried out the experimental and analytical work shown in all of the above articles. I am also the first author of all of these articles.

5 D'Sa K., **Rao, L** and Munz, R. J. Effect of cathode microstructure on arc velocity and erosion rate of cold-sprayed copper cathodes in magnetically rotated atmospheric pressure arcs. *Journal of Thermal Spray Technology* (submitted) (Chapter 8)

I came up with the idea and experimental design to test cold sprayed coatings. I guided and assisted the summer student (Keith D'sa) with the experimental part of the work. I corrected/edited the manuscript written by Keith. I am the second author of the article.

6 **Rao, L.,** Munz, R. J. and Coulombe, S. Observation of atmospheric pressure arc on a cold cathode. *Applied Physics Letters* (accepted) (Chapter 9)

I planned and carried out the experimental and analytical work shown in this above article. I am also the first author of this article.

7 **Rao, L.,** Reddy N.K., Coulombe, S., Meunier, J-L., and Munz, R. J. Carbon nanotubes as nanoparticles collector. *Journal of Nanoparticle Research*, **9** (4) , 689-695 (2007) (Chapter 10)

I came up with idea of using carbon nano tubes as nanoparticles collector. I used carbon nanotubes grown by my colleague Reddy N.K, and carried out the experimental and analytical work shown in this article. I am also the first author of this article.

Chapter 3 Literature review

3.1 Electric arc discharges, vacuum arcs and atmospheric pressure arcs

A direct current (DC) electric arc is a self-sustaining discharge of electric current between two electrodes, the cathode and anode, maintained at different electrical potentials, in a conducting medium (electrode vapor or ionized gas). For vacuum arcs, electrode vapor necessarily serves as a conducting medium, whereas an ionized gas conducts electric current in atmospheric pressure arcs. Arc discharges have high current density and hence can support large currents at relatively low voltage drops.

In addition to their use in vacuum arc deposition of hard coatings and re-melting of metals, vacuum arcs are mainly used in circuit breakers [1-3]. High power electrical systems use vacuum circuit breakers as their chief safety device. Under operation, these vacuum switches must be able to withstand currents ranging from a few amps to several 100 kA of current between their contacts for over a few hundred microseconds. This is achieved by a vacuum arc discharge between these contacts [1]. The most common geometry of these contacts are rectangular coupons and circular discs.

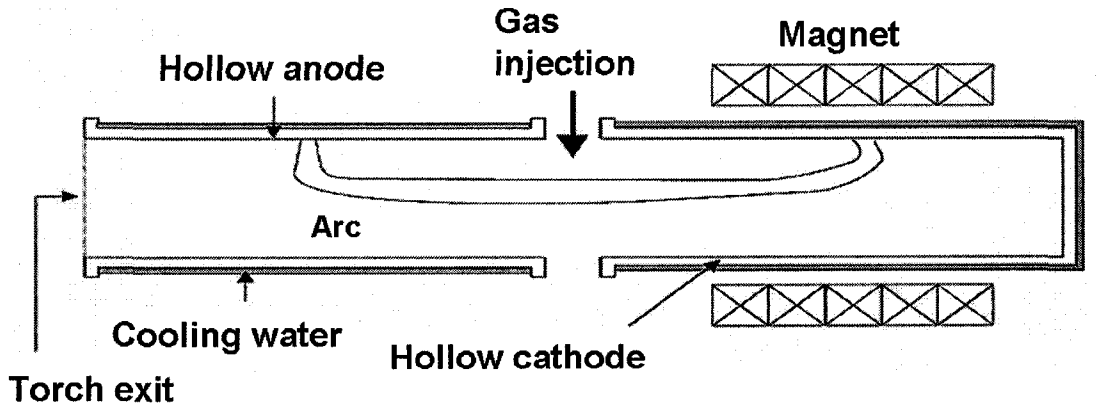

Figure 3.1 Schematic representation of an industrial DC plasma torch

Atmospheric pressure arcs are mainly used in plasma torches. Plasma torches are devices that generate a directed flow of electrically conducting gas (or plasma) from their nozzle. Figure 3.1 shows a schematic representation of an industrial DC plasma torch using tubular electrodes. The plasma torch consists of two electrodes, the cathode and the anode, maintained at different electrical potentials. When a sufficient potential difference is applied between these two electrodes, the otherwise non conducting medium between the electrodes starts to conduct electric current and forms an electric arc between the electrodes. This arc is rotated either magnetically or by a swirling gas flow or a combination of both. These torches are most commonly used as arc heaters to heat gases up to 5000 K [3]. The gas which is injected tangentially between the electrodes flows out of the torch nozzle as an electrically conducting gas.

Although a variety of materials are used as electrodes, copper, micro alloyed copper, tungsten and zirconium inserts are the most common materials. The geometry of plasma torches can vary greatly, but one common form is the tubular cathode, where the electrodes are heavily water cooled metallic circular cylinders. In this case, copper is the most common material used.

The work described in this thesis was carried out on a pulsed vacuum arc setup using rectangular coupons and also on a magnetically rotated atmospheric pressure arc setup using water cooled tubular cathodes. The electrode material used was copper. Copper cathodes having different microstructures were formed and tested for their erosion behavior.

3.2 The electrode-arc phenomena

3.2.1 The anode and cathode

The immediate vicinity of the two electrodes, the anode and the cathode is where the transition from gaseous conduction in the arc column, to metallic conduction in the electrode occurs [4].

The anode is essentially an electron receiver; therefore, solely electrons carry a current at an anode's surface. The anode is a passive electrode which does not play a critical role for maintenance of an arc; essentially it preserves current continuity [4]

The processes occurring at the cathode are more complex and play a vital role for self-sustenance of an arc. Unlike the anode, three current carrying mechanisms occur at the cathode surface

- Emission of electrons from the cathode surface
- Acceleration of positive ions towards the cathode surface
- Retro-diffusion of plasma-electrons towards the cathode surface

The details are discussed below.

3.2.2 Electron emission from cathode

Emission of electrons from the cathode is a critical factor governing the self-sustenance of an arc. Among many identified mechanisms supporting electron emission from a metal, thermionic, field and thermo-field mechanisms of electron emission are the dominant modes of electron emission.

Thermionic emission is a mechanism of electron emission, from the surface of the material, governed by the material's temperature. The electrons in a metal are trapped in the potential well; they can escape from the metal surface provided they absorb enough thermal energy to overcome this potential barrier [5]. This energy, also known as work function of the material, is the minimum quantity of energy an electron must absorb to escape from the metal surface. Thermionic emission from an arc cathode only becomes dominant mechanism at very high temperature (>3500 K) [4]. This mechanism of electron emission is normally seen on refractory cathodes such as thoriated tungsten and carbon cathodes.

Field emission is a mechanism of electron emission, whereby electrons are drawn out of a material's surface by electrostatic forces [5]. Very high electric fields of ~ 10^9 V/m, in the vicinity to the surface are required for field emission to become a significant mode of

electron emission. In addition to the above two modes of electron emission, due to high temperatures and intense electric fields prevailing in the near-cathode region, thermionic and field emission occur simultaneously. This mode is referred to as "thermo-field" emission. Low melting point cathodes such as those of copper operate primarily by field or thermo-field emission modes.

3.2.3 Cathode phenomena and cathode erosion

Processes occurring at the cathode region play a vital role for the self-maintenance of an arc. The cathode region is composed of the cathode surface, and an exceeding thin layer of gas and cathode vapor in front of it [6]. This thin layer of gas can be further divided into two zones; the pre-sheath or ionization zone and the cathode sheath zone as shown in figure 3.2. Significant gradients of voltage, particle number density and temperature exist in these zones and are shown in figure 3.3

Under steady operation of the arc, the cathode emits the electron by thermionic, field and/or thermo-field emission modes. The emitted electrons pass through the cathode sheath without collision; however, in the pre-sheath, they collide with the filling gas atoms and electrode vapors [7]. This causes ionization of the filling gas leading to the release of more electrons and the formation of positive ions.

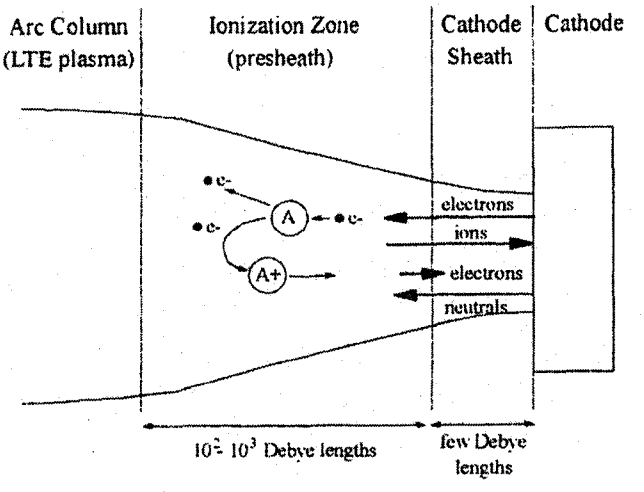

Figure 3.2 General representation of arc attachment at cathode [7]

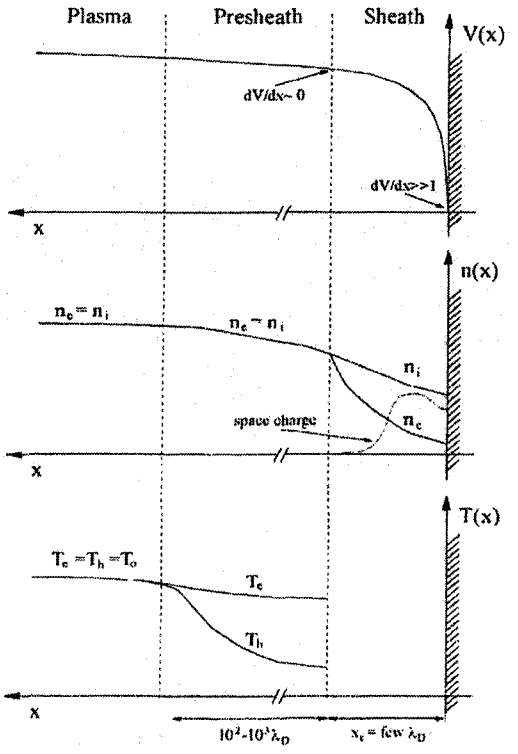

Figure 3.3 Gradients of voltage, particle number density and temperature in cathode region [7]

Radial diffusion of charged particles from the hot core of the arc column, to the relatively cold fringe of the column occurs and plays a role in current transfer. The positive ions produced in the pre-sheath are accelerated across the cathode sheath, under the influence of the voltage drop therein (see figure 3.3) and bombard the negatively charged cathode surface.

It is mainly this ion-cathode bombardment phenomenon that is responsible for the maintenance of high cathode surface temperatures, and thus ensures emission of electrons and production of cathode vapor.

Furthermore, since the mass of ions are many orders of magnitude greater than that of electrons, ions accelerate across the cathode sheath much slower than the electrons which

are accelerating in the opposite direction [4]. Consequently, there exists a net positive charge, called the space charge, in the cathode sheath.

This space charge creates a high local electric field and provides conditions for field emission [4]. In summary, we see that the bombarding ions create two important conditions: 1) maintenance of high cathode surface temperature and 2) formation of high surface electric field. The ion bombardment gives rise to two different effects, namely, thermionic emission and field emission.

Electron emission (thermionic, field or thermo-field), provides the electrons that ionize the gas and cathode vapor in the pre-sheath. The resulting ions and electrons serve to preserve current transfer between the electrodes and to compensate for radial diffusion losses.

In addition to creating a self-sustaining arc condition, ion bombardment leads to intense heating of the cathode. This intense heating results in melting and vaporization of the cathode material either as metal vapor or as liquid metal droplets. This loss of material from a cathode sustaining an electric arc [7] is cathode erosion. Typically, cathode erosion rates are expressed as the mass of the cathode lost per unit charge flowing through the cathode, namely micro grams per coulomb [μg/C].

Severe cathode erosion is a problem in the industrial application of plasma technology. Efforts to understand and minimize cathode erosion are numerous. Many factors affect cathode erosion and a brief discussion of these factors is presented here.

3.3 Factors affecting cathode erosion

Cathode erosion is affected by many different factors which act simultaneously. The following factors have all been reported to influence the cathode erosion rate: the arc residence time (or arc velocity) on the cathode, the cooling intensity of the cathode, plasma gas, its chemistry and flow rate, operating conditions such as arc current, arcing time and operating pressure, the cathode chemistry especially the O content for Cu

cathodes, surface roughness, microstructure and purity of the cathode and the size of the inter electrode gap [8-28].

3.3.1 Arc velocity and cooling intensity of the cathode

With inert plasma gases, among the above factors, arc velocity and heat removal from the cathode affect the erosion most [9]. Higher arc velocities imply lower arc residence time, less melting and vaporization of the cathode material and hence lower erosion rates. Better cooling of the cathode also prevents excessive melting and vaporization of the cathode material.

Arc velocity is in turn affected by external magnetic field used to rotate the arc [8], the plasma gas chemistry and flow rate [9-11], the O content of the cathode [12], the cathode surface roughness, purity and microstructure [13-28].

3.3.2 External magnetic field

The arc striking between the electrodes can be rotated either using a swirling gas or by an external magnetic field (B-field) or a combination of both. Depending on the operating pressure of the plasma system, the external B-field can cause either retrograde motion (in vacuum arcs) or arc movement in the Amperian direction (motion governed by the $\mathbf{I} \times \mathbf{B}$ force; in atmospheric pressure arcs). Increasing the B-field causes two effects: 1) the arc velocity increases [8] and 2) the arc attachment points (also called cathode spots) become aligned in the direction of the B-field lines and hence the arc becomes constricted [29]. Higher velocity reduces erosion while cathode spot alignment increases erosion due to increased local heating of the cathode. The competition between the two is known to decide the erosion rate [12].

3.3.3 Plasma gas chemistry, flow rate and its interaction with cathode

Plasma gas and its chemistry effects arc velocity significantly [12, 31] for Cu cathodes. Low concentrations (<1%) of polyatomic gases such as N_2, CO, Cl_2, CH_4, H_2S, NH_3 and O_2 in Ar and He are known to influence arc velocity significantly [12]. These poly atomic

gases change the surface chemistry and work function of the cathode material which leads to lower current densities and a broad distribution of cathode spots.

The presence of oxidizing atmosphere either in the plasma gas or low concentrations of O content in the cathode material, specifically for Cu, is also known to bring the same effect. These conditions promote easier electron emission allowing rapid movement of the cathode spots (giving higher velocities) and less arc stretching across the electrodes [12, 31, 32]. A higher concentration of O on the other hand develops a thick oxide layer leading to high joule heating and increased erosion.

Gas flow rates also affect arc velocities by the changing the gas density in the regions close to arc Higher gas flow rate causes higher cooling of the gas and hence increases the density of the gas through which the arc passes. This leads to a lower arc velocity [30].

3.3.5 Cathode surface roughness and microstructure

The surface properties such as surface micro-protrusion, roughness, impurity inclusions and microstructure of the cathode including, the grain size, second phase, changes in solute concentration and defect structure are known to significantly effect break-down voltage and dielectric strength of the electrode system [20-25].

Although the effect of surface roughness on the erosion of cathodes is mentioned [23, 33-36] only a handful of studies are available in the literature. Surface irregularities, like scratches on the cathode, are known to affect the movement of the vacuum arc [35]. The arc velocity is known to be a strong function of the direction of the surface roughness. Having scratches in the direction of the spot motion is known to give 2-3 times higher arc velocities relative to perpendicular surface scratches [17, 18, 20].

Some preliminary work on nanostructured CuCr cathodes, report on higher arc velocities and lower erosion rates [25-28]. But, a systematic study of the effect of cathodes surface roughness and microstructure on cathode erosion rate is not available and is the subject of this work.

3.4 References

1. Daalder J E 1978 Cathode erosion of metal vapour arcs in vacuum PhD thesis submitted to Eindhoven University of Technology Netherlands
2. Boxman L R, Sanders D M and Martin P J 1995 Handbook of vacuum arc science and technology: fundamentals and applications (New Jersey: Noyes publications)
3. Beilis I I 2001 State of the theory of vacuum arcs *IEEE transactions of plasma science* 29 5 657-670.
4. Guile A E 1971 Arc-electrode phenomena, *Proc. IEE, IEE Reviews,* **118,** 1131
5. Reece R J 1995 Industrial Plasma Engineering Volume 1: Principles (IOP publishing Ltd.)
6. Zhou X, Student, Heberlein J and Pfender E 1994 Theoretical study of factors influencing arc erosion of cathodes, *IEEE Trans. CPMT-Part A,* **17,** 1, 107-112
7. Coulombe S., 1997 A model of the electric arc attachment on non-refractory (cold) cathodes PhD Thesis submitted to McGill University of Montreal Canada
8. Guile A E and Hitchcock A H 1981 Effect of transverse magnetic field on erosion rate of cathodes of rotating arcs *Proc. IEE* **128** 117-122.
9. Szente R N, R J Munz and Drouet M G 1987 Effect of low concentrations of a diatomic gas in argon on erosion of copper electrodes in a magnetically rotated arc *Plasma Chemistry and Plasma Processing* 7 349-364.
10. George A P and Hare A L 1983 Arc heater operating characteristics on oxygen and nitrogen, an interim report *Proc. ISPC-6* IUPAC Montreal A-5-2 144-147.
11. Porto D R, C W Kimblin and Tuma R J 1982 *Journal of applied physics* **53** 4740-4749.
12. Szente R N 1989 Erosion of plasma torch electrodes PhD Thesis Department of Chemical Engineering McGill University Montreal Canada.

13. Teste P, T Leblanc, R Andlauer and J P Chabrerie 2001 Copper cathode erosion by an electric arc—the causes of the variations of the erosion rate with the electrode gap *Plasma Sources Sci. Technol.* **10** 2001 10-16.
14. Guile A E and Hitchcock A H 1975 Effect of water cooling on erosion of the copper cathode of a rotating arc *Proc. IEE* **122** 579-580
15. Guile A E and Hitchcock A H 1975 Erosion of copper cathodes by moving arcs at currents of 45-800 A *Proc. IEE* **122** 763-764
16. Guile A E and Hitchcock A H 1978 The erosion of copper cathodes from vacuum to atmospheric pressure arcs *Journal of applied physics* **49** 7 4275-4276
17. Fu Y H and Smeets R P P 1989 The influence of contact surface microstructure on vacuum arc stability and voltage *IEEE Transactions on plasma science* **17** 5 727-729
18. Fu Y H 1989 The influence of cathode surface microstructure on DC vacuum arcs *J. Phys. D: Appl. Phys* **22** 94-102.
19. Lakshminarayana Rao, Munz R J and Meunier J-L 2007 Vacuum arc velocity and erosion rate measurements on nanostructured plasma and HVOF spray coatings *J. Phys. D: Appl. Phy* **40** 4192-4201.
20. Fu Y H and Smeets R P P 1989 The influence of contact surface microstructure on vacuum arc stability and voltage *IEEE Transactions on plasma science* **17** 5 727-729.
21. Schmoll R 1998 Analysis of the interaction of cathode micro protrusions with low-temperature plasmas *J. Phys. D: Appl. Phys.* **31** 1841-1851.
22. Farrall G A 1985 Electrical breakdown in vacuum *IEEE Transaction on electrical insulation* **20** 815-841.
23. Juttner B, Pursch H and Shilo V A 1984 The influence of surface roughness and surface temperature on arc spots movement in vacuum *J. Phys. D: Appl. Phys* **17** L31-L34.
24. Daalder J E and Vos C W M 1972 Distribution functions of the spot diameter for single and multi cathode discharges in vacuum Eindhoven University of Technology Eindhoven Netherlands Rep 72-E-32.

25. Ding B, Yang Z and Wang X 1996 Influence of microstructure on dielectric strength of CuCr contact materials in vacuum *IEEE Transactions on Components, Packaging and Manufacturing Technology Part-A* **19** 1 76-81.
26. Wang Y P and Ding B J 1999 The preparation and their properties of microcrystalline and nanocrystalline CuCr contact materials *IEEE Transactions. CPT* **22** 467–72.
27. Wang Y, Zhang C, Zhang H, Ding B and Lu K 2003 Effect of the microstructure of electrode materials on arc cathode spot dynamics *J. Phys. D: Appl. Phys.* **36** 2649-2654.
28. Zhang C, Yang Z, Wang Y and Ding B 2003 Cathode spot propagation on the surface of amorphous, nanocrystalline and crystalline $Cu_{60}Zr_{28}Ti_{12}$ cathodes *Physics Letters A* **318** 435–439.
29. Drouet M G 1981 Japan J. Appl. Physis. Vol 20. 10270-1036
30. Szente R N 1986 Cathode erosion in magnetically rotated arcs Master Thesis Department of Chemical Engineering McGill University Montreal Canada.
31. Szente R N, R J Munz and Drouet M G 1989 Cathode erosion in inert gases: the importance of electrode erosion *Plasma Chemistry and Plasma Processing* **9** 1 121-132.
32. Juttner B 1981 Formation time and heating mechanism of arc cathode craters in vacuum *J. Phys. D: Appl. Phys.* **14** 1265-1275.
33. Reece M P 1956 Arcs in vacuum *Nature* **177** 1089-1090.
34. Germer L H and W S Boyle 1955 Anode and cathode arcs *Nature* **176** 1019.
35. Cobine J D and C J Gallagher 1948 Current density of the arc cathode spot *Phys. Rev.* **74** 10 1524-1530.
36. Daalder J E 1974 Diameter and current density of single and multiple cathode discharges in vacuum *IEEE Trans. Power Appar. Syst.* **PAS-93** 1747-1758.

Chapter 4 Arc velocity and erosion studies on annealed and hard drawn copper cylinders in magnetically rotated atmospheric pressure arcs

This chapter presents the effect of microstructure on erosion behavior of hard drawn and annealed pure Cu cathodes. The experimental setup and experimental procedure for continuous running magnetically rotated atmospheric pressure arc experiments are described. Pre and post erosion microstructural analysis of the cathodes are presented.

Although the differences in grain size of these two kinds of cathodes were small, the results confirmed the effect of grain size on erosion behavior of the cathodes.

Abstract

From anecdotal and some experimental evidence on cathode electrode erosion, it has been hypothesized that the microstructure of the cathodes influences arc velocity and arc erosion rate. In this paper we present atmospheric pressure erosion measurements on hard drawn and annealed copper cathodes having different grain sizes. Hard drawn cathodes had elongated grains (average grain size of 6 and 20 μm in the direction perpendicular and parallel to drawing directions respectively) whereas Cu cathodes annealed at 500 ^{0}C, had equi-axed grains with an average grain size of 21 μm. All erosion measurements were performed at a constant power setting of 6 kW (40 V and 150 A), external magnetic field of 0.05 T and argon gas flow rate of 23 slpm. The erosion rates measured indicate that hard drawn electrodes which have smaller grains give 16 % lower erosion rates relative to annealed electrodes. Microstructural analysis of the arc trace show grain relaxation and grain growth on hard drawn electrodes only.

4.1 Introduction

Industrial applications of plasma technology range from circuit breakers to waste water treatment and from material processing to nano technology [1]. Current research is focused on development of plasma systems with long electrode lifetimes and reproducible working conditions [2]. Control of electrode erosion in plasma torches remains a major challenge for researchers. Particularly for plasma torches using Cu electrodes in tubular geometry, cathode erosion is far greater than anode erosion [3].

Although many factors affect cathode erosion, arc residence time (or arc velocity) and heat removal from the cathode have a very major effect [3]. Higher arc velocities imply lower arc residence time, less melting and vaporization of the cathode material and hence lower erosion rates. Better cooling of the cathode also prevents excessive melting and vaporization of the cathode material [3]. Arc velocity is in turn affected by the external magnetic field used to rotate the arc [4], the presence or absence of an oxidizing plasma gas [3], the O content in the cathode and also the microstructure of the cathode [3,5-7]. Earlier research has shown that, cathodes having smaller grain size promote higher arc velocities [6]. Although a few published works studies the effect of the cathode's microstructure on the rate of erosion [7, 8], this has received little attention.

In this paper we report on the arc velocity and erosion behavior of hard drawn and annealed Cu cathodes having two different grain sizes. It is hypothesized that, hard drawn cathodes which have elongated small grains in the direction of the drawing (and of the arc motion) give lower erosion rates when compared to annealed electrodes which have equi-axed larger grains. In addition, pre and post erosion microstructural analyses were performed for both hard drawn and annealed cathodes.

4.2 Materials and methods

4.2.1 Heat treatment

Hard drawn copper tubes (99.9% pure Cu) obtained from Wolverine Tubes Inc. were used as cathodes either in their as purchased state or after annealing them in an inert atmosphere. Annealing was carried out in a nitrogen atmosphere at 500 ^{0}C for 8 hrs. Chemical composition of both the as-purchased Cu tubes and annealed Cu tubes were determined by inductively coupled plasma mass spectroscopy (ICP).

For microscopic analysis, both hard drawn and annealed Cu tubes were cut using a Struers 'Secotom-10' universal precision cut off machine and vacuum mounted in cold setting resin. The mounted specimens were wet ground using SiC papers #800, 1200 and 4000 under running tap water. The ground samples were the polished using 3 μm and 0.04 μm silica suspensions. The polished samples were etched with a $FeCl_3$ etchant (2.5 g of $FeCl_3$ + 10 ml of HCl + 50 ml of ethanol) for 5 seconds. The etched specimens were examined under optical microscope to determine their microstructure.

4.2.2 Experimental setup

The erosion test chamber used in this work is shown in figure 4.1. It was a water-cooled gas tight enclosure which housed two electrically isolated electrodes from its chamber. The setup was able to operate at either polarity. For this work, the central electrode was used as the anode and annular test electrode was the cathode. The central anode had a raised portion to localize the arc as shown in figure 4.1b. The minimum distance between the electrodes was 4 mm. Figure 4.1c shows the end on view of the electrode assembly.

A water-cooled solenoid around the test chamber was used to apply an axial magnetic field B of 0.05 T, to rotate the arc. The solenoid consisted of 150 m of 6.35 mm outer diameter copper tubing in seven layers of 29 turns each. The layers were separated by 1-mm-thick Mylar sheet and individual turns were insulated with electrical tape. The axis of the solenoid coincided with the central axis of the reactor. All parts of the test chamber were made of non magnetic material. Experimental measurements showed that the axial

magnetic field strengths created by the solenoid varied less than 3% radially and 5% axially within the test cathode.

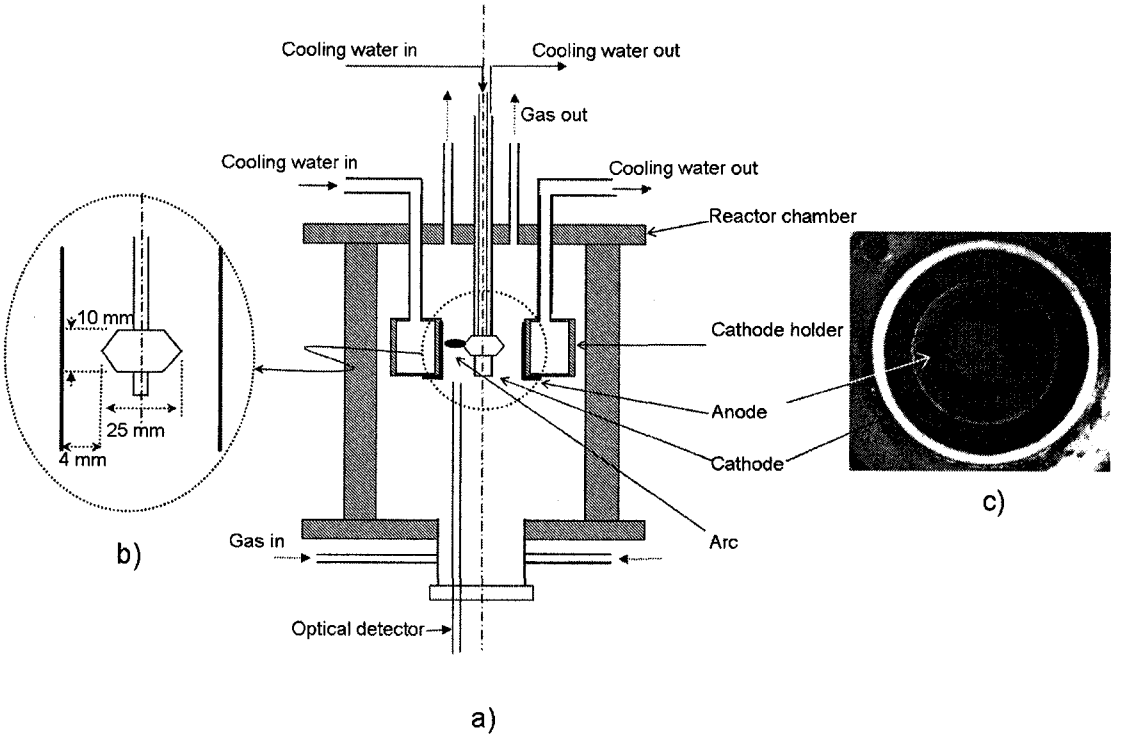

Figure 4.1 a) Schematic of the experimental setup; b) Raised portion of the electrode assembly c) Picture of the electrodes assembly; end on view

An optical detector as shown in figure 4.1a was used to capture the arc rotation frequency. The optical detector consisted of a photodiode and a collimating lens assembly which had a narrow field of view of 3 mm. The optical detector assembly was aligned to view the arc between the electrodes and gave a positive voltage output when the arc passed in its narrow field of view. This optical voltage output along with the arc current and arc voltage waveforms were recorded simultaneously onto a computer using LabVIEW at 10 kHz sampling rate. The arc rotational frequency was calculated from the recorded optical voltage data using windowed fast Fourier transform analysis. The arc current data were used to calculate the total electric charge transfer between the electrodes.

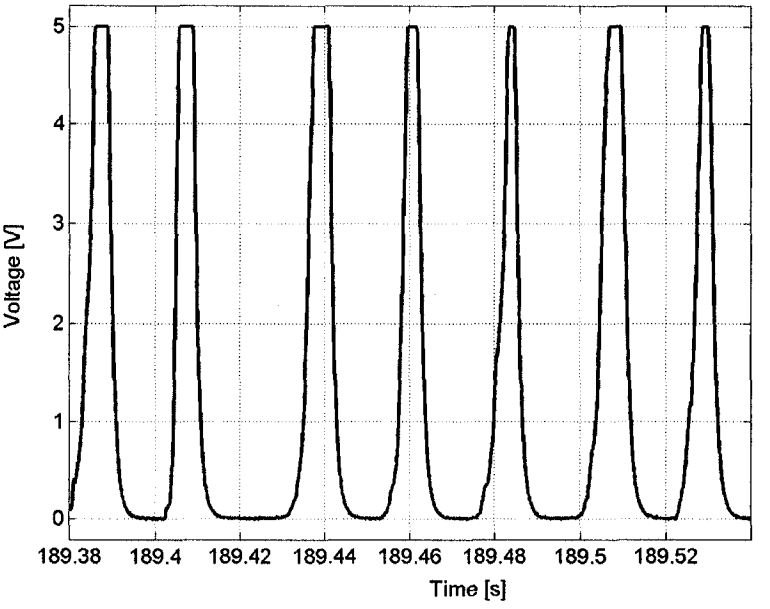

Figure 4.2 Voltage output from the optical detector

Two separate rectifiers were used to power the arc and the magnetic coil. The arc was powered by a welding power supply (maximum power and current of 78 kW and 500 A, respectively) while the solenoid was powered by an 18 kW rectifier (60 V and 300 A). The arc was ignited using a Miller HF 250-1 high-frequency trigger pulse. An average power of 6 kW (40 V and 150 A) was maintained throughout the experiments. Experiments were conducted using ultrahigh purity (UHP; 99.99% pure) argon as plasma forming gas, which circulated from the lower end of the reactor to the top end at a flow rate of 23 SLPM under atmospheric pressure. Gas and water flow rates were monitored and controlled with calibrated rotameters.

4.2.3 Experimental procedure

At the start of each experiment, the test cathode was cleaned in 5% dilute nitric acid to remove native copper oxide layer. The cleaned electrode was dried using a hair drier and wiped clean with soft cloth. The cleaned electrode was allowed to sit in air for 10 minutes to form a uniform native oxide layer on the cathode. The cathode was then weighed to $\pm 1\times10^{-4}$ g accuracy using a digital balance and was installed into the test chamber. The

test chamber was flushed with ~100 chamber volumes of Ultra High Purity (UHP) argon flowing at 23 slpm. The arc was ignited and the test cathode was eroded until a steady arc rotation velocity was reached. Figure 4.2 gives an example of the optical signal captured using the optical detector.

After the experiment, the cathode was removed from the reactor, cleaned with dilute nitric acid, and dried before recording its final weight. The erosion rate values in grams per coulomb were calculated by dividing the weight difference of the cathode before and after the arcing, by the total electric charge $Q = \int I\, dt$ passing through the cathode. The arc rotational frequency was calculated from the recorded optical voltage data using windowed fast Fourier transform analysis. Each erosion experiment lasted between 180 to 240 s. A total of six cathodes (viz., three hard drawn and three annealed) were eroded and the average and standard deviations were calculated.

4.3 Results and discussion

4.3.1 Characterization of cathodes pre erosion

Figure 4.3 shows the cross sectional optical microscope pictures of the hard drawn and annealed cathodes before erosion. Figures 4.3a and 4.3b are images of the hard drawn cathode perpendicular and parallel to the drawing direction respectively. Similar pictures taken for annealed cathodes are shown in figures 4.3c and 4.3d.

We can see from figure 4.3a and 4.3b, that hard drawn cathodes have elongated grains in the direction of drawing (along its length). The elongated grains had an average length of 20 ± 2 μm in the direction of drawing whereas their average width was only 6 ± 1 μm. Figures 4.3c and 4.3d are cross sectional images of an annealed cathode in the perpendicular and parallel drawing direction respectively. Here we see that the grains in both directions appear equi-axed indicating grain growth and recrystallisation due to annealing. The equi-axed grains had an average size of 21 ± 2 μm.

Hence, the arc which is set up to run perpendicular to the drawing direction (shown by arrows in figure 4.3) would see small grains on hard drawn cathodes compared to annealed cathodes.

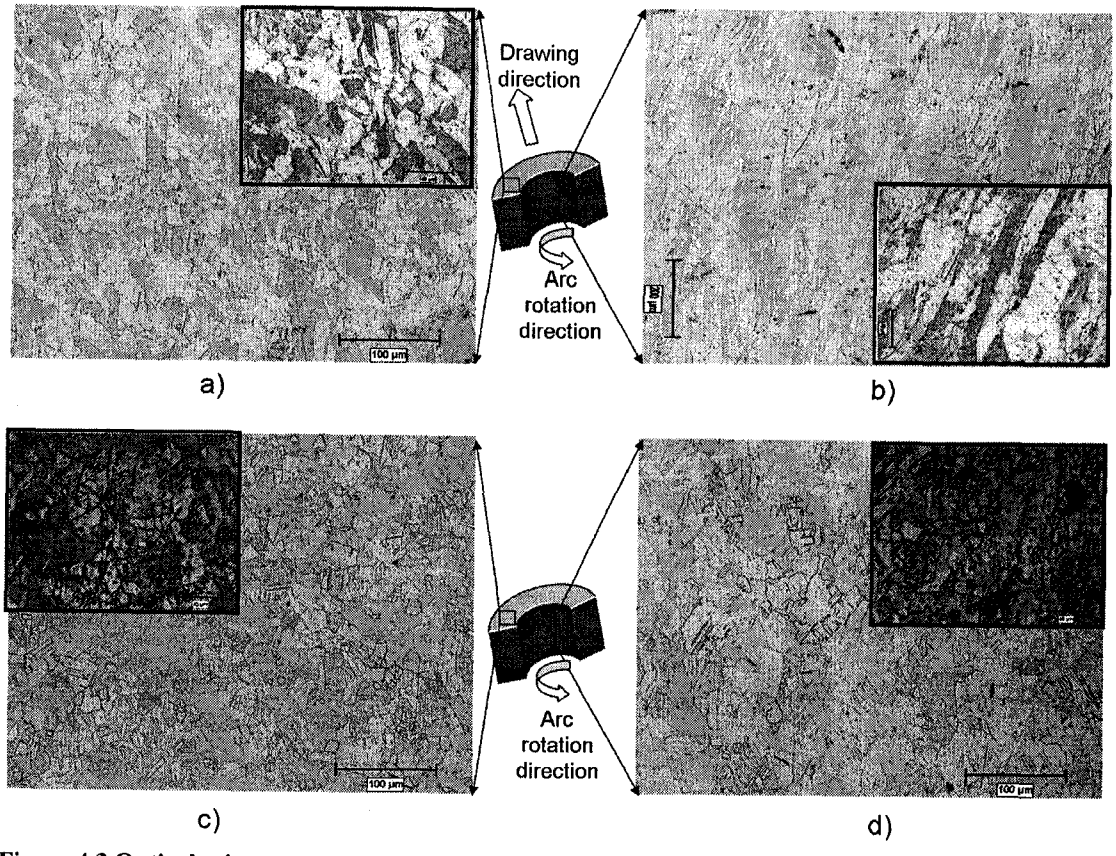

Figure 4.3 Optical microscope pictures of cathodes before erosion; cross sectional view; a) hard drawn electrode perpendicular to drawing direction; b) hard drawn electrode parallel to drawing direction; c) annealed electrode perpendicular to drawing direction; d) annealed electrode parallel to drawing direction; for all inset picture dimension bar length = 40 μm.

4.3.2 Arc erosion and velocity measurements

Three hard drawn and three annealed electrodes were eroded under identical experimental conditions to find erosion rates. The results obtained are given in table 4.1 along with the mean and standard deviations. We can see from table 4.1 that, the erosion rates on hard drawn electrodes which had lower grain sizes had an erosion rate of 30.70 ± 1.26 μg/C whereas annealed electrodes which had larger grains showed an erosion rate of 36.64 ± 2.71 μg/C. Statistical analysis on the erosion values showed that with a 95%

confidence level, the erosion values for hard drawn cathodes was lower than that of annealed cathodes.

Figure 4.4 shows typical arc rotation velocity results for both electrode types. We can see from figure 4 that both the electrodes have two velocity regimes. A high velocity regime (50-70 m/s), for the first 50 to 80 s of the experiment, followed by a low velocity regime (2 -3 m/s), for the rest of the experiment. The high velocity regime was attributed to the movement of the arc on the native oxide layer present on the cathodes and the slow regime was due to the arc moving on pure Cu, free from the oxide layer. This layer was removed during the initial erosion between 50 to 80 s of the experiment [3].

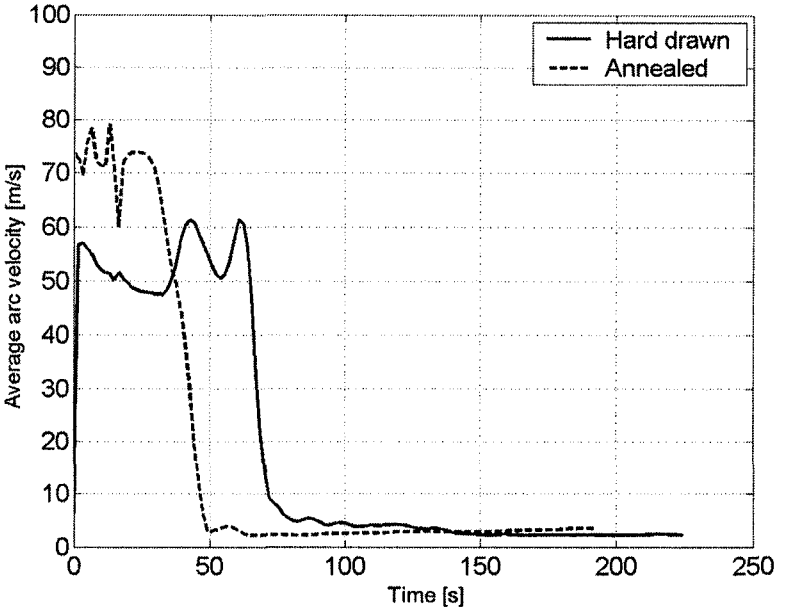

Figure 4.4 Arc velocities on hard drawn and annealed cathodes

Table 4.1 Erosion rate results

Electrode type	Erosion rate [μg/C]				
	1	2	3	Average	Std. dev
Hard drawn	32.09	29.60	30.31	30.70	1.26
Annealed	39.76	35.26	34.92	36.64	2.71

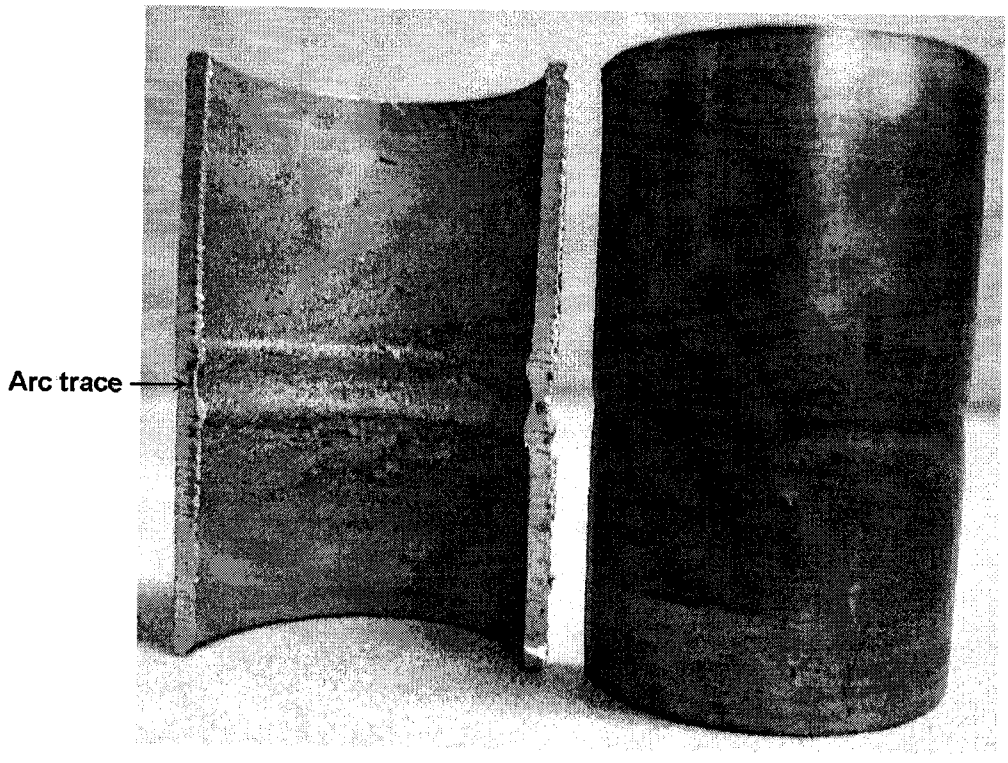

Figure 4.5 Arc trace on the cathode

4.3.3 Characterization of cathodes after erosion

Figure 4.5 shows a picture of typical arc trace on the cathode after an erosion experiment. Microstructural specimens were taken from the arc trace and were analyzed for possible microstructural changes. The results obtained are shown in figure 4.6.

Figures 4.6a and 4.6b show an optical microscope image of the arc trace left on hard drawn electrode perpendicular and parallel to the drawing direction respectively. Small columnar grains can be clearly seen from figure 4.6a indicating melting and rapid solidification. From figure 4.6b, we see that the initial elongated grains (shown in figure 4.3b) have relaxed to form equi-axed grains. Grain relaxation is attributed to the heating of the cathode under the arc.

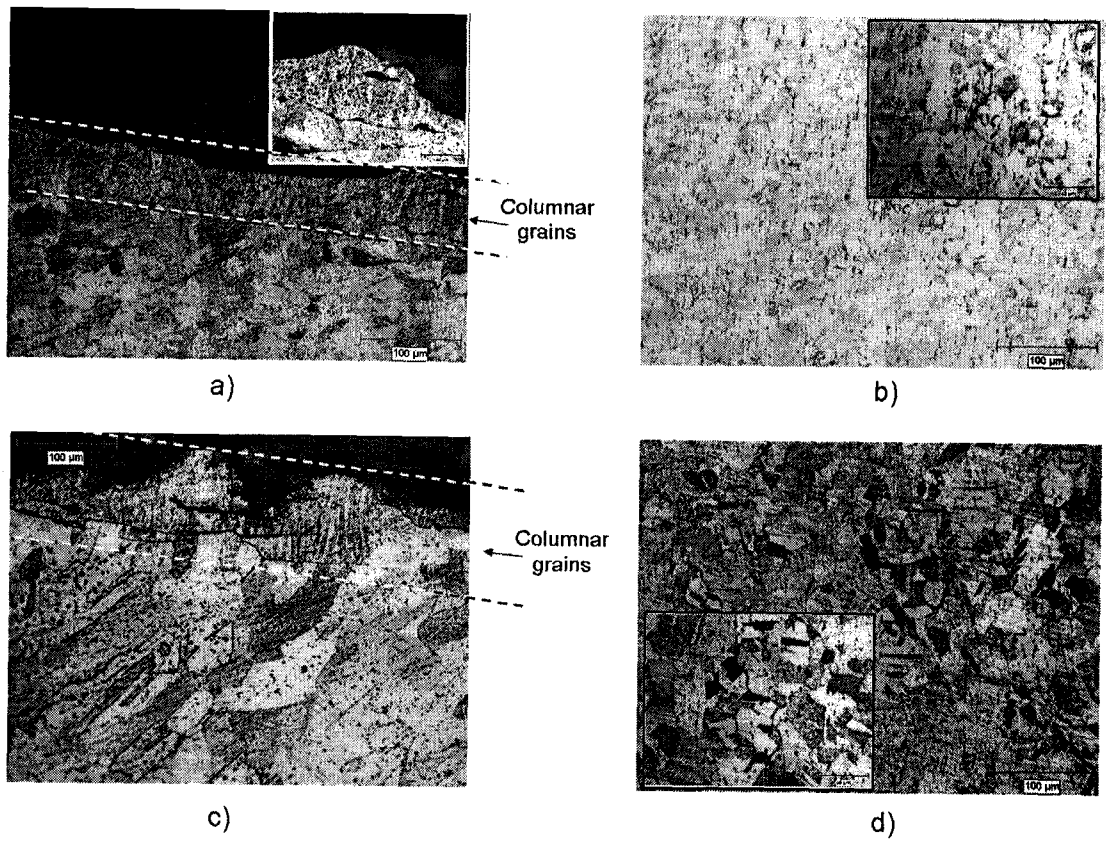

Figure 4.6 Optical microscope pictures of the cathode on the arc trace; cross sectional view; a) hard drawn electrode perpendicular to drawing direction; b) hard drawn electrode parallel to drawing direction; c) annealed electrode perpendicular to drawing direction; d) annealed electrode parallel to drawing direction; for all inset picture dimension bar length = 40 μm

Figures 4.6c and 4.6d show an optical microscope image of the arc trace left on an annealed electrode perpendicular and parallel to the drawing direction respectively. Again, small columnar grains can be seen in figure 4.6c, which is an optical microscope image of the arc trace taken perpendicular to the drawing direction. In figure 4.6d, unlike hard drawn cathodes, no grain growth or grain relaxation was observed. It was concluded that the grains in the annealed cathodes had reached their maximum size during annealing itself and additional heating of the cathode under the arc did not cause any changes in the grain size of the fully annealed cathode.

4.4 Conclusions

We conclude that, the grain size of the cathodes affects arc erosion rates. Hard drawn electrodes having smaller (6 ± 1 μm) grain sizes perpendicular to the motion of the arc showed 16% lower erosion rates compared to electrodes with larger (21 ± 2 μm) grain sizes.

Grain relaxation and grain growth in the arc trace region were clearly observed on hard drawn cathodes whereas no such effect was observed on fully annealed cathodes. Small columnar grains were noticed on the arc traces for both hard drawn and annealed cathodes.

4.5 Acknowledgements

We wish to acknowledge the financial support provided by the Natural Sciences and Engineering Research Council of Canada (NSERC), and Wolverine Tubes Inc. for supply of hard drawn Cu tubes.

4.6 References

1. C Tendero Tixier C Tristant P Desmaison J and P Leprince 2006 Spectrochimica Acta Part B **61**.
2. J M Park Kim K S Hwang T H and S H Hong 2004 IEEE Transactions On Plasma Science **32** 2.
3. Szente R N, R J Munz and Drouet M G 1987 Effect of low concentrations of a diatomic gas in argon on erosion of copper electrodes in a magnetically rotated arc *Plasma Chemistry and Plasma Processing* **7** 349-364.
4. Guile A E and Hitchcock A H 1981 Effect of transverse magnetic field on erosion rate of cathodes of rotating arcs *Proc. IEE* **128** 117-122.
5. Szente R N 1989 Erosion of plasma torch electrodes PhD Thesis Department of Chemical Engineering McGill University Montreal Canada.
6. Lakshminarayana Rao, Munz R J and Meunier J-L 2007 Vacuum arc velocity and erosion rate measurements on nanostructured plasma and HVOF spray coatings *J. Phys. D: Appl. Phy* **40** 4192-4201.
7. Fu Y H 1989 The influence of cathode surface microstructure on DC vacuum arcs *J. Phys. D: Appl. Phys* **22** 94-102.
8. Wang Y, Zhang C, Zhang H, Ding B and Lu K 2003 Effect of the microstructure of electrode materials on arc cathode spot dynamics *J. Phys. D: Appl. Phys.* **36** 2649-2654.

Chapter 5 Effect of surface roughness on erosion rates of pure copper coupons in pulsed vacuum arc system

This chapter describes the effect of surface roughness and surface pattern on erosion behavior of pure Cu cathodes in a pulsed vacuum arc setup. Preparation of pure Cu cathodes having different surface roughness and pattern is described. The experimental setup used to test for erosion is explained in brief here. The erosion rates are given and the arc traces are analyzed for crater size and arc movement.

Though surface roughness is different from grain size, it is related to the microstructure of the cathode. The results indicate that, reducing the initial surface roughness reduces erosion rates of pure Cu cathodes in vacuum arcs. Effect of roughness on erosion behavior in atmospheric pressure arcs is presented in chapter 7.

Abstract

Vacuum arc erosion measurements were performed on copper cathodes having different surface roughness and surface patterns in 10^{-5} Torr vacuum (1.3324 m Pa), in an external magnetic field of 0.04 T. Different surface patterns and surface roughness were created by grit blasting with alumina grits (G-cathodes) and grinding with silicon carbide emery paper (E-cathodes). The erosion rates of these cathodes were obtained by measuring the weight loss of the electrode after igniting as many as 135 arc pulses, each of which was 500 μs long at an arc current of 125 A. The erosion rates measured indicate that erosion rates decrease with decreasing roughness levels. Results obtained indicate that both surface roughness and surface patterns affect the erosion rate. Having patterns perpendicular to the direction of arc motion gives lower erosion rates than having patterns parallel to arc movement. Isotropic surfaces give lower erosion rates than patterned surfaces at the same roughness.

Keywords: Surface roughness, surface pattern, cold cathode erosion, vacuum arcs

5.1 Introduction

High power electrical systems use vacuum circuit breakers as their chief safety device. Under operation, these vacuum switches must be able to withstand currents ranging from a few amps to several 100 kA of current between their contacts for over a few 100 microseconds. This is achieved by a vacuum arc between these contacts. Erosion of contacts in these safety switches determines their life [1]. Erosion of these contacts has been a subject of study for the past 50 years and it is well known that the negative contact (cathode) erodes faster than the positive contact [2-4]. Researchers have shown that many factors such as geometry of the cathode, operating vacuum, inter electrode gap, plasma forming gas, surface chemistry and electrode microstructure meaning the grain size affect the nature and extent of cathode erosion [5-12]. It was observed in 1942 by Cobine and Callagher [13] that surface irregularities, like scratches, affect the movement of the vacuum arc on the cathode. Although many researchers mention the effect of surface roughness [14-16] on the erosion of cathodes only a hand full of systematic studies are available in the literature. Daalder [16] in his meticulous study of the effect of surface roughness on erosion of copper cathodes, only reports on the effect of roughness on the size and movement of the cathode spots formed and not the erosion rate itself. Daalder and Vos [17] have shown that the arc voltages have different values on cathodes of different roughness. Y.H Fu [18-20], studying the effect of surface roughness in the presence of an external magnetic field (B field), has reported that the cathode spot retrograde arc velocity is a strong function of the direction of the surface roughness. She has reported that when the grinding is in the direction of the spot motion imposed by the external B field, the arc velocities are several times higher relative to a perpendicular ground surface. She has observed that the arc voltage on rough surfaces was higher than the smooth surfaces in the presence of an external B field. But again she does not report on any erosion rate measurement which is a chief parameter in calculating the life time of a contact in vacuum circuit breakers.

In this paper, we report on the effect of surface roughness on the erosion rates of pure copper cathodes measured at 10^{-5} Torr vacuum (1.3324 m Pa). Different surface roughness levels were created by grinding with three different sizes of silicon carbide

emery papers and also by grit blasting the surface with two different sizes of alumina grits. Regular surface patterns were created by the emery method whereas grit blasting yielded isotropic rough surfaces. The different cathodes formed were characterized for their roughness levels using a surface profilometer and vacuum erosion rates on these cathodes were measured. Arc craters formed on these cathodes were analyzed using a field effect scanning electron microscope (Hitachi-4700). The results obtained were compared to the literature values of smooth pure Cu. The details are presented below.

5.2 Materials and experimental methods

Electronic grade oxygen free high electrical conductivity pure copper (99.99 wt %) was used in this study. As purchased machine finished copper bars were cut into rectangular strips of 60 mm × 12 mm × 3 mm and used as cathodes for erosion experiments. Different surface patterns and surface roughnesses were created on these copper strips using two methods viz., grit blasting (further referred as G) and grinding with emery paper (further referred as E). Two different sizes of alumina grit viz., 190 μm and 708 μm were blasted with nitrogen at 45 psig, to create an isotropic surface roughness and pattern. Three different sizes of silicon carbide emery paper viz., 35 μm grit size, 95 μm and 190 μm grit size, were used to obtain a unidirectional surface pattern. Unidirectional surface patterns were created both parallel and perpendicular to the length of the copper strip. The surface roughness created was measured using a surface profilometer (DekTak) and the Ra values were calculated. Just before using them for erosion studies these copper strips were carefully cleaned by ultrasound with acetone as the cleaning medium dried with a soft cloth and immediately installed into a vacuum chamber. The schematic diagram of the experimental setup used for this study is shown in figure 5.1 and the details of the experimental setup are given elsewhere [21]. In essence, it consisted of a vacuum chamber, a power supply unit and a pulsed laser system. Vacuum chamber held the rectangular strip cathode mounted parallel to a rectangular Cu anode (50mm × 10mm × 3mm). Before the start of each experiment, the electrodes were placed in the chamber maintaining an inter-electrode gap of 5mm and the chamber was pumped down to 10^{-2} Torr using a mechanical pump. At this vacuum, the reactor was filled with ultra high

purity argon and then pumped to 10^{-5} Torr by a mechanical and an oil diffusion pump connected in series. A permanent U shaped magnet (B field = 0.04 T) was positioned behind the cathode to move the arc in the retrograde direction, parallel to the length of the copper strip. Capacitors in the arc power supply unit were charged to an open circuit voltage of 200 V. A pulsed arc was initiated on the cathode by a 1000 ns pulse of 10.6 μm infrared laser radiation from a 1.2 kW Diamond^{TM} K-500 CO_2 laser system, supplied by Coherent technologies. A thyristor based electrical switching circuit was used to control a 500 μs arc duration over which, a constant current of 125 A was maintained. This square current pulse was measured using an externally triggered HP-54503A digital oscilloscope. To determine the erosion rate, as many as 135 arc pulses, each 500 μs long with a current of 125 A, were run on the cathode. These pulses were run at a rate of 3-4 pulses per minute. The erosion rate values in grams per coulomb were measured by weighing the cathode before and after the arcing, using a digital balance (accuracy ± 1×10^{-4} gm) and then dividing the weight difference by the total electric charge $Q = \int I\,dt$, passing through the cathode. For each surface pattern and roughness, erosion rates were measured on three individual cathodes. An average of these three measured values was calculated and reported as average erosion rate.

5.3 Results and discussion

5.3.1 Surface roughness characterization

The cathodes prepared were characterized for their roughness, Ra values, using a surface profilometer (DekTak). Table 5.1 gives a summary of the surface patterns and the Ra values for each kind of cathode used. Each kind of cathode was scanned for a length of 0.5 cm in the soft touch mode and the Ra values were computed with inbuilt software. Two individual measurements were made on each kind of cathode and the standard deviations computed are reported as error in table 5.1. On surfaces prepared by emery paper (E-cathodes), which had unidirectional patterns, the surface was only scanned perpendicular to the direction of the pattern created whereas on surfaces prepared by grit

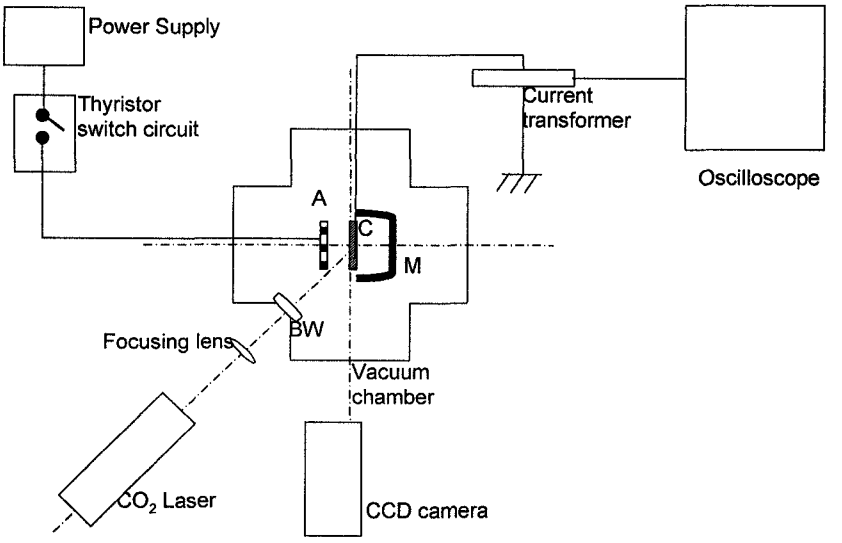

Figure 5.1 Schematic diagram of the experimental setup A = anode; BW = beryllium window; C = cathode and M = permanent magnet.

blasting (G-cathodes), surface was scanned in both parallel and perpendicular directions. We see that the Ra values increase with the grit size used. For G-cathodes, the Ra values were similar in both parallel and perpendicular directions showing that the roughness created was isotropic. On E-cathodes, at a particular emery grit size, both parallel patterned and perpendicular patterned cathodes had similar Ra values. Thus the only difference between the two kinds of E-cathodes prepared from the same emery paper is the surface pattern.

Figure 5.2 shows a plot of Ra vs. grit size used. We see that the Ra value of E-190 cathodes is slightly lower than that of G-190 cathodes although the grit size used in both the cases were same.

Table 5.1 Summary of the cathodes studied.

Name	Preparation method	Grit size [μm]	Roughness Ra [μm]	Pattern type	
E-36-llel	Grinding with emery	36	0.86 ± 0.1		Parallel to sample length
E-36-ular	Grinding with emery	36	0.66 ± 0.1		Perpendicular to sample length
E-95-llel	Grinding with emery	95	1.70 ± 0.1		Parallel to sample length
E-95-ular	Grinding with emery	95	1.48 ± 0.1		Perpendicular to sample length
E-190-llel	Grinding with emery	190	2.67 ± 0.3		Parallel to sample length
E-190-ular	Grinding with emery	190	2.64 ± 0.1		Perpendicular to sample length
G-190	Grit blasting	190	3.31 ± 0.1 (Direction parallel) 3.31 ± 0.1 (Direction perpendicular)		Isotropic
G-708	Grit blasting	708	7.32 ± 0.1 (Direction parallel) 7.42 ± 0.1 (Direction perpendicular)		Isotropic

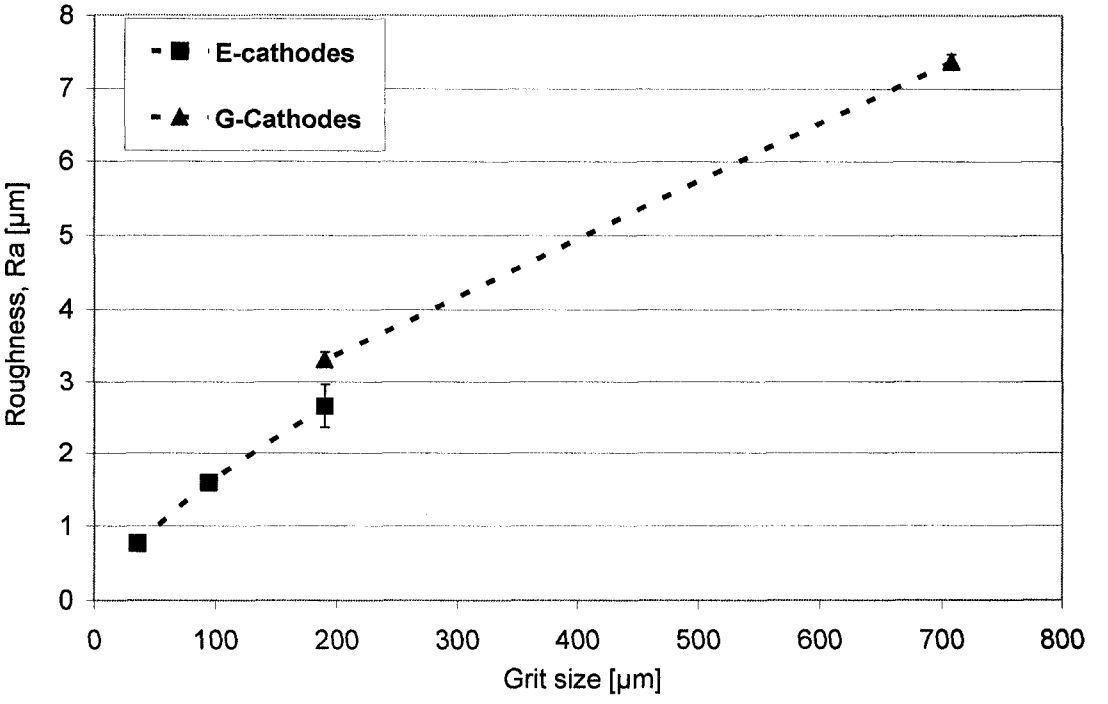

Figure 5.2 Grit size vs. roughness Ra

Figure 5.3 shows the scanning electron microscope (SEM) pictures for each kind of cathode used. For E-cathodes, only cathodes having parallel patterns are shown here since the SEM pictures of the surfaces with perpendicular patterns had similar features. Figure 5.3a, b and c are SEM pictures of E-cathodes prepared from grit size 36 µm, 95 µm and 190 µm respectively. We can see the unidirectional ridges on the surface which are mostly parallel to one another. Individual ridges have many sharp projections. Comparing figure 5.3a through 5.3c we can clearly see that, as the grit size is increased, the width of the ridge formed is also increased and so is the separation between the individual ridges. Figure 5.3d and 5.3e are the SEM images of the G-cathode formed after grit blasting with 190 µm and 708 µm alumina grits respectively. On these cathodes no directional features are noticeable, which corroborates the isotropic Ra values measured. The cathode formed from 708 µm grit has larger irregular features (shown by the dotted circle) when compared to the features observed on the cathodes formed from 190 µm alumina grits.

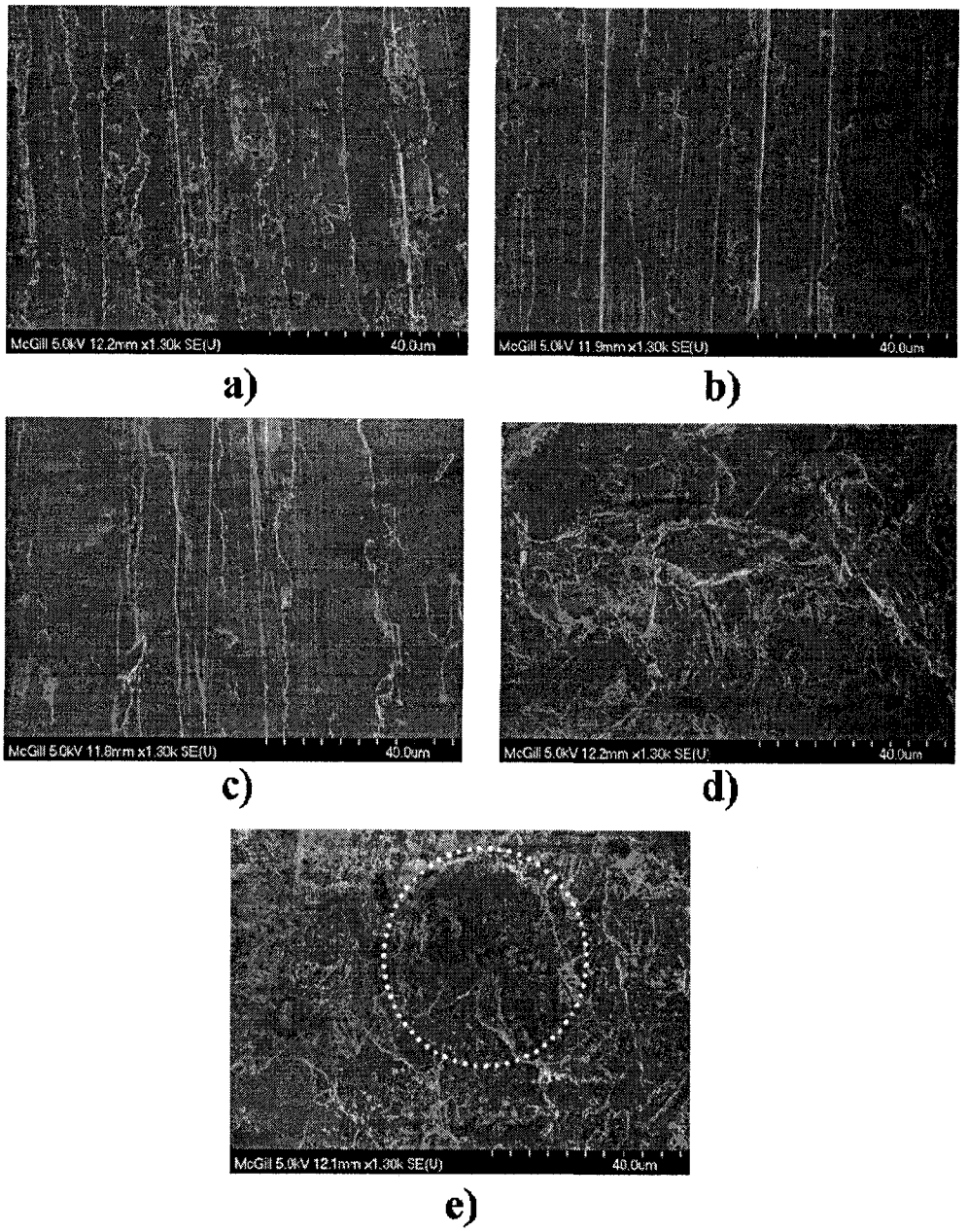

Figure 5.3 a) SEM images of E-36-IIel cathodes; b) SEM images of E-95-IIel cathodes; c) SEM images E-195-IIel cathodes; d) SEM images of G-190 cathode, dotted circle shows the individual features present on the cathode; e) SEM images of G-708 cathode, dotted circle shows the individual features present on the cathode.

5.3.2 Arc erosion measurements

Table 5.2 summarizes the erosion rates reported in the literature for pure massive Cu. For arcs of 100 to 125 A, in 10^{-6} Torr vacuum, an erosion rate of the order of 100 μg/C, is generally agreed upon [4]. In all the references cited in table 5.2, the authors do not report on any special surface roughness preparation or measurement and hence we consider that the cathodes tested had machine finished surfaces (formed after cold rolling).

Figure 5.4 shows the erosion rates and the Ra values measured on the cathodes tested in this study. The error bars reported in figure 5.4 are the standard deviations of the values obtained from three separate measurements. To maintain identical conditions, a constant arc current of 125 A for a duration of 500 μs was maintained for each pulse and a total of 135 arc pulses were run on each cathode to calculate the erosion rate. To account for the loss of material due to the 1000 ns laser pulse, which was used to initiate the arc, the weight loss of the cathode was determined under identical experimental conditions, by imposing 135 laser pulses on the machine finished pure Cu with no arcs. This weight loss, which was ~ 15% of the total weight loss, was removed before calculating the erosion rates.

In figure 5.4, for both E-cathodes and G-cathodes tested, we see that the erosion rate decreases with the Ra values. In the group of E-cathodes, E-36 μm cathodes have the lowest Ra value of 0.86 μm and also have the lowest erosion rate of 30 μg/C. Similarly in the G-cathodes group, G-190 μm cathodes have the lowest Ra value of 3.30 μm and gave an erosion rate of 33 μg/C.

Table 5.2 Erosion rates of pure massive Cu reported in the literature.

	Reference	Arc Current (A)	Vacuum level (Torr)	Erosion rate (μg/C)
1	Plyutto et., al. [22]	120	1×10^{-6}	130
2	Kimblin et., al. [23]	80	1×10^{-6}	115
3	Boxman R.L. [4] (page 233-234)	125	1×10^{-5}	90
4	Meunier J. L. et., al. [24]	≤300	1×10^{-6}	70-80

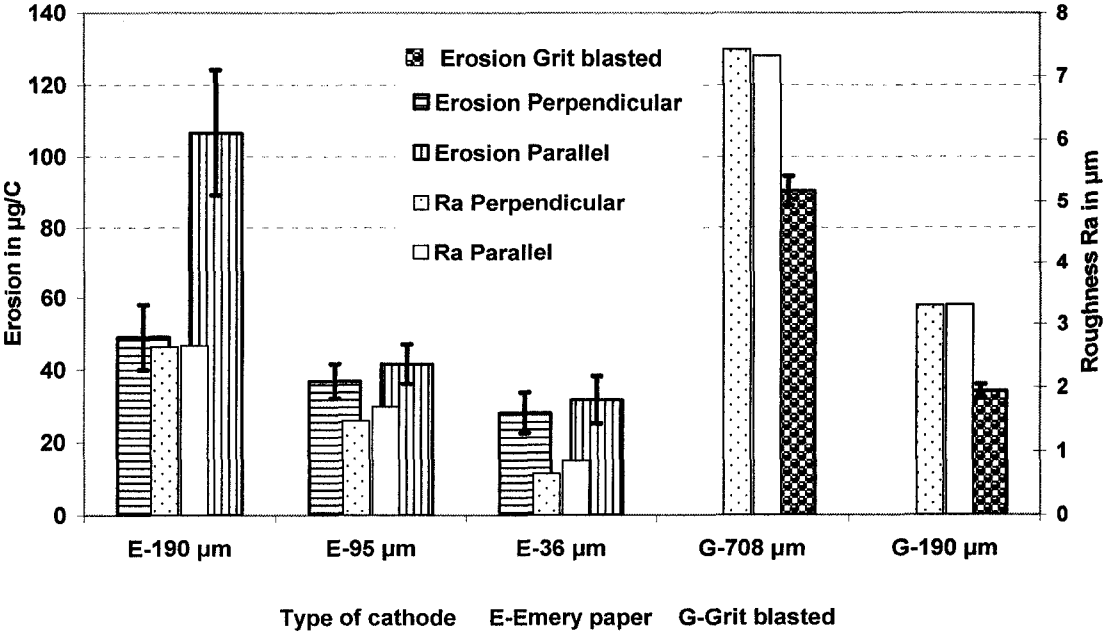

Figure 5.4 Erosion rate and roughness levels of cathodes prepared by emery paper and grit blasted cathodes.

5.3.2.1 Comparison between parallel and perpendicular patterns on E-cathodes

In figure 5.4, for any particular grit used, we see that the average erosion rate (average of three individual measurements) of cathodes having perpendicular patterns is lower than the average erosion rate of cathodes with parallel patterns. Although, error bars for both E-95 μm cathodes and E-36 μm cathodes overlap, we clearly see that E-190-ular cathodes have an average erosion rate of 45 μg/C whereas E-190-llel cathodes have an erosion rate of 106 μg/C. This trend can be explained by analyzing the arc traces formed on these cathodes and is discussed in detail below.

Figure 5.5 shows the images of the arc trace left on the cathodes after 135 arc pulses. For all the cases, multiple arcs were initiated at different vertical positions on the cathode by moving it vertically. Once the arc was ignited, a permanent U-shaped magnet moved the arc down in the retrograde direction as shown by an arrow in figure 5.5. Figures 5.5a and 5.5b are SEM images of the arc trace on E-190-ular surface and E-190-llel surface respectively. From figure 5.5, we can clearly see that arc trace formed on cathode with perpendicular patterns is wider compared to the arc trace formed on cathodes with parallel pattern. The arc trace formed on parallel patterns is made up of individual arc traces either separate and/or overlapping on one another which are very narrow compared to their perpendicular pattern counterpart. From detailed analysis of the arc trace under an optical microscope, we noticed that, on both parallel and perpendicular patterned cathodes, the arc trace clearly follows the surface patterns created. Similar to what we observe, researchers have reported earlier in the literature that the vacuum arcs tend to follow the surface scratches [1, 13-16, 19 and 20]. That is, vacuum arcs which are composed of many individual current carrying micro/macro-attachment points (cathode spots), move by successive initiation and extinction of cathode spots. It is well documented that new cathode spots always initiate along a surface scratch, if present [13-16, 19 and 20]. So, on E-cathodes with perpendicular patterns, the natural tendency of the arc is to move sideways on the cathode, but the B field created by the permanent magnet pushes the arc downwards. Due to the combined effect of these two, the arc attachment on the surface becomes wider, resulting in a wider arc trace relative to the arc trace

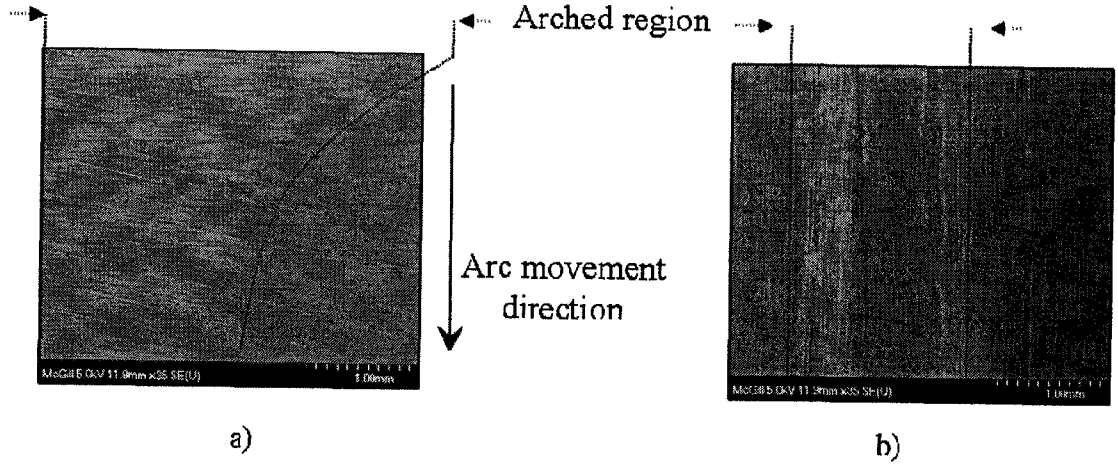

Figure 5.5 a) arc trace formed on E-190-ular cathode; the brighter region between the dotted lines is the arc trace; b) arc trace formed on E-190-llel cathode; the brighter region between the dotted lines is the arc trace. The solid arrow shows the direction of arc movement.

formed on E-cathodes with parallel patterns. On E-cathodes with parallel patterns, the B field force is in the same direction as the surface pattern which also happens to be the natural direction of arc movement. Hence on E-cathodes with parallel patterns, the final arc trace is narrow.

If one were to analyze the arc motion at the micro level, the arc once ignited on a surface with perpendicular patterns, would start on a particular ridge (say i_{th} ridge) and tend to move sideways. That is new cathode spots would be created one next to the other along the i_{th} ridge. Now due to the B field force, the cathode spot would jump from i_{th} ridge to $(i+1)_{th}$ ridge, which is right below the i_{th} ridge, and then start to move sideways on this $(i+1)_{th}$ ridge. Further, it would jump down again to $(i+2)_{nd}$ ridge and so on. If the above argument were true, then the SEM observations of the arc trace should reveal macro craters formed only along the ridges. Figure 5.6 shows the SEM pictures of the arc trace formed on E-190-ular pattern. Figure 5.6a through 5.6d shows the successive images increasing magnification of the arc craters formed (the magnified section is shown by a rectangle as we proceed from image to image). We can clearly see that the macro craters are only present along the scratches and that the regions between the ridges are free from

arc craters. These pictures support the above argument. Similar results were seen on both E-95-ular and E-36-ular cathodes.

Extending the above argument, if the average distance between the i_{th} and $(i+1)_{th}$ ridge is increased, then the arc has to jump a larger vertical distance as it moves down the cathode. This should result in a higher residence time of the arc on the i_{th} ridge before jumping onto the $(i+1)_{th}$ ridge. It is well documented in the literature that the erosion of cathodes is a heat transfer problem. Higher arc residence time on the cathode results in higher erosion rates [25]. As shown in figure 5.3, when we move from E-36-ular cathodes to E-190-ular cathodes, in addition to increasing the roughness level, we are also increasing the average separation between the unidirectional ridges formed. Thus, one would expect higher erosion rates on E-190-ular cathodes than on E-36-ular cathodes. The erosion rates results reported in figure 5.4 support this argument.

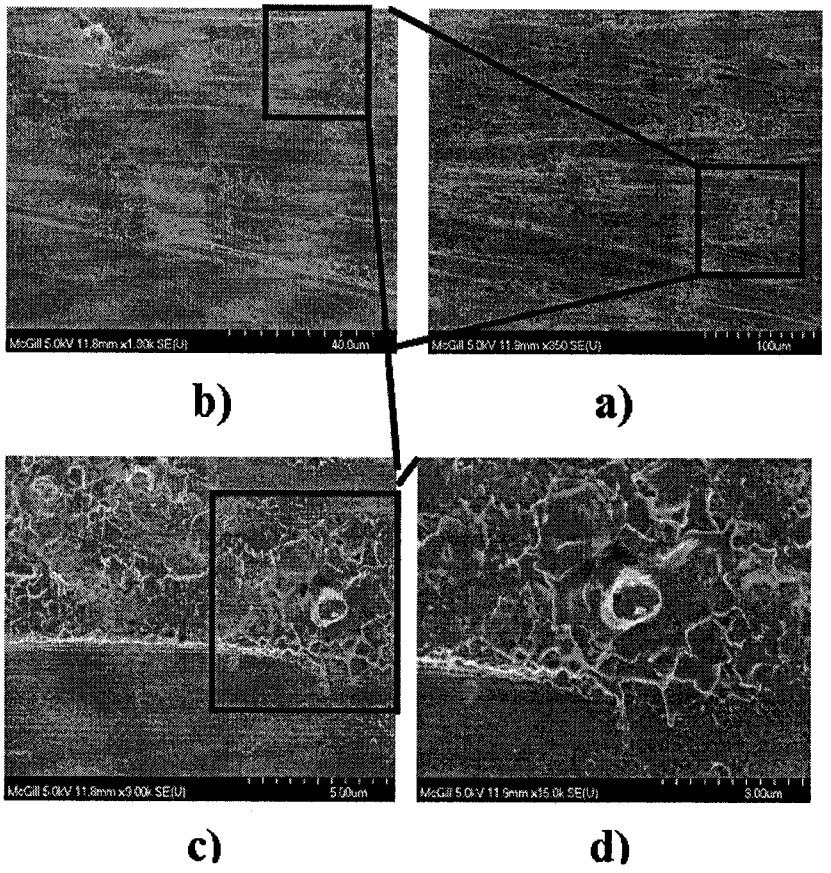

Figure 5.6 a) through d) shows the SEM images of the arc craters formed on E-190-ular cathode.

Analyzing the arc motion on the cathodes with parallel patterns, the arc once ignited would move along a particular ridge and the cathode spots would line up one below the other. This should result in multiple overlapping craters and also result in increased local heating of the cathode. Figure 5.7 shows the SEM pictures of the arc trace formed on E-190-llel pattern. Figure 5.7a through 5.7d show the successive images of the arc craters formed. We can clearly see from these images is that the arc craters are lined up one below the other. Larger overlapping craters are clearly visible in figure 5.7d. Due to the combined effect of increased local heating and formation of multiple arc craters one above the other, the E-190-llel cathode gives higher erosion rate in comparison with its counterpart E-190-ular. On E-190-ular cathodes, the arc craters are more distantly spaced as is seen in figure 5.6 and this result in better heat dissipation on the cathode surface giving lower erosion rates. Similar crater formations were observed on E-95-llel and E-36-llel cathodes.

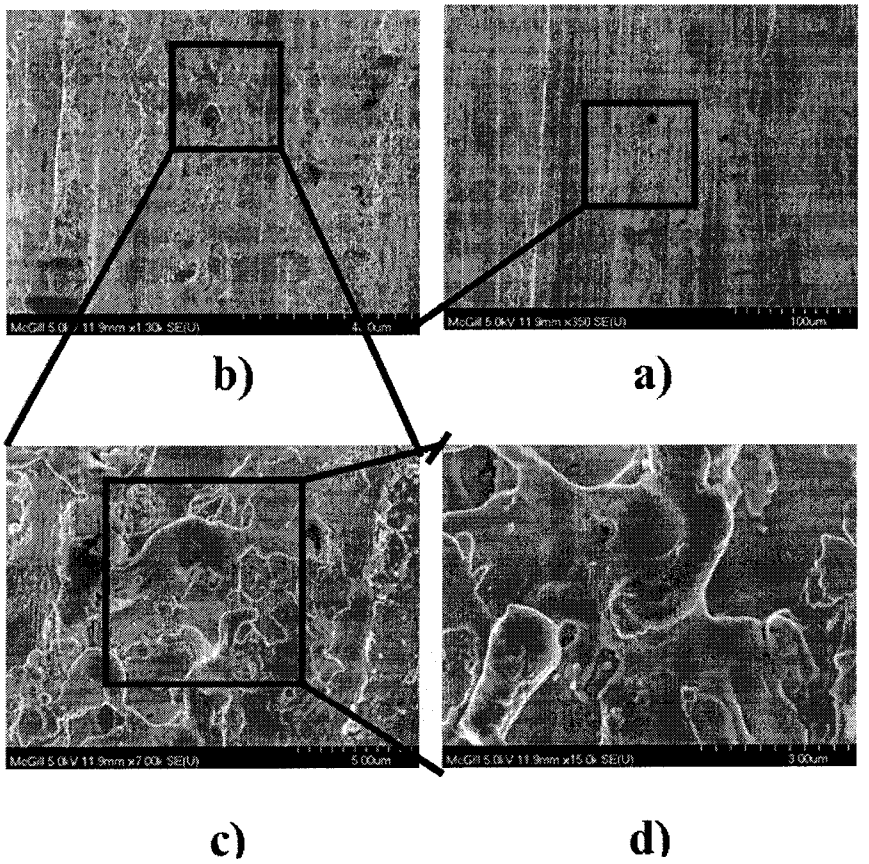

Figure 5.7 a) through d) shows the SEM images of the arc craters formed on E-190-llel cathode.

We notice from figure 5.4, between E-95 μm and E-36 μm cathodes, though there is a significant reduction in the roughness levels, there is only a slight reduction in the erosion rates. The erosion error bars on all these cathodes overlap showing a plateau effect in the erosion rate with roughness level. This result is attributed again to the nature of arc attachment and the surface patterns. If the dimensions of the surface pattern start to become comparable to the size of the macro craters formed, then the original surface roughness and pattern created would be destroyed in the first few passages of the arc. This would result in a constant roughness irrespective of the original roughness level/pattern. Figure 5.8 shows the SEM images on E-95-ular and E-36-llel cathodes. Here we can see that the arc craters formed have destroyed the initial pattern in spite of the fact that both the grit size used and pattern formed were different. Hence the overall erosion rate measured on these cathodes would be the same irrespective of their initial roughness level.

In pulsed vacuum arc experiments, arc velocity is generally calculated by dividing the length of the arc trace with the pulse duration [18-21]. Fu et. al., [18-20] working on similar studies as ours, observe higher arc velocities on cathodes having parallel patterns. Generally, higher arc velocities result in a lower residence time of the arc, and lower erosion rates. As shown in figure 5.4, the parallel patterned cathodes have higher erosion rates which are counterintuitive. Although the arc velocities on the parallel patterned cathodes may be higher, the overall erosion rates are also higher due to the formation of over lapping craters and increased local heating.

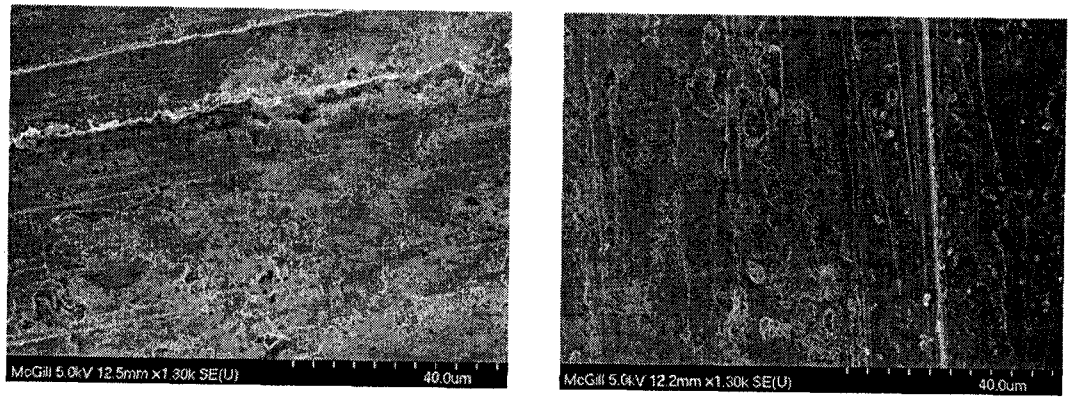

Figure 5.8 a) SEM image of arc trace formed on E-95-ular cathode; b) SEM image of arc trace formed on E-36-llel cathode.

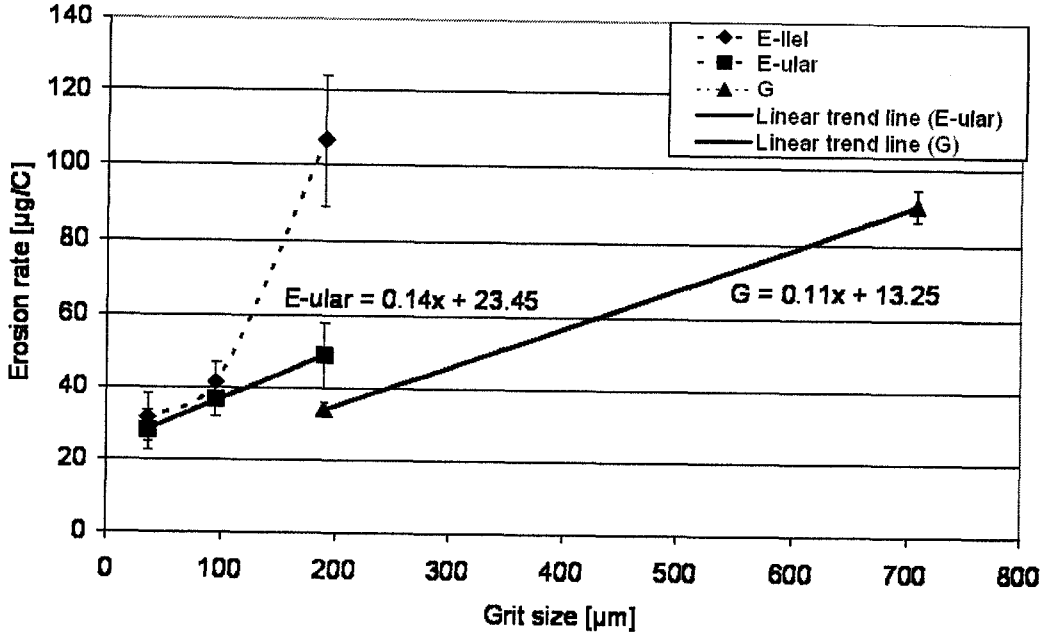

Figure 5.9 Erosion rate vs. grit size used. Notice the linear trend lines added on both E-ular and G cathodes have similar slopes.

5.3.2.2 Erosion rates on G-cathodes and comparison with E-cathodes

Figure 5.9 shows a plot of erosion rate vs. grit size used. From figures 5.2 and 5.9, we can see that the erosion rates of G cathodes also show a similar trend with roughness as E cathodes. That is, the erosion rate increases with the Ra. G-708 µm cathodes which have

an Ra value of 7.32 μm gives an erosion rate of 90 μg/C whereas G-190 μm cathodes which have an Ra value of 3.31 μm gives an erosion rate of 33 μg/C. The reason for this trend is again explainable by the surface features present on the cathodes as shown in figure 5.3d and 5.3e. G-708 μm cathodes having larger surface features give higher erosion rates when compared to G-190 μm cathodes which have smaller surface features.

From figure 5.9, we can see that the G-190 μm cathodes have Ra value of 3.31 μm which is slightly greater than the Ra value of 2.67 μm for E-190 μm cathodes. As shown in table 5.1, the grit size used to prepare both G-190 μm and E-190 μm cathodes was 190 μm. G-190 cathodes, which have an isotropic pattern give lower erosion rates when compared to E-190 cathodes which have a unidirectional pattern. We see from figure 5.4 that the average erosion rates of G-190 μm cathodes is 33 ± 2 μg/C whereas the average erosion rate of E-190-ular cathodes is 49 ± 9 μg/C. Also, we can see from the added trend lines, that the slopes for both E-ular and G cathodes are similar. However, the erosion rates do not scale with the Ra values for E and G cathodes. G-708 μm cathodes which have the highest Ra value of 7.42 μm has an average erosion rate of 90 μg/C whereas E-190-llel cathodes which has Ra value of 2.67 μm, also has average erosion rate of 108 μg/C. The reason for this behavior is not known at this point, but is probably due to the arc motion on isotropic roughness.

Figure 5.10 shows the SEM images of the arc craters formed on G-190 μm and G-708 μm cathodes. The arc craters formed on G-190 μm cathodes are smaller in dimension (~2 microns) relative to the arc craters formed on G-708 μm cathodes (~3 to 4 microns). Similar to earlier reports in the literature, formation of large craters is consistent with higher erosion rates [26].

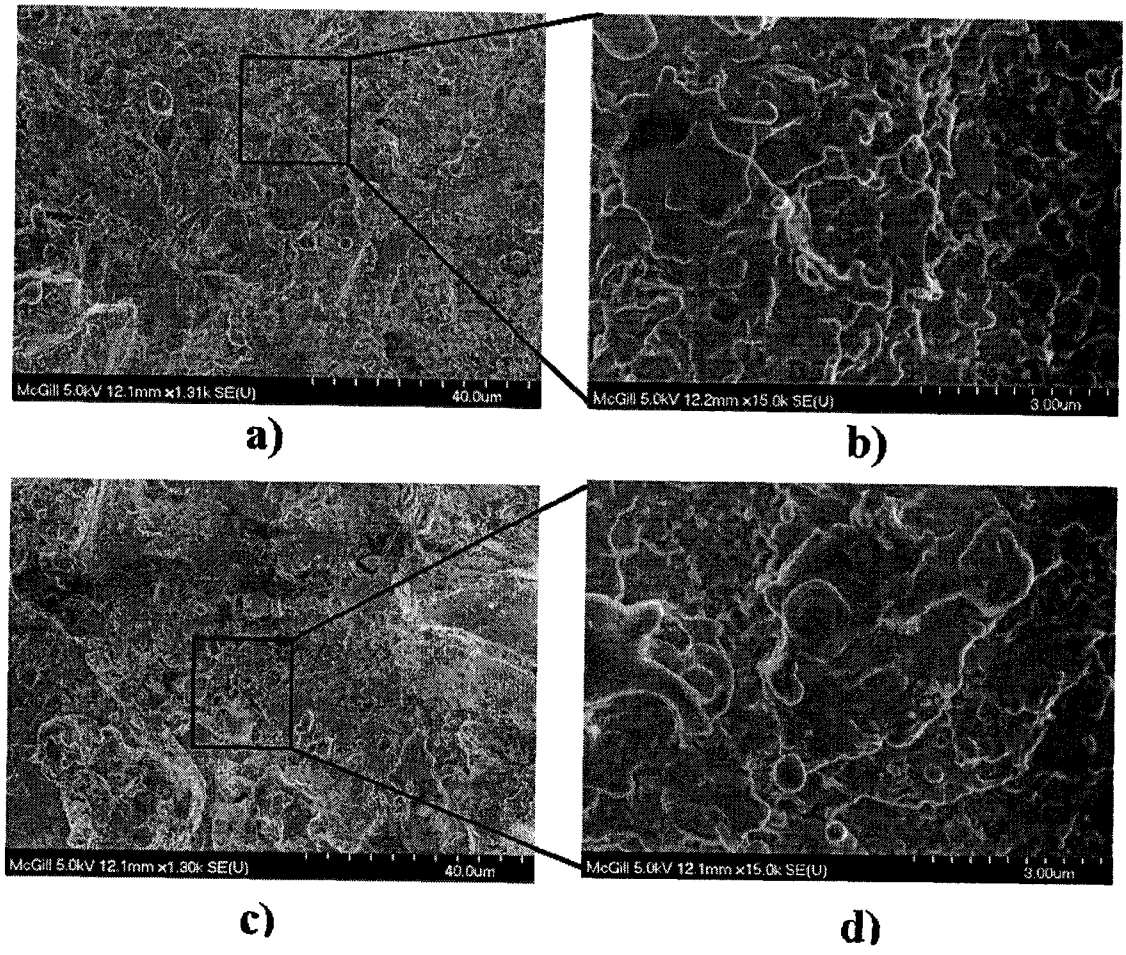

Figure 5.10 a) and b) are SEM images of the arc craters formed on G-190 cathodes; c) and d) are the SEM images of the arc craters formed on G-708 cathodes.

5.4 Conclusions

We conclude that:

- For both E and G cathodes tested, vacuum erosion rates reduce with reducing surface roughness levels.
- Both surface roughness and surface patterns affect the erosion rates. Having surface patterns perpendicular to the direction of arc motion results in lower erosion rates. Cathodes with perpendicular patterns gives lower erosion rates due to a wider arc attachment. This results in reduced local heating and better heat dissipation on the cathode surface.

- Erosion rates depend chiefly on the nature of arc attachment and arc movement on the cathode. At any roughness level, having regular patterns in the direction of arc movement, results in overlapping craters and higher erosion rates. Isotropic surfaces promote random motion and hence give lower erosion rates.

5.5 Acknowledgements

The authors express their gratitude to Dr. Jean-Luc Meunier of McGill University, Chemical Engineering Department, Montreal, Canada, for valuable suggestions and discussions. The financial support of the Natural Sciences and Engineering Research Council of Canada for the work is gratefully acknowledged.

5.6 References

1. Daalder J E 1978 Cathode erosion of metal vapour arcs in vacuum PhD thesis submitted to Eindhoven University of Technology Netherlands
2. Boxman R L Twenty-five years of progress in vacuum arc research and utilization 1997 *IEEE transactions of plasma science,* **25** 6 1174-1186
3. Farrall G A 1980 Electrical breakdown in vacuum. Arcs: Theory and Application ed J M Lafferty (New York: Wiley)
4. Boxman L R, Sanders D M and Martin P J 1995 Handbook of vacuum arc science and technology: fundamentals and applications (New Jersey: Noyes publications)
5. Beilis I I 2001 State of the theory of vacuum arcs *IEEE transactions of plasma science* **29** 5 657-670.
6. Schmoll R 1998 Analysis of the interaction of cathode micro protrusions with low-temperature plasmas *J. Phys. D: Appl. Phys.* **31** 1841-1851
7. Farrall G A 1985 Electrical breakdown in vacuum *IEEE Transaction on electrical insulation* **20** 815-841
8. Guile A E and Hitchcock A H 1978 The erosion of copper cathodes from vacuum to atmospheric pressure arcs *Journal of applied physics* **49** 7 4275-4276
9. Ding B, Yang Z and Wang X 1996 Influence of microstructure on dielectric strength of CuCr contact materials in vacuum *IEEE Transactions on Components, Packaging and Manufacturing Technology Part-A* **19** 1 76-81
10. Wang Y P and Ding B J 1999 The preparation and their properties of microcrystalline and nanocrystalline CuCr contact materials *IEEE Transactions. CPT* **22** 467–72
11. Wang Y, Zhang C, Zhang H, Ding B and Lu K 2003 Effect of the microstructure of electrode materials on arc cathode spot dynamics *J. Phys. D: Appl. Phys* **36** 2649-2654

12. Zhang C, Yang Z, Wang Y and Ding B 2003 Cathode spot propagation on the surface of amorphous, nanocrystalline and crystalline $Cu_{60}Zr_{28}Ti_{12}$ cathodes *Physics Letters A* **318** 435–439
13. Cobine J D and C J Gallagher 1948 Current density of the arc cathode spot *Phys. Rev.* **74** 10 1524-1530
14. Juttner B, Pursch H and Shilo V A 1984 The influence of surface roughness and surface temperature on arc spots movement in vacuum *J. Phys. D: Appl. Phys* **17** L31-L34.
15. Reece M P 1956 Arcs in vacuum *Nature* **177** 1089-1090
16. Germer L H and W S Boyle 1955 Anode and cathode arcs *Nature* **176** 1019
17. Daalder J E 1974 Diameter and current density of single and multiple cathode discharges in vacuum *IEEE Trans. Power Appar. Syst.* **PAS-93** 1747-1758
18. Daalder J E and Vos C W M 1972 Distribution functions of the spot diameter for single and multi cathode discharges in vacuum Eindhoven University of Technology Eindhoven Netherlands Rep 72-E-32
19. Fu Y H and Smeets R P P 1989 The influence of contact surface microstructure on vacuum arc stability and voltage *IEEE Transactions on plasma science* **17** 5 727-729
20. Fu Y H 1989 The influence of cathode surface microstructure on DC vacuum arcs *J. Phys. D: Appl. Phys* **22** 94-102.
21. Lakshminarayana Rao, Munz R J and Meunier J-L 2007 Vacuum arc velocity and erosion rate measurements on nanostructured plasma and HVOF spray coatings *J. Phys. D: Appl. Phy* **40** 4192-4201.
22. Plyutto A A, Ryzhkov V N and Kapin A T 1965 High speed plasma streams in vacuum arcs *Soviet physics-JET* **20** 2 328-337
23. Kimblin C W 1974 Cathode spot erosion and ionization phenomena in the transition from vacuum to atmospheric pressure arc *Journal of applied physics* **45** 12 5235-5244
24. Meunier J-L and Drouet M G 1987 Experimental study of the effect of gas pressure on arc cathode erosion and redeposition in He, Ar and SF_6 from

vacuum to atmospheric pressure *IEEE transaction of plasma science* **PS-15** 5 515-519

25. Szente R N, R J Munz and Drouet M G 1992 Electrode erosion in plasma torches *Plasma Chemistry and Plasma Processing* **12** 3 327-343.
26. Daalder J E 1975 Erosion and the origin of charged and neutral species in vacuum arcs *J. Phys. D: Appl. Phys* **8**, 1647-1659

Chapter 6 Vacuum arc velocity and erosion rate measurements on nanostructured plasma and HVOF spray coatings

This chapter presents the erosion behavior of pure Cu coatings which have nanostructure grain distribution prepared from thermal spray methods. The powders and the thermal spray methods used to produce nanostructured coatings are described along with the characterization of the coatings produced. Pulsed vacuum arc setup and the erosion results are presented. Microstructural analysis of the arc trace and the coatings after the erosion experiments are presented.

The results indicate that the nanostructured coatings have up to 50% lower erosion rates compared to massive Cu having relatively large grain size. Spalling of the coating under the vacuum arc contributed to higher erosion rates for one of the coatings tested. These coatings produced by atmospheric pressure thermal spray techniques in air have intersplat oxide content along with their nanostructured grains. Hence the results cannot isolate effect of microstructure alone on the erosion behavior. This issue of oxide content is addressed in chapter 7 and 8.

Abstract

Arc velocity and erosion rate measurements were performed on nanostructured pure Cu cathodes in 10^{-5} torr vacuum (1.3324 mPa), in an external magnetic field of 0.04 T. Five different kinds of nanostructured cathodes were produced by spraying pure Cu powders of three different sizes, on Cu coupons by atmospheric pressure plasma spraying and high velocity oxygen fuel spraying techniques. The erosion rates of these electrodes were obtained by measuring the weight loss of the electrode after igniting as many as 135 arc pulses, each of which was 500 μs long at an arc current of 125 A. The arc erosion values measured on three kinds of nanostructured coatings were 50% lower than the conventional pure massive Cu cathodes. Microscopic analyses of the arc traces on these nanostructured coatings show that the craters formed on these coatings were smaller than those formed on conventional Cu (<1 micron in diameter compared to 7-12 microns

diameter on conventional Cu). It was concluded that nanostructured cathodes had lower erosion rates than conventional pure Cu cathodes.

6.1 Introduction

Vacuum arcs have been extensively studied over the past twenty five years for their many applications including high-current vacuum switching, vacuum arc deposition of hard coatings, vacuum arc degassing and re-melting of metals [1, 2]. Erosion of cathodes in vacuum arc devices severely limits their useful operation time. Intensive experimental and theoretical studies of vacuum arcs have revealed that many parameters such as magnetic field strength, geometry of the cathode, inter electrode gap, operating vacuum, plasma forming gas, arc current, surface chemistry and electrode microstructure affect the nature and extent of cathode erosion [3-8]. Researchers have shown that the surface properties such as surface micro-protrusion, roughness, impurity inclusions and microstructure of the cathode, meaning the grain size, second phase or particles, features like solute concentration and defect structure significantly effect break-down voltage and dielectric strength [9-14]. Wang et al., [15-17] working with nanostructured CuCr alloy cathodes and $Cu_{60}Zr_{28}Ti_{12}$ cathodes have observed that the erosion rate on these electrodes were lower than conventional electrodes (4%-20% less than pure Cu). They have reported that the arc attachment points on these electrodes moved significantly faster and covered most of the surface of the cathode.

In this paper, we report on the erosion values, arc velocities and on the arc craters formed on nanostructured Cu cathodes. Nanostructured cathodes were prepared by atmospheric pressure plasma spraying and high velocity oxygen fuel spraying of pure Cu powders onto Cu substrates. The coatings formed were characterized for their grain size, porosity, thermal conductivity and oxide content. At the micro-scale, the coatings formed appeared as the stacking of well flattened lamellae and the grains inside each lamella were submicron sized, ranging from 100 nm to 300nm. Vacuum arc erosion and arc velocity values were determined and the arc craters formed on these electrodes were analyzed using a field emission scanning electron microscope, FE-SEM (Hitachi-4700). The results obtained were compared to the literature values for pure massive Cu. The results

obtained from the work leads us to conclude that coatings having similar grain sizes show similar erosion values. The details are presented below.

6.2 Materials and experimental methods

Three different commercially available Cu powders viz., Metco-55 (99.99% pure; further referred as M-55), Diamalloy-1007 (99.99% pure; further referred as D-1007) and Cerac-1133 (99.9% Cu and 0.1%Te; further referred as C-1133) were used as spray powders. The morphology and size distribution of the powders were determined by scanning electron microscopy (SEM) and Mastersizer-2000 respectively. Distilled water was used as dispersant in the Mastersizer for size distribution analysis. Energy dispersive spectroscopy (EDS) and inductively coupled plasma mass spectroscopy (ICP) techniques were used to determine the chemical composition of the powders.

The characterized powders were sprayed using atmospheric pressure plasma spraying (PS) and high velocity oxygen fuel spraying (HVOF) methods. All the three powders were sprayed by PS whereas only M-55 and D-1007 powders were used for HVOF spraying. The particle size of the C-1133 powder was so small that the particles melted and agglomerated when injected internally in either plasma or HVOF torch nozzle. Plasma spraying by injecting into the plasma plume external to the torch nozzle was possible whereas C-1133 was excluded for the HVOF spray technique. Powders for all other coatings were injected into the torch nozzle. The spray conditions used for the two methods are summarized in table 6.1. During spraying, the substrate was cooled by jets of cold nitrogen and the temperature of the substrate was measured using a pyrometer. Two different substrates viz., square copper plates (60mm × 60mm × 2.5mm) and square aluminum plates (35mm × 35mm × 3mm) were used. Both the substrates were grit blasted with 800 micron alumina grits just before coating and had a surface roughness Ra = 8.58 microns. The coated copper plates were further cut and used as specimens for microscopic analysis and also as electrodes for arc velocity and arc erosion measurements. The coatings formed on aluminum substrates were separated from the substrate by dissolving the aluminum in 40% KOH solution, to obtain free-standing

specimens for thermal diffusivity measurements by the laser flash method as explained in [18]. Thermal diffusivity values were converted to thermal conductivity by considering the properties of pure Cu (ρ = 8900 kg/m3, Cp = 386 J/kg K, K = 398 W/m K).

Table 6.1 Spray conditions

Parameters	Plasma spraying	HVOF spraying
Spray distance	3 inches (76.2 mm)	14 inches (355.6 mm)
Transverse speed	24 inches per sec (0.61 m/s)	30 inches per sec (0.76 m/s)
System settings	Propellant gas: Ar 388.89 kPa, 298 K, 58.0 lpm Carrier gas: Ar 241.32 kPa, 298 K, 5.0 lpm Arc current (I) :700 A Power (V×I): 21 kW Nozzle diameter : 0.3125 inch (7.9375 mm)	Kerosene (K) : 0.28 lpm Oxygen (O_2) : 967 lpm Stochiometry O_2: K: 5.64:1 (wt %) Combustion pressure: 58.05 kPa

For microscopic analysis, the coatings on Cu substrates were cut using Struers 'Secotom-10', a universal precision cut off machine and vacuum mounted in cold setting resin. The mounted specimens were wet ground using SiC paper #800, 1200 and 4000 under running tap water. The ground samples were polished using 3 microns and 0.04 microns silica suspensions. The polished samples were etched by a $FeCl_3$ etchant (2.5g of $FeCl_3$ + 10ml of HCl + 50ml of ethanol) for 5 seconds. The etched coatings were examined under optical microscope and SEM to determine their microstructure. To determine the porosity of the coatings, as many as 10 SEM pictures of polished coatings (prior to etching) were taken at regular intervals on each of the coatings and the porosity of individual pictures was measured by an image analysis technique. An average of these numbers were calculated and reported as porosity with a standard deviation of ± 5%.

The coatings formed on Cu plates were cut into rectangular strips of 60mm × 12 mm to use as cathodes in a pulsed arc chamber. The schematic diagram of the experimental setup used for this study is shown in figure 6.1. It consisted of a vacuum chamber, a power supply unit and a pulsed laser system. Vacuum chamber was an eight port cross of 23 cm diameter, which held the rectangular strip cathode mounted parallel to a rectangular Cu anode (50mm × 10mm × 3mm). Before the start of each experiment, the electrodes were placed in the chamber, maintaining an inter-electrode gap of 5 mm and the chamber was pumped down to 10^{-2} Torr using a mechanical pump. At this vacuum, the reactor was filled with ultra high purity argon and then pumped to 10^{-5} Torr by a mechanical and an oil diffusion pump connected in series. A permanent U shaped magnet (B field = 0.04 T) was positioned behind the cathode to move the arc in the retrograde direction. Capacitors in the arc power supply unit were charged to an open circuit voltage of 200 V. A pulsed arc was initiated on the cathode by a 1000 ns pulse of 10.6 μm infrared laser radiation from a 1.2 kW Diamond™ K-500 CO_2 laser system, supplied by Coherent technologies. A thyristor based electrical switching circuit was used to control a 500 μs arc duration over which, a constant current of 125 A was maintained. This square current pulse was measured using an externally triggered HP-54503A digital oscilloscope. The moving arc left a clear arc trace on the cathode and the velocity of the moving arc was measured by dividing the length of the arc trace with the arc duration time (500 μs). To determine the erosion rate, as many as 135 arc pulses, each 500 μs long with a current of 125 A, were run on the cathode. These pulses were run at a rate of 3-4 pulses per minute. The erosion rate values in grams per coulomb were measured by weighing the cathode before and after the arcing, using a digital balance (accuracy ± 1×10^{-4} grams) and then dividing the weight difference by the total electric charge $Q = \int I\, dt$, passing through the cathode. For each coating, erosion rates and the arc velocities were measured on three individual electrodes. An average of these measured values was recorded and reported as erosion rate and arc velocity.

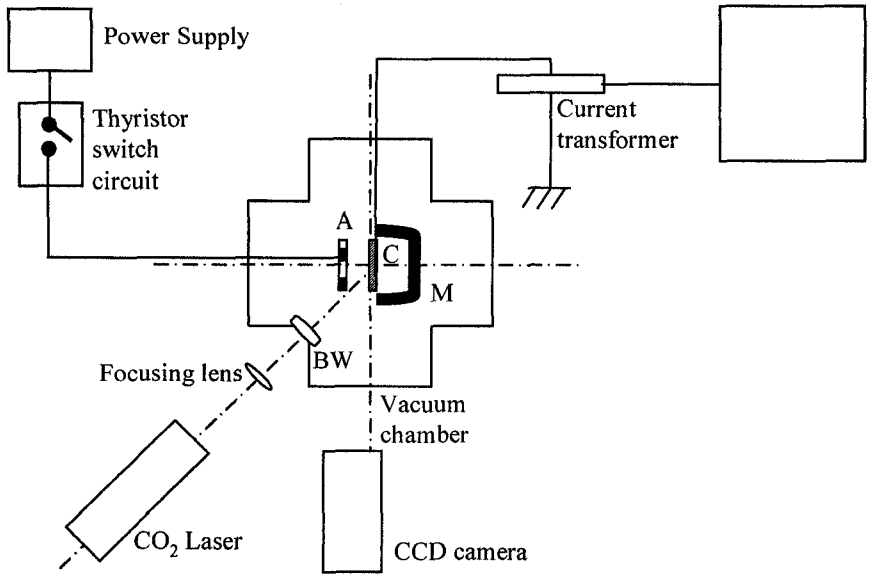

Figure 6.1 Schematic diagram of the experimental setup. A = Anode; BW = Beryllium Window; C= Cathode and M=Permanent Magnet.

6.3 Results and discussion

6.3.1 Characterization of powders

Figure 6.2 shows SEM pictures and particle size distribution results of individual powders. For all the three powders, the size distribution was lognormal. The parameters of the lognormal distribution for individual powders are given in table 6.2. In figure 6.2a, a SEM image of C-1133 shows that the C-1133 particles were irregular in shape. Higher magnification images of the individual particle (inset of figure 6.2a) revealed them as agglomerates with interconnected pores. For C-1133, the size distribution analysis results in figure 6.2b, shows a size range between 0.6 to 60 microns with a maximum at 22 microns. Similar pictures, figure 6.2c, 6.2d and 6.2e, 6.2f were taken for D-1007 and M-55 respectively. These results lead us to conclude that, most of D-1007 and M-55 particles were spheroids though a few irregular shaped particles were also present. Higher magnification images of these particles (not shown here) revealed that the surface of D-1007 particles appeared porous with no interconnection whereas, images of M-55 revealed that they had no pores on the surface. The size range of D-1007 particles was between 30 to 100 microns with a maximum at 60 microns, as shown in figure 6.2d. The

size range of M-55 particles was between 28 to 110 microns with a maximum at 70 microns, as shown in figure 6.2e. The volume weighted mean of C-1133, D-1007 and M-55 particles were 22.8, 83.4 and 102 microns respectively.

Table 6.2 Summary of powder characterization

Powder	μ^a	σ^b	Vol. wtd.mean (μm)	d(0.5)[c] (μm)	d(0.1)[d] (μm)	d(0.9)[e] (μm)	ICP –MS (wt/wt%)	Morphology
C-1133	18	0.46	23.92	22.06	11.82	39.03	0.1% Te	Irregular-Agglomerates
D-1007	53	0.24	83.38	59.34	42.73	86.68	Pure Cu	Spheroidal
M-55	58	0.31	101.69	43.46	71.13	126.65	Pure Cu	Spheroidal

[a] the mass median size.

[b] the natural logarithm of the dispersion indicator.

[c] particle size at 50% of the distribution.

[d] particle size at 10% of the distribution.

[e] particle size at 90% of the distribution.

Both EDS and ICP analyses were carried out on each powder in order to determine the chemical compositions. Figure 6.3a gives the energy dispersive spectrum of C-1133 particles, wherein Cu, O and C peaks can be seen. The oxygen peak was attributed to the surface oxidation of Cu and the C peak to carbon contamination. Back scattered electron (BSE) image of a C-1133 sample showed one particle of higher atomic number and a spot analysis identified it as Te. Figure 6.3b is the EDS result of the Te particle. Cu peaks in figure 6.3b were attributed to the peaks from surrounding Cu particles and C peaks to the carbon contamination. EDS is essentially a surface analysis technique. So a small amount of surface contamination gives high apparent concentrations of the contaminants (O or C in this case). ICP is a bulk analysis and is more reliable. ICP analysis of these powders shows that, C-1133 contains 0.1% (wt/wt %) of Te as contamination. Whereas, D-1007 and M-55 were pure Cu powders with no contaminants present in them. EDS

analysis of D-1007 and M-55 revealed only Cu, O and C peaks similar to figure 6.3a and hence are not reported here. All the above results are summarized in table 6.2.

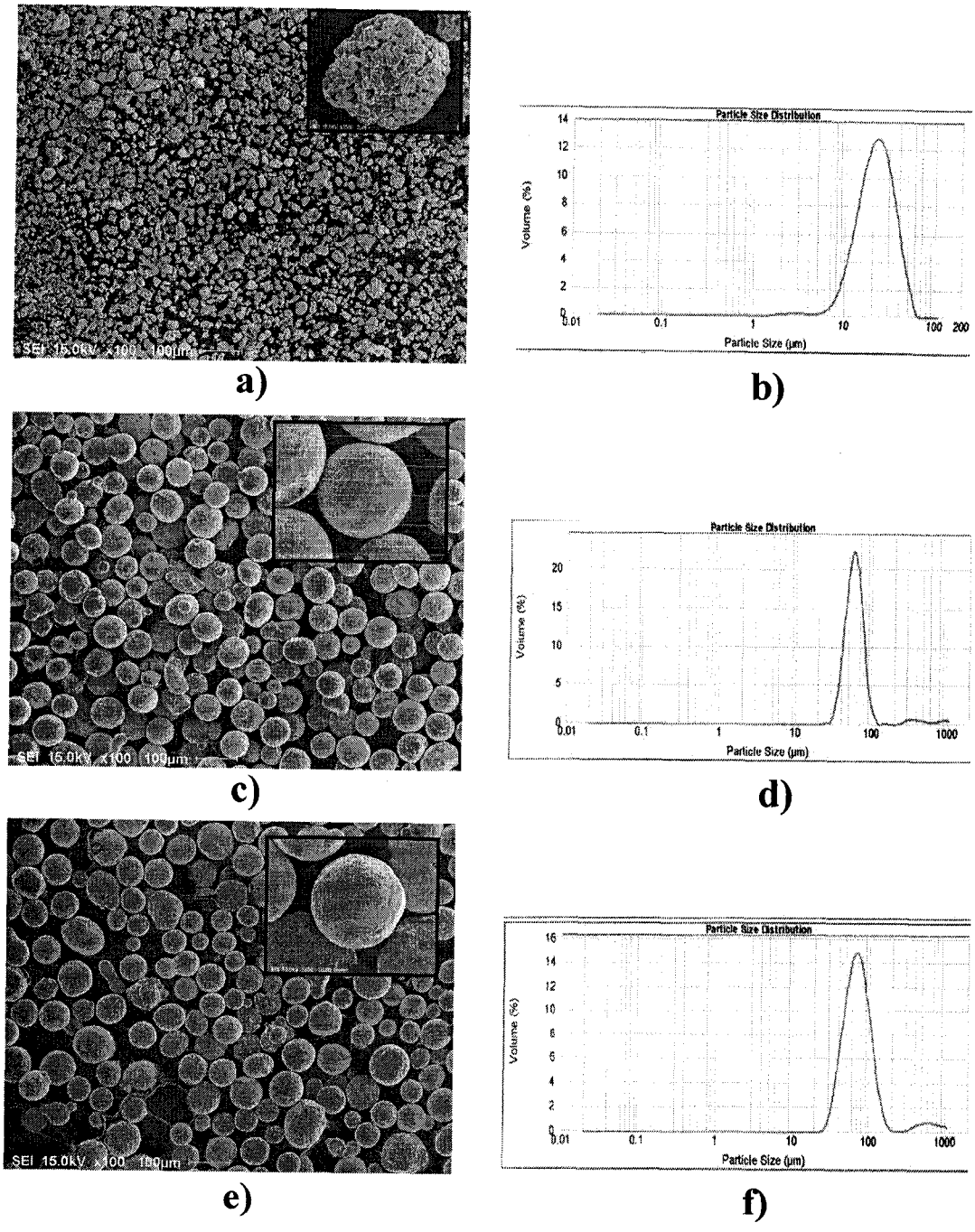

Figure 6.2 a) Morphology of C-1133 ; inset is an image of individual particle; b) size distribution of C-1133; c) morphology of D-1007; inset is an image of individual particle; d) size distribution of D-1007; e) morphology of M-55; inset is an image of an individual particle; f) size distribution of M-55.

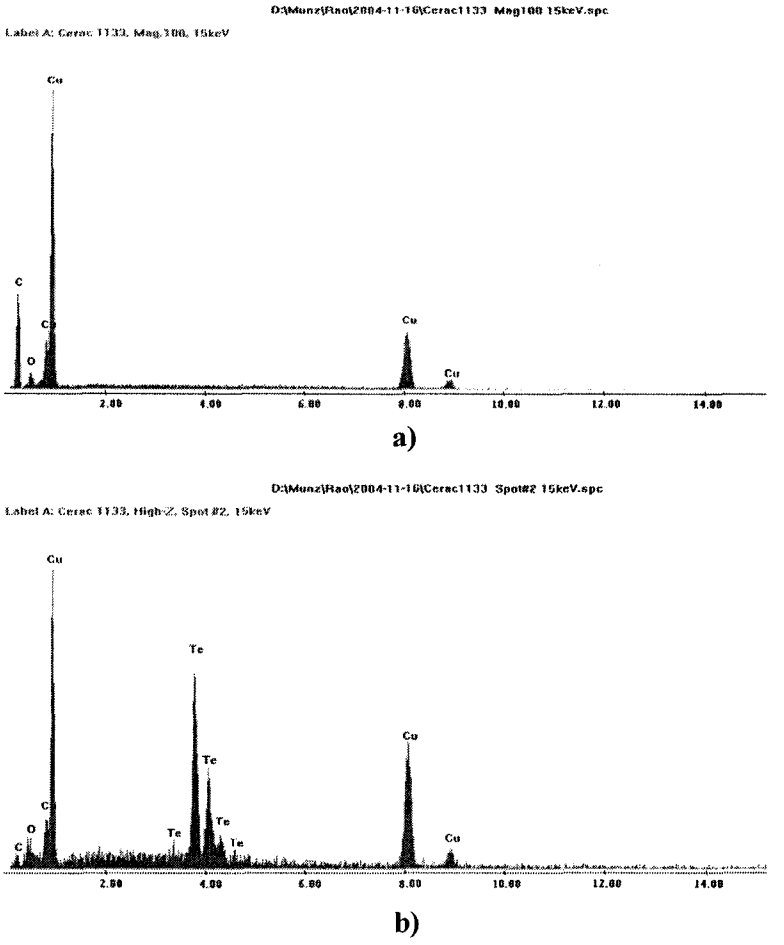

Figure 6.3 a) Energy dispersive spectrum of C-1133; b) Spot analysis result of Te particle

6.3.2 Characterization of coatings

a) Plasma sprayed coatings: Figure 6.4 shows the etched cross sectional low and high magnification images of the plasma sprayed coatings. The coatings were 85% to 93% dense and heavy deformation of the particles from their initially shape was clearly seen from these images. In figure 6.4, grain boundaries and inter-splat boundaries appear dark because of preferential etching. All the coatings appear as stacking of well flattened lamellae with nearly even thickness, which is a characteristic of PS coatings [19]. In all the three cases, the particle-particle interface and the particle-substrate interfaces were clearly visible. In each case, a well deformed particle was elongated to 375 to 430% from

its original diameter and reduced to 4 to 6% from its original thickness. High magnification images, figure 6.4b, 6.4d and 6.4f and their insets, show the fine columnar grains in an individual splat. As C-1133 was the smallest particle with a mean size of 23.9 μm, the grains formed in this coating were also the smallest, less than 100 nm in width. The grains formed from D-1007 and M-55 were 100 to 300 nm thick. These columnar grains were perpendicular to the lamellar direction and were oriented parallel to one another. This proved that, all the three types of particles were sufficiently melted during the spraying process and were cooled at a very rapid rate of 10^7 to 10^8 K/s[19, 20]. Table 6.3 gives the mean temperature of the coating during spraying, the thickness of each coating, the grain size obtained for each powder along with the porosity and the thermal conductivity values. For erosion measurements, the coatings formed were used as sprayed with out polishing and had a surface roughness Ra = 17.5 microns.

Very low magnification images (not shown here) show that, C-1133 had zero non-flattened particles, D-1007 had 2-3 non flattened particles in an optical microscope image of 100 microns dimension bar and M-55 had about 7-8 particles in a similar image. This trend was attributed to the difference in the initial particle diameter which was highest for M-55 and lowest for C-1133. EDS analysis of the coatings showed an oxygen content of 2.1 at% for all the coatings.

Table 6.3 Summary of plasma sprayed coating characterization.

Powder	Mean temperature during coating (deg C)	Thickness (microns)	Grain size (nm)	Porosity (%)	Thermal conductivity (W/m K)
C-1133	130	368	<100-200	7	62
D-1007	110	355	100-300	15	96
M-55	110	337	100-300	11	93

Porosity calculations imply that the coating density varied from 85%, for D-1007 to 93%, for C-1133. M-55 had a coating density of 89%. This trend in porosity can be explained by the presence of non-flattened particles present in the coatings. Thermal conductivity values indicate that both D-1007 and M-55 coatings had similar values, whereas C-1133, which was externally injected during spraying, had lower values.

b) HVOF sprayed coatings: Figure 6.5 shows the etched cross sectional low and high magnification pictures of HVOF sprayed coatings. Both D-1007 and M-55 coatings showed very little porosity, due to high velocity achieved in HVOF technique [21, 22]. In flight surface oxidation of the particles was evident from the dark intersplat regions seen in a back scattered electron (BSE) image of the coatings (not shown here). EDS analysis showed an oxygen content of 2.2 at%. High magnification images of the splats revealed that the splats had columnar grains with their width ranging from 100 to 300 nm. This confirms that all the particles were sufficiently melted during spraying and were cooled at a very high cooling rate. For both D-1007 and M-55, the particle-substrate interface was clearly visible, whereas the particle-particle interface was hard to find in unetched coatings. The coatings appeared as stacking of potatoes with very small inter-particle pores. Table 6.4 summarizes the properties of the coatings. Both D-1007 and M-55 coatings were more than 98% dense and the thermal conductivity values were higher than those of plasma sprayed coatings. A noticeable difference in the HVOF coatings compared to the PS coatings was the orientation of the columnar grains. Unlike PS coatings which had well oriented grains in one direction (parallel to direction of spraying), columnar grains formed on HVOF coatings were oriented in different directions.

In summary, five different coatings were produced starting from three different powders using two different techniques. Four out of five coatings (D-1007-PS, M-55-PS, D-1007-HVOF and M-55-HVOF) had similar grain sizes ranging from 100 to 300 nm thick and one coating (C-1133-PS) had grains smaller than 100 nm. The PS coatings were 85% to 93% dense whereas HVOF coatings were 98% dense. The thermal conductivity values of PS coatings were three times lower in comparison with HVOF coatings. The trend in

thermal conductivity values followed the trend in porosity and both the coatings had oxygen content of ~2 at%.

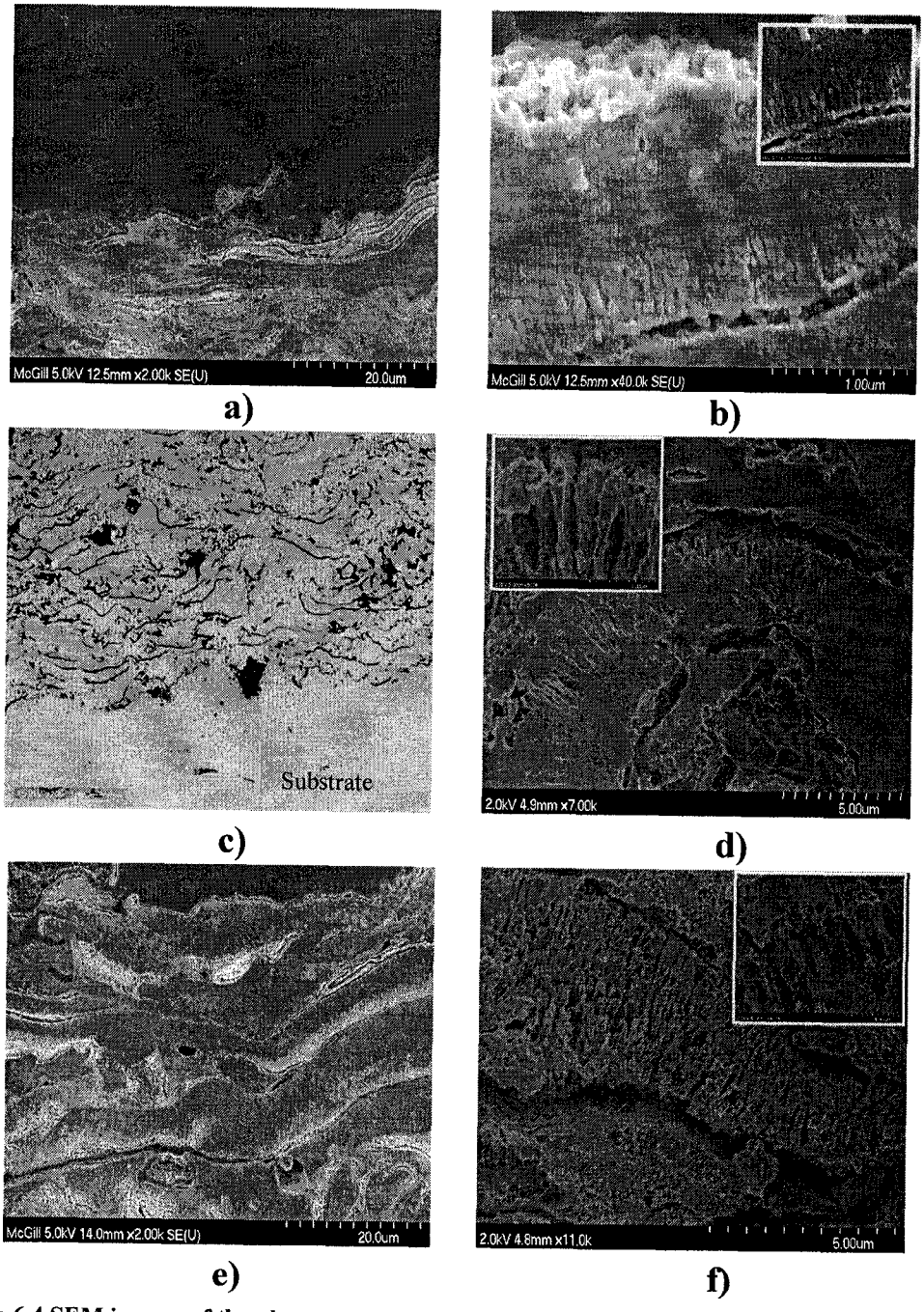

Figure 6.4 SEM images of the plasma sprayed coatings; a, b) low and high magnification pictures of C-1133; c, d) low and high magnification pictures of D-1007; e) and f) low and high magnification pictures of M-55.

Table 6.4 Summary of HVOF sprayed coating characterization.

Powder	Thickness (microns)	Mean temperature during coating (deg C)	Porosity (%)	Thermal conductivity (W/m K)	Grain size (nm)
D-1007	409	125	1.2	302	100-300
M-55	351	125	1.8	236	100-300

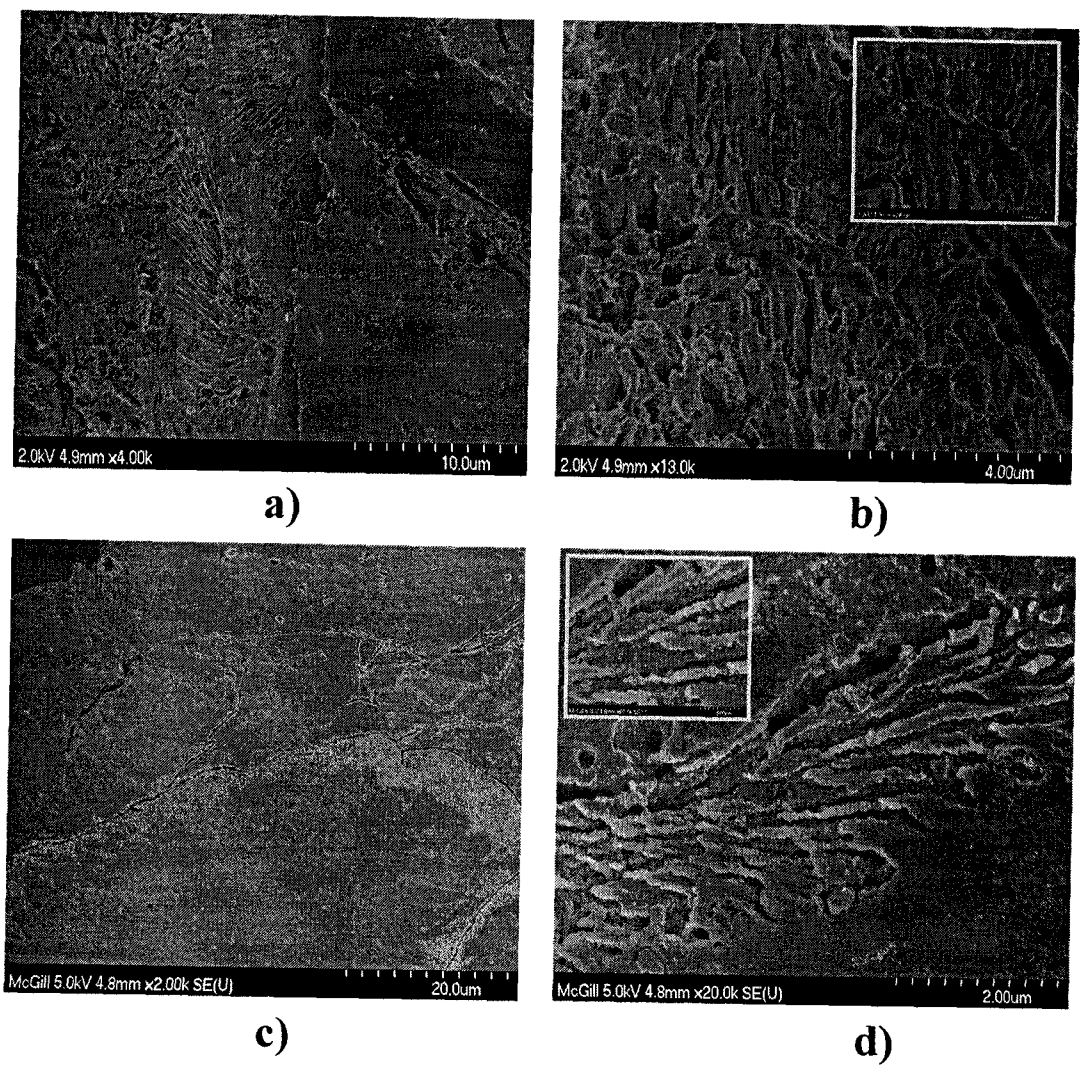

Figure 6.5 SEM images of the HVOF sprayed coatings; a, b) low and high magnification pictures of D-1007; c) and d) low and high magnification pictures of M-55.

6.3.3 Arc velocity and arc erosion results

Table 6.5 summarizes the erosion rates reported in the literature for pure massive Cu. For arcs of 100 to 125 A, in 10^{-6} torr vacuum, an erosion rate of the order of 100 μg/C, is generally agreed upon [5 and references therein].

Figure 6.6 shows the erosion rates and the arc velocity results measured on the coated electrodes. The error bars reported in figure 6.6 are the standard deviations of the values obtained from three separate measurements. To maintain identical conditions, a constant arc current of 125 A for a duration of 500 μs was maintained for each pulse and a total of 135 arc pulses were run on each of the coated electrodes to calculate the erosion rates. To account for the loss of material due to the 1000 ns laser pulse, which was used to initiate the arc, the weight loss of the coatings was determined under identical experimental conditions, by imposing 135 laser pulses on the coatings with no arcs. This weight loss, which was ~ 11% of the total weight loss, was removed before calculating the erosion rates.

Table 6.5 Erosion rates of pure massive Cu reported in the literature.

	Reference	Arc Current (A)	Vacuum level (Torr)	Erosion rate (μg/C)
1	Plyutto et., al. [23]	120	1×10^{-6}	130
2	Kimblin et., al. [24]	80	1×10^{-6}	115
3	Boxman R.L. [4] (page 233-234)	125	1×10^{-5}	90
4	Meunier J. L. et., al. [5]	≤300	1×10^{-6}	70-80

Comparison of plasma sprayed coatings: Except for C-1133 coatings, the other two coatings have erosion values significantly less than that of pure Cu. Coatings D-1007 and M-55 had erosion rates of 51 μg/C and 48 μg/C respectively. The higher erosion rate of C-1133 coating is explained by the physical loss of particles from the coating due to thermal shock. SEM observations of the arc traces formed on C-1133 electrodes revealed that the coating was spalled in the arced region due to the removal of individual particles and this left holes on the surface. Figure 6.7 is an SEM image of the arc trace on C-1133

coating after an erosion experiment. Arrows 1, 2 and 3 in figure 6.7 point to the regions of spalled coatings. Detailed observation of these regions indicated that the particles at these sites were dislodged and left behind a hole on the surface. This spalling of coatings was attributed to the thermal shocks produced during arcing. The spalling of coatings was observed only on the C-1133 coating which was formed by external injection. This indicates poor adhesion of the particles and is consistent with lower thermal conductivity values as shown in Table 6.3. Hence the weight loss for C-1133 coatings was both by erosion due to arcing and also by spalling of the coating.

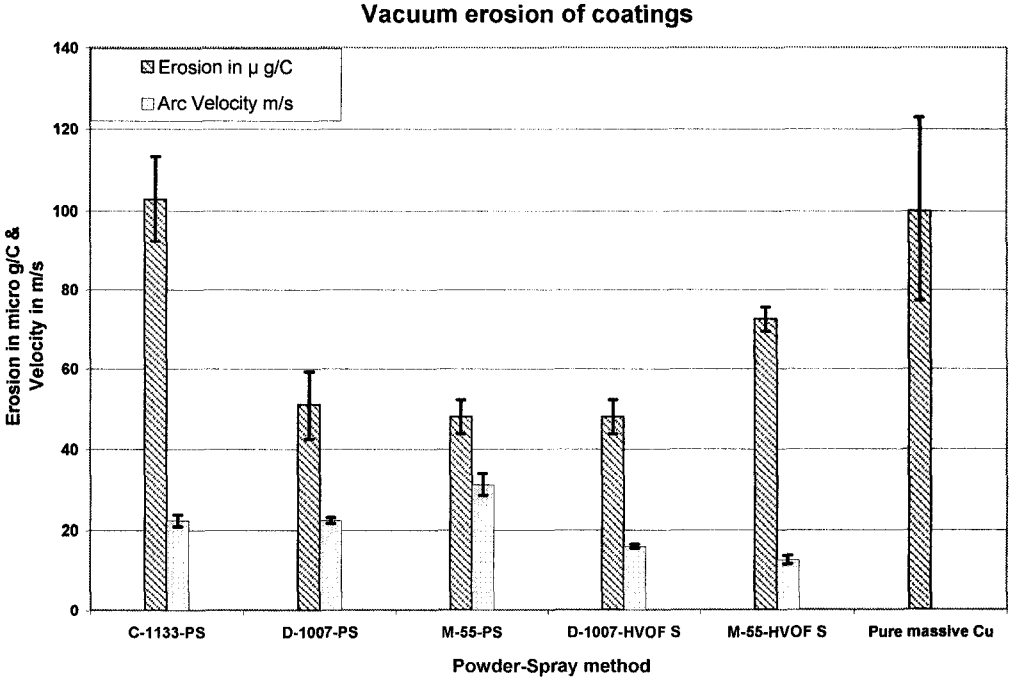

Figure 6.6 Erosion rate of coatings (PS: Plasma sprayed coatings and HVOF S: High velocity oxygen fuel sprayed coatings).

The arc velocity measured on D-1007 was 22.3 m/s and on M-55 it was 31.2 m/s, indicating that the arc moved more easily on M-55 than on D-1007 coatings. In spite of these differences in arc velocity the erosion values on both the coatings were similar with overlapping error bars.

Comparison of HVOF sprayed coatings: From figure 6.6, we see that, the arc velocity on D-1007 was 16.0 m/s whereas on M-55 it was 12.6 m/s, and the erosion rates on D-1007 and M-55 were 48 μg/C and 72 μg/C respectively. For these coatings increased velocity was correlated with reduced erosion rates.

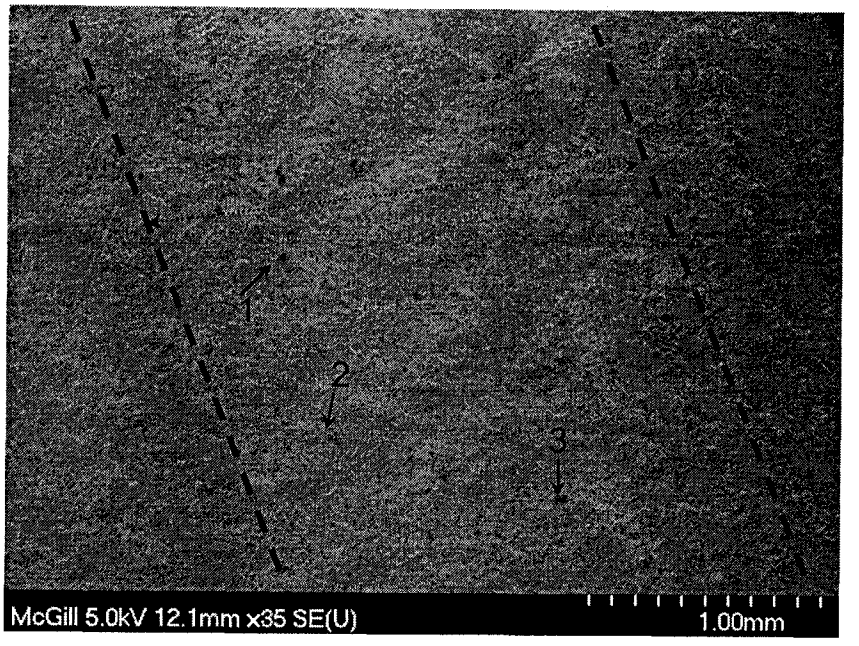

Figure 6.7 Arc trace formed on C-1133, the region showed between dashed lines was the arc trace; arrows 1, 2 and 3 show the holes formed on the coated electrode in the arced region due to dislodging of the coated splats.

Effect of arc velocity on erosion rate: It is well understood and reported in the literature that, increased arc velocities result in lower erosion rates. The arc velocities measured in our case were based on the arc trace length of the first arc only, whereas the erosion value was based on 135 arc pulses. Multiple arcing under vacuum conditions would remove the native oxide layer and also form overlapping arc craters. These changes in the surface chemistry and the surface roughness during multiple arcing, could lead to changes in the arc velocity as arcing proceeded. The arc velocity measured using the length of the first arc trace might thus not be valid for all the arcs. This could explain the apparently contradicting erosion rate-arc velocity results of plasma sprayed and HVOF coatings.

Effect of thermal conductivity on erosion rate: Erosion is a heat transfer problem and is expected to increase with poor heat removal from the electrode surface. One would expect that coatings with lower thermal conductivity such as PS coatings would yield higher erosion rates than HVOF coatings having higher thermal conductivity values. However, the erosion rates of both HVOF and PS coatings were similar for the D-1007 coatings though a slightly higher value was seen for HVOF sprayed M-55 coating. This observation leads us to conclude that, in our case the difference in thermal conductivity of the coatings was not influencing the erosion rate. This is because the experiments were transient and a time delay of 15-20 s between individual pulses was sufficient for uniform heat dissipation in the cathode.

Effect of microstructure and oxide content on erosion rate: All the five coatings had nanostructured grains and an oxide content of ~2 at%. All coatings except C-1133-PS, showed lower erosion values than pure massive Cu. Three of them (D-1007-PS, M-55-PS and D-1007-HVOF) showed erosion rates 50% lower than pure massive Cu. In spite of having the finest microstructure, the C-1133 coatings had the highest erosion rate due to spalling. The oxide content was common for all the coatings and hence the individual effect of oxide content and/or microstructure is a subject for further study.

The orientation of the microstructure appeared to have no effect; PS coatings had aligned columnar grains which were oriented perpendicular to the lamellar direction as shown in figure 6.4. On the other hand, HVOF coatings had grains oriented in all directions and there was no particular order/direction of orientation as shown in figure 6.5. In spite of this difference in grain orientation, the erosion values for the both cases were similar.

6.3.4 Characterization of eroded coatings

Figures 6.8a and 6.8b shows an optical microscope image of the arc trace and a SEM image of an individual crater formed on massive Cu. Individual arc craters which were well isolated from one another can be seen in figure 6.8a. Figure 6.8b is a higher magnification image of an isolated crater, which shows overlapping micro craters inside

an individual crater. The arc trace appeared discontinuous to naked eye observation. These findings are consistent with the findings from Daalder [8].

A macroscopic observation of a single arc trace on the coated electrodes appeared continuous as shown in figure 6.8c. Figure 6.8d shows the arc traces formed on a coated cathode after 135 arc pulses. The final arc trace on figure 6.8d appears longer than the first arc trace in figure 6.8c, because the cathode had to be moved vertically to ignite multiple arcs. A microscopic observation of the final arc trace also showed overlapping craters. For all the coated electrodes, these craters were smaller than those formed on massive Cu. This is further discussed below.

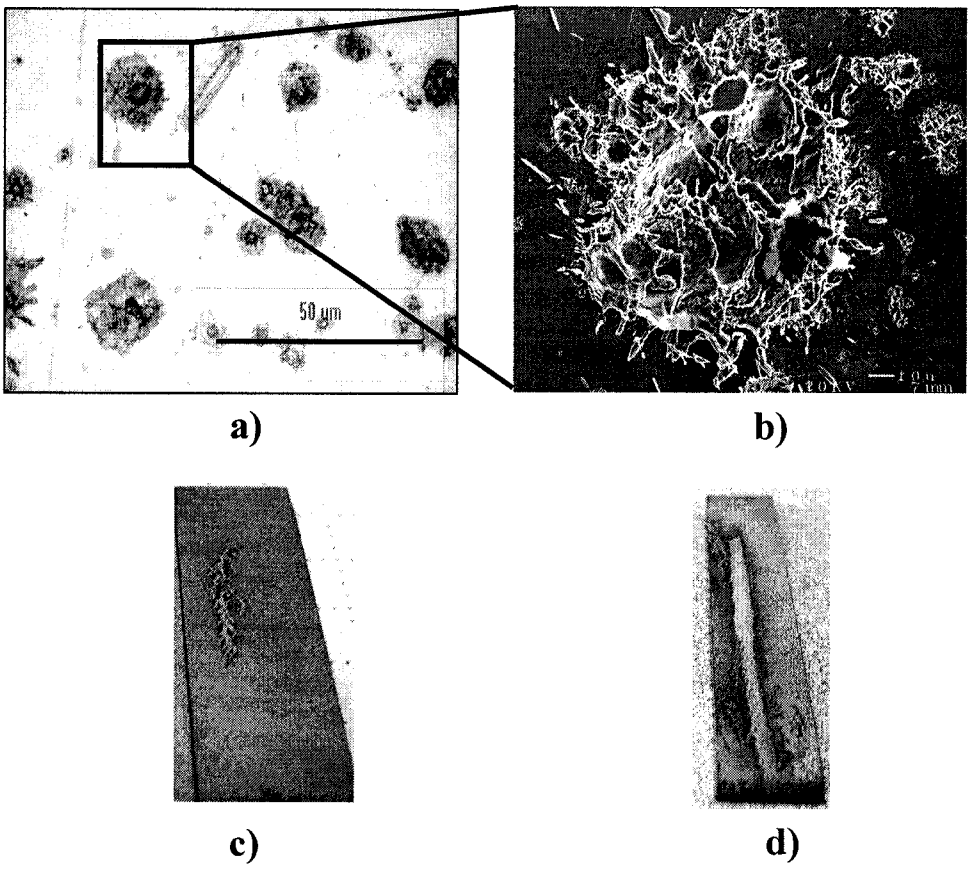

Figure 6.8 a) Optical microscope image of arc trace on a pure massive Cu; b) SEM image of the individual arc crater on a pure massive Cu showing overlapping craters c) typical arc trace formed on a coated coupon (width =12 mm) after a single arc of 500 µs long; d) arc trace formed after 135 arc pulses each of 500 µs long.

Figure 6.9 shows SEM images of the arc trace and arc craters formed on D-1007 coated electrode after 135 arc pulses. The total erosion constituted only a small fraction of the coating thickness. The brighter region seen between the dashed lines in figure 6.9a, which is an SE+BSE image, is the arc trace. Daalder [25], reported that, for pure Cu, a single arc discharge of I=127 A, divided into two discharges after a few mm of travel. He also reported that, the most probable crater diameter on these traces was between 7 μm and 12 μm with a narrow distribution. As seen in figure 6.9b and c, the craters formed on D-1007 had very small diameters with diameters of about 1-2 μm. Craters formed on other coatings were also similar in size. The formation of smaller crater sizes is consistent with lower erosion values.

Etched cross sections of the eroded coatings did not show any change in the microstructure of the coatings. The nano metric grain size distribution found in the initial coatings were retained on the arced regions of the coating.

6.4 Conclusions

The coatings produced by PS and HVOF spray methods had nano structured grain distribution. The individual particles used to make the coatings were completely melted and were surface oxidized during their flight. The oxygen content of the coatings was of the order of 2 at%. Though different powders were used in two different spraying techniques, the final coatings produced had similar grain size distribution. The grain size formed in the coatings ranged from 100 nm to 300 nm in width. These coatings when used as cathodes for vacuum arcs show lower erosion rates than pure massive Cu. The erosion rates on some of these electrodes were 50% lower than that of pure massive Cu reported under identical conditions.

Even after passing as many as 135 arc pulses, each 500 μs long, the nanostructure of the coatings remained intact. The craters formed on the coated electrodes were significantly smaller than those formed on pure massive Cu. This is consistent with the lower erosion rates.

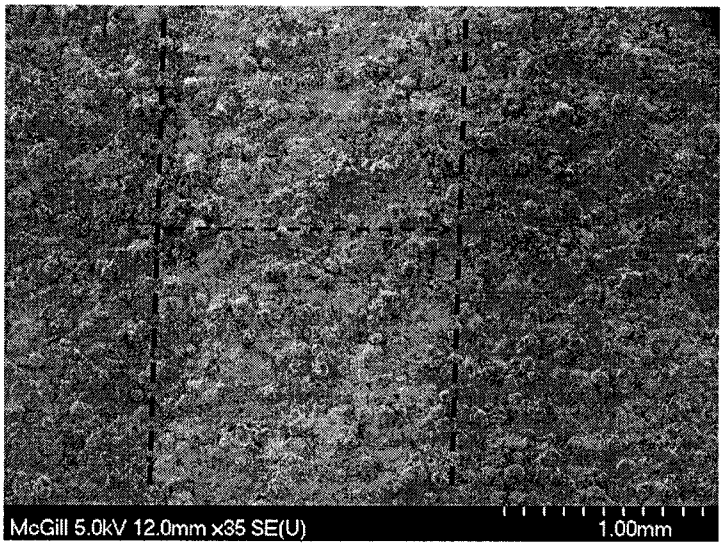

a)

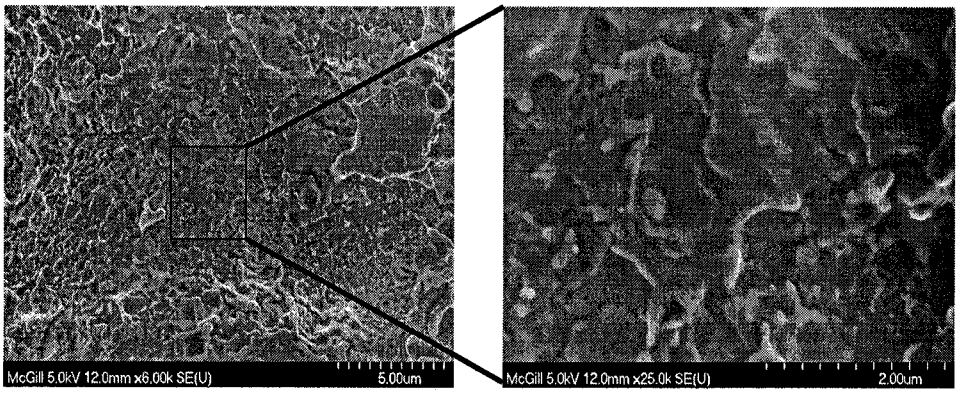

b) c)

Figure 6.9 a) Arc trace formed on D-1007 coating; the region showed between dashed lines was the arc trace; b) and c) show the arc craters formed.

The reasons for lower erosion rates may be nanostructure of the coatings or the presence of oxide layer on individual lamellas or a combination of both. Further experiments are in progress to isolate the effect of microstructure alone. Cold spraying of these powders is being pursued as an alternative way of forming the coatings free from oxide content.

6.5 Acknowledgements

The authors express their gratitude to Dr. Christian Moreau and Dr. Jean-Gabriel Legoux of IMI, Montreal, Canada, for producing the coatings, their valuable suggestions and discussions. The financial support of the Natural Sciences and Engineering Research Council of Canada for the work is gratefully acknowledged.

6.6 References

1. Boxman R L Twenty-five years of progress in vacuum arc research and utilization 1997 *IEEE transactions of plasma science,* **25** 6 1174-1186
2. Beilis I I 2001 State of the theory of vacuum arcs *IEEE transactions of plasma science* **29** 5 657-670.
3. Farrall G A 1980 Electrical breakdown in vacuum. Arcs: Theory and Application ed J M Lafferty (New York: Wiley)
4. Boxman L R, Sanders D M and Martin P J 1995 Handbook of vacuum arc science and technology: fundamentals and applications (New Jersey: Noyes publications)
5. Meunier J-L and Drouet M G 1987 Experimental study of the effect of gas pressure on arc cathode erosion and redeposition in He, Ar and SF_6 from vacuum to atmospheric pressure *IEEE transaction of plasma science* **PS-15** 5 515-519
6. Kimblin C W 1973 Erosion and ionization in the cathode spot regions of vacuum arcs *Journal of applied physics* **44** 7 3074-3078
7. Guile A E and Hitchcock A H 1978 The erosion of copper cathodes from vacuum to atmospheric pressure arcs *Journal of applied physics* **49** 7 4275-4276
8. Daalder J E 1978 Cathode erosion of metal vapour arcs in vacuum PhD thesis submitted to Eindhoven University of Technology Netherlands
9. Fu Y H and Smeets R P P 1989 The influence of contact surface microstructure on vacuum arc stability and voltage *IEEE Transactions on plasma science* **17** 5 727-729
10. Schmoll R 1998 Analysis of the interaction of cathode micro protrusions with low-temperature plasmas *J. Phys. D: Appl. Phys.* **31** 1841-1851
11. Farrall G A 1985 Electrical breakdown in vacuum *IEEE Transaction on electrical insulation* **20** 815-841

12. Juttner B, Pursch H and Shilo V A 1984 The influence of surface roughness and surface temperature on arc spots movement in vacuum *J. Phys. D: Appl. Phys* **17** L31-L34.
13. Daalder J E and Vos C W M 1972 Distribution functions of the spot diameter for single and multi cathode discharges in vacuum Eindhoven University of Technology Eindhoven Netherlands Rep 72-E-32
14. Ding B, Yang Z and Wang X 1996 Influence of microstructure on dielectric strength of CuCr contact materials in vacuum *IEEE Transactions on Components, Packaging and Manufacturing Technology Part-A* **19** 1 76-81
15. Wang Y P and Ding B J 1999 The preparation and their properties of microcrystalline and nanocrystalline CuCr contact materials *IEEE Transactions. CPT* **22** 467–72
16. Wang Y, Zhang C, Zhang H, Ding B and Lu K 2003 Effect of the microstructure of electrode materials on arc cathode spot dynamics *J. Phys. D: Appl. Phys* **36** 2649-2654
17. Zhang C, Yang Z, Wang Y and Ding B 2003 Cathode spot propagation on the surface of amorphous, nanocrystalline and crystalline $Cu_{60}Zr_{28}Ti_{12}$ cathodes *Physics Letters A* **318** 435–439
18. Houlbert A S, Cielo P, Moreau C and Lamontange M 1994 Measurement of thermal diffusivity and anisotropy of plasma sprayed coatings *International Journal of Thermophysics* **15** 3 525-546
19. Chang-Jiu Li and Bo Sun 2004 Microstructure and property of micro-plasma-sprayed Cu coating *Materials Science and Engineering A* **379** 92–101
20. McDonald A, Mario Lamontagne, Sanjeev Chandra, and Christian Moreau 2006 Photographing Impact of Plasma-Sprayed Particles on Metal Substrates *Journal of Thermal Spray Technology* **15** 4 708-716
21. Dent A H, Horlock A J, McCartney D G and Harris S J 2001 Microstructural characterization of a Ni-Cr-B-C based alloy coating produced by high velocity oxy-fuel thermal spraying *Surface and Coatings Technology* **39** 244-250

22. Edris H and Mccartney D G 1997 Microstructural characterization of high velocity oxy-fuel sprayed coatings of Inconel 625 *Journal Of Materials Science* **32** 863-872

23. Plyutto A A, Ryzhkov V N and Kapin A T 1965 High speed plasma streams in vacuum arcs *Soviet physics-JET* **20** 2 328-337

24. Kimblin C W 1974 Cathode spot erosion and ionization phenomena in the transition from vacuum to atmospheric pressure arc *Journal of applied physics* **45** 12 5235-5244

25. Daalder J E 1975 Erosion and the origin of charged and neutral species in vacuum arcs *J. Phys. D: Appl. Phys* **8**, 1647-1659.

Chapter 7 Effect of cathode microstructure on arc velocity and erosion rate of cold cathodes in magnetically rotated atmospheric pressure arcs

This chapter presents the effect of microstructure on erosion behavior of HVOF sprayed and vacuum plasma sprayed (VPS) Cu coatings in atmospheric pressure arc setup. The preparation and characterization of coatings are presented. Erosion rates of massive Cu in central cathode geometry are presented. The non effect of initial surface roughness on erosion rates is presented. The effect of annealing on microstructural properties, porosity and erosion behavior of the prepared coatings having grains ranging from a few hundred nanometers to a few micrometers are presented. The effect of initial coating thickness on erosion rates is presented. Erosion results in both inert and oxidizing gas atmosphere are presented.

Coated cathodes having smaller grains (0.9 to 3 μm) showed higher arc velocities and lower erosion rates compared to massive Cu cathodes with relatively large grain sizes (20 to 23 μm). Due to poor thermal transport properties, as-sprayed HVOF coatings severely spalled and resulted in higher erosion rates. However, annealing improved the thermal transport properties of the coatings, which reduced spalling and erosion rates. The VPS coatings which were free from intersplat oxide content isolated the effect of microstructure alone and confirmed that having smaller grains give higher velocities and lower erosion rates. Results prove a clear effect of microstructure on the erosion behavior of copper cathodes.

Abstract

Atmospheric pressure arc velocity and arc erosion measurements were performed on thermal sprayed copper cathodes having grain size distributions from submicron to a few microns in a continuous running arc system. Ultra high purity (UHP), 99.99% pure, argon and a mixture of UHP argon with 10% (v/v) extra dry air were used as plasma forming gases. An external magnetic field of 0.10 T was used to rotate the arc which was operated

at a constant power setting of 6 kW (150 A and 40 V). Cathodes having different microstructure were formed using high-velocity oxygen fuel (HVOF) spraying, vacuum plasma spraying (VPS) and annealing methods. HVOF sprayed cathodes were tested for arc erosion and arc velocity in their as-sprayed state and also after annealing them at 300 and 600 ^{0}C for 1 and 8 hr durations in an inert argon atmosphere. VPS sprayed coatings were tested as-sprayed. The effect of initial coating thickness on erosion rates was investigated. Annealing HVOF coatings at 600 ^{0}C for 8 hrs, produced near equi-axed grains 2 to 3 μm average size. These coatings gave 60% higher steady state arc velocities and up to 68% lower erosion rates compared to massive copper cathodes having 20 to 23 μm average grain size. VPS coatings having 0.9 to 1.5 μm average grain size gave up to 70% lower erosion rates when compared to massive copper cathodes. The results show a clear effect of cathode microstructure on arc velocity and on arc erosion rates.

7.1 Introduction

Cathode erosion still limits the application of plasma technology to processes which rely on torches with cold cathode in tubular geometry. Cathode erosion increases the operating cost of these processes via the cost of replacement cathodes, the cost of process down time to electrode replacement, and also by contaminating the process stream with erosion products.

Cathode erosion is a highly complex phenomenon which depends not only on arc residence time and heat removal from the cathode but, also on many other parameters [1]. Previous studies have shown that many factors such as the external magnetic field (B field) used to rotate the arc [2], the plasma gas, its chemistry and its flow rate [3-5], the electrode chemistry [6], the inter-electrode gap [7] and the operating conditions of the plasma torch such as the cooling water flow rate, the operating current and voltage [8-10] affect erosion rates. Specifically for Cu cathodes, the presence of O in the cathode and/or the presence of a certain amount of an oxidizing gas are known to reduce cathode erosion significantly [1, 6]. In addition to the above mentioned factors, cathode microstructure is also known to affect arc erosion rates [11-13]. Researchers have shown that the surface properties such as surface micro-protrusions, roughness, impurity inclusions and

microstructure of the cathode (grain size, second phase or particles, features like solute concentration and defect structure) significantly affect the break-down voltage and dielectric strength [14-19]. Wang et al., [20-22] working with nanostructured CuCr alloy cathodes and $Cu_{60}Zr_{28}Ti_{12}$ cathodes, observed that the erosion rates on these electrodes were lower compared to conventional cathodes (4%-20% less than massive Cu). They reported that the arc attachment points on nanostructured cathodes moved significantly faster and covered most of the cathode surface.

Cathodes having different microstructures with their grains ranging from hundreds of nm to a few μm can be produced by thermal spray techniques in combination with heat treatment methods. Specifically, high velocity oxygen fuel (HVOF) technique can give Cu cathodes having a nanostructured grain distribution [13]. Spraying Cu powder on Cu substrates using the HVOF technique can give 98% dense coated cathodes. These coatings generally have lower thermal conductivity than pure Cu [13, 23 and 24]. Since arc erosion of cathodes is chiefly a heat transfer problem, having a porous coating of lower thermal conductivity will not help reduce erosion rates. However, annealing HVOF sprayed coatings is known to improve the thermal conductivity, electrical conductivity and adhesion strength of the coatings [23]. Hence, annealed HVOF coatings may give reduced erosion rates.

In addition to having nanostructured grain distribution, HVOF coated Cu cathodes have intersplat oxygen contents of ~2 at%. In our earlier studies, using HVOF coatings as vacuum arc cathodes, we have shown that these coated cathodes give 50% lower erosion rates than massive Cu (further referred as M-Cu) [13]. The reduced erosion rates may have been due to the nanostructured grains or due to the presence of intersplat oxygen or a combination effect. Thus HVOF coatings cannot isolate the effect of microstructure alone on the erosion rate and studying the effect of microstructure alone is of fundamental interest. Vacuum plasma spray coatings (VPS) can also produce nanostructured coatings but with zero or very minimal oxygen content and hence can isolate the effect of microstructure from the effect of oxygen content.

The main objective of this work was to study the effect of microstructure alone on the erosion behavior of copper cathodes. Also the work aims at identifying a better cathode having low erosion rates. In this paper, we present on arc velocity and arc erosion studies of annealed and as-sprayed HVOF coatings which have nanostructured grain distribution and intersplat oxygen

content. Annealing time, temperature and initial thickness of the coating were studied as parameters affecting erosion rates of HVOF coatings. VPS coatings which have only nanostructured grain sizes but zero or minimal oxygen content were studied to isolate the effect of microstructure. For VPS coatings, only the coating initial thickness was studied as a parameter. Erosion studies were conducted both in an inert atmosphere and in oxidizing atmosphere. The details are presented below.

7.2 Materials and experimental methods

Commercially available Cu powder viz., Metco-55 (99.99% pure; further referred as M-55), was used as spray powder. The morphology and size distribution of M-55 was determined by scanning electron microscopy (SEM) and Mastersizer-2000 respectively. Distilled water was used as dispersant in the Mastersizer for size distribution analysis. Energy dispersive spectroscopy (EDS) and inductively coupled plasma mass spectroscopy (ICP) techniques were used to determine the chemical composition of M-55.

M-55 was sprayed using HVOF and VPS methods. The spray conditions used are summarized in table 7.1. During HVOF spraying, the substrate was cooled by jets of cold nitrogen and the temperature of the substrate was monitored not to exceed 200 ^{0}C, using a pyrometer. Three different substrates viz., square copper plates (60mm × 60mm × 2.5mm), square aluminum plates (35mm × 35mm × 3mm) and hollow copper cylinders (25 mm outer diameter, 65 mm length) were used for HVOF spraying. Only solid copper rods (25 mm outer diameter, 305 mm length) were used as substrates for VPS. All the substrates were grit blasted with 800 μm alumina grits, just before coating and had a surface roughness Ra of 8.58 μm. For erosion studies, coatings having three different thickness ranges viz., 100-150 μm, 350-400 μm and 800-850 μm were produced with both the HVOF and VPS methods.

The coated copper plates were further cut and used as specimens for microscopic analysis. The coatings formed on aluminum substrates were separated from the substrate by dissolving the aluminum in 40% KOH solution, to obtain free-standing specimens for

thermal diffusivity measurements by the laser flash method as explained in [25]. Thermal diffusivity values were converted to thermal conductivity by considering the properties of pure Cu (ρ = 8900 kg/m^3, Cp = 386 J/kg K, k = 398 W/m K).

VPS coated solid copper rods were cut and machined into hollow cylinders (65 mm length, 25 mm outer diameter and 3 mm wall thickness), to use as cathodes for arc erosion and arc velocity measurements. Great care was taken to avoid any contamination of the coatings during machining. EDS analysis of the machined cathodes revealed only O and Cu peaks. The oxygen peak was attributed to the surface oxidation of Cu. No other high molecular weight elements were detected in the EDS analysis. This confirmed that no high molecular weight metal contaminants were added to the VPS coating during machine and the coating was essentially pure Cu.

The HVOF coated hollow cylinders and copper plates were annealed in an argon atmosphere in a tubular furnace. A full factorial two temperature (viz., 300 ^{0}C and 600 ^{0}C), two annealing times (viz., 1 hr and 8 hrs) experimental design was chosen for annealing. Before starting the annealing procedure, the specimens were placed inside the tubular furnace and the furnace was flushed with ~90 furnace volumes of 99.99% pure argon gas flowing at 3 slpm. After purging, the heating was started maintaining the argon flow rate to reach the desired annealing temperature. It took less than 10 minutes to reach the desired annealing temperature. The specimens were held at this temperature for either 1 hr or 8 hrs. Then the heating was stopped and the specimens were allowed to cool down to room temperature inside the furnace, while still maintaining the argon flow. Annealed hollow cylinders were used as cathodes for erosion studies whereas Cu plates were used for microscopic analysis.

For microscopic analysis, the coatings on Cu substrates (i.e., copper plates in the case of HVOF coatings and copper rods in the case of VPS coatings) were cut using a Struers 'Secotom-10' universal precision cut off machine and vacuum mounted in cold setting resin. The mounted specimens were wet ground using SiC paper #800, 1200 and 4000 under running tap water. The ground samples were the polished using 3 μm and 0.04 μm

silica suspensions. The polished samples were etched with a $FeCl_3$ etchant (2.5 g of $FeCl_3$ + 10 ml of HCl + 50 ml of ethanol) for 5 seconds. The etched coatings were examined under optical microscope and SEM to determine their microstructure. To determine the porosity of the coatings, as many as 10 SEM pictures of polished coatings (prior to etching) were taken at regular intervals on each of the coatings and the porosity of individual pictures was measured by an image analysis technique. An average of these numbers were calculated and reported as porosity with a standard deviation of ± 5%.

Table 7.1 Spray conditions.

Parameters	HVOF spraying	Vacuum plasma spraying
Spray distance	14 inches (355.6 mm)	11.8 inches (300 mm)
Transverse speed	30 inches per sec (0.76 m/s)	
System settings	Kerosene (K) : 0.28 lpm Oxygen (O_2) : 967 lpm Stochiometry O_2: K: 5.64:1 (wt %) Combustion pressure: 58.05 kPa	Arc current (I) :700 A Primary gas : Ar: 40 lpm Secondary gas: H_2: 5 lpm Operating pressure: 100 bar

The externally coated hollow copper cylinders were used as cathodes in a continuous arc chamber. The schematic diagram of the experimental setup used for this study is shown in figure 7.1; details are presented elsewhere [3]. Figure 7.1a shows the setup which uses a concentric electrode geometry whereby the water-cooled cathode is on the centerline while the water-cooled sleeve anode surrounds it, thus defining a minimum annular gap of 4 mm. Figure 7.1b shows the dimensions of the electrode assembly. A water-cooled solenoid which surrounds the electrode assembly was used to apply an axial magnetic field B of 0.10 T, to rotate the arc. The axial magnetic field strengths varied less than 3% radially and 5% axially within the test cathode. The arc was ignited by a high-frequency trigger pulse and powered by a welding power supply (maximum power and current of

78 kW and 500 A, respectively). An average power of 6 kW (40 V and 150 A) was maintained throughout the experiments. Experiments were conducted either using ultrahigh purity (UHP; 99.99% pure) argon or a mixture of UHP argon with 10% (v/v) extra dry air (moisture < 2 ppm) as plasma forming gas, which circulated from the lower end of the reactor to the top end at a flow rate of 23 SLPM under atmospheric pressure.

The coated hollow cylinders, which had a surface roughness Ra of 18 μm, were used as-sprayed without giving any special surface finish or polishing. The cathode was weighed (accuracy ± 5×10^{-4} grams) and was installed in the reactor. The cathode was eroded at a constant power setting for a fixed time anywhere between two to ten minutes depending on the planned length of the experiment. An optical detector as shown in figure 7.1a was used to capture the arc rotation frequency. The optical detector consisted of a photodiode and a collimating lens assembly which had a narrow field of view of 3 mm. The optical detector assembly, fixed at the bottom of the rector, was aligned to view the arc between the electrodes and gave a positive voltage output when the arc passed in its narrow field of view. This optical voltage output along with the arc current and arc voltage waveforms were recorded simultaneously onto a computer using LabVIEW at 10 kHz sampling rate. After the experiment, the cathode was removed from the reactor and completely dried of cooling water before recording its final weight. The erosion rate values in grams per coulomb were calculated by dividing the weight difference of the cathode before and after the arcing, by the total electric charge $Q = \int I\,dt$ passing through the cathode. The arc rotational frequency was calculated from the recorded optical voltage data using windowed fast Fourier transform analysis. For each kind of coating, a minimum of two and a maximum of three individual experiments were performed and an average erosion rate was determined and reported here as the average erosion rate along with its standard deviation .

7.3 Results and discussion

7.3.1 Characterization of powders

Detailed characterization of M-55 is presented elsewhere [13]. The M-55 powders were mostly spheroids with a few irregular shaped particles. The size distribution of M-55

particles was log normal ranging between 28 to 110 μm with a maximum at 70 μm. The volume weighted mean size of M-55 particles was 102 μm. EDS and ICP analysis of the particles revealed them to be 99.99% pure copper particles with no detectable contaminants.

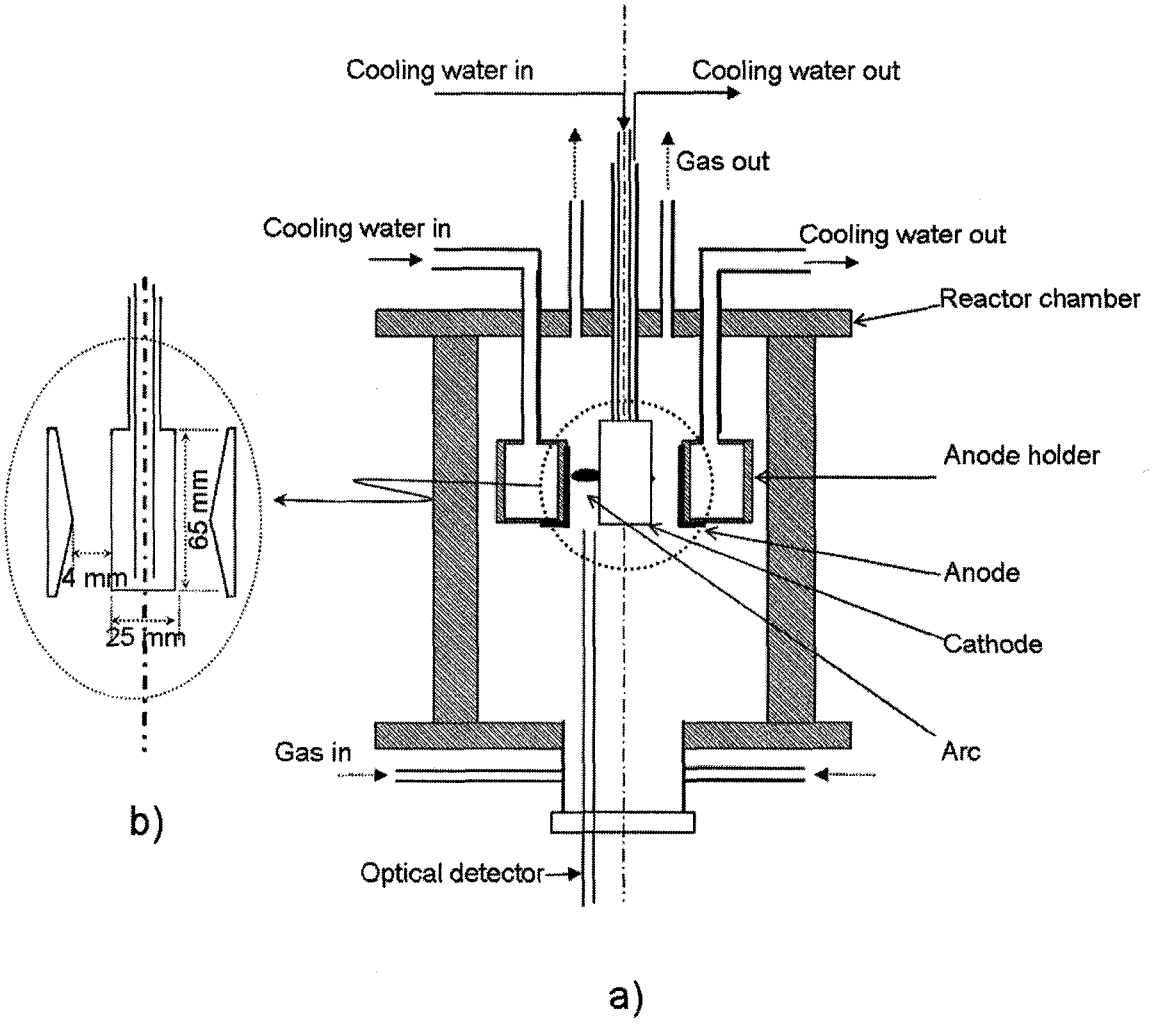

Figure 7.1 a) Schematic of the experimental setup; b) dimensions of the electrode.

7.3.2 Characterization of coatings before erosion

7.3.2.1 Characterization of as-sprayed HVOF coatings

Figure 7.2a shows an SEM picture of etched HVOF as-sprayed coating (further referred as H-as-sprayed). A detailed description of H-as-sprayed coating is given elsewhere [13].

As expected of HVOF coatings [26, 27], H-as-sprayed coating had nanostructured columnar grains with their width ranging from 100 to 300 nm. The coating was 98% dense and had a thermal conductivity k = 236 W/m K (k of M-Cu = 367 W/m K). In flight surface oxidation of the particles was evident from the dark intersplat regions seen in a back scattered electron (BSE) image of the coatings (not shown here). EDS analysis showed an oxygen content of 2.2 at%. The properties of as-sprayed HVOF coating are summarized in table 7.2.

7.3.2.2 Characterization of annealed HVOF coatings

Figures 7.2b and 7.2c, SEM pictures of HVOF coatings annealed at 300 ^{0}C for 1 and 8 hrs respectively (further referred to as H-300-1 and H-300-8 coatings respectively). We observe some grain growth relative to as-sprayed coatings shown in figure 7.2a. The well defined columnar grains, which were present in the as-sprayed coating, have started to grow in their width and to shrink in their length. The grains in these coatings were still columnar in shape with their widths still in the nanometer range varying between 500 and 700 nm. Figures 7.2c and 7.2d shows the SEM pictures of HVOF coatings annealed at 600 ^{0}C for 1 and 8 hrs respectively (further referred as H-600-1 and H-600-8 coatings respectively). Here we see a clear grain growth and microstructural changes. In both H-600-1 and H-600-8 coatings, the grains are no longer columnar. The well defined nanometric columnar grains which were present in the as-sprayed coatings have grown in their width and shrunk in their lengths yielding near equi-axed grains. The grains in H-600-1 coatings were similar to H-600-8 coatings. Table 7.2 summaries the grain size and shape of all the coatings. Our observations corroborate the findings of [23].

All the annealed HVOF coatings were also 98% dense. Attempts were made to determine the thermal diffusivity by the laser flash method as described in [25]. We were only able to measure the thermal diffusivity of the HVOF-as-sprayed coatings, which is presented in table 7.2 after converting into thermal conductivity values using M-Cu properties. For annealed coatings, the thermal diffusivity signal was 'saturating' i.e., the .signal reached its peak at a time scale which we were unable to resolve. This indicates a very high thermal conductivity.

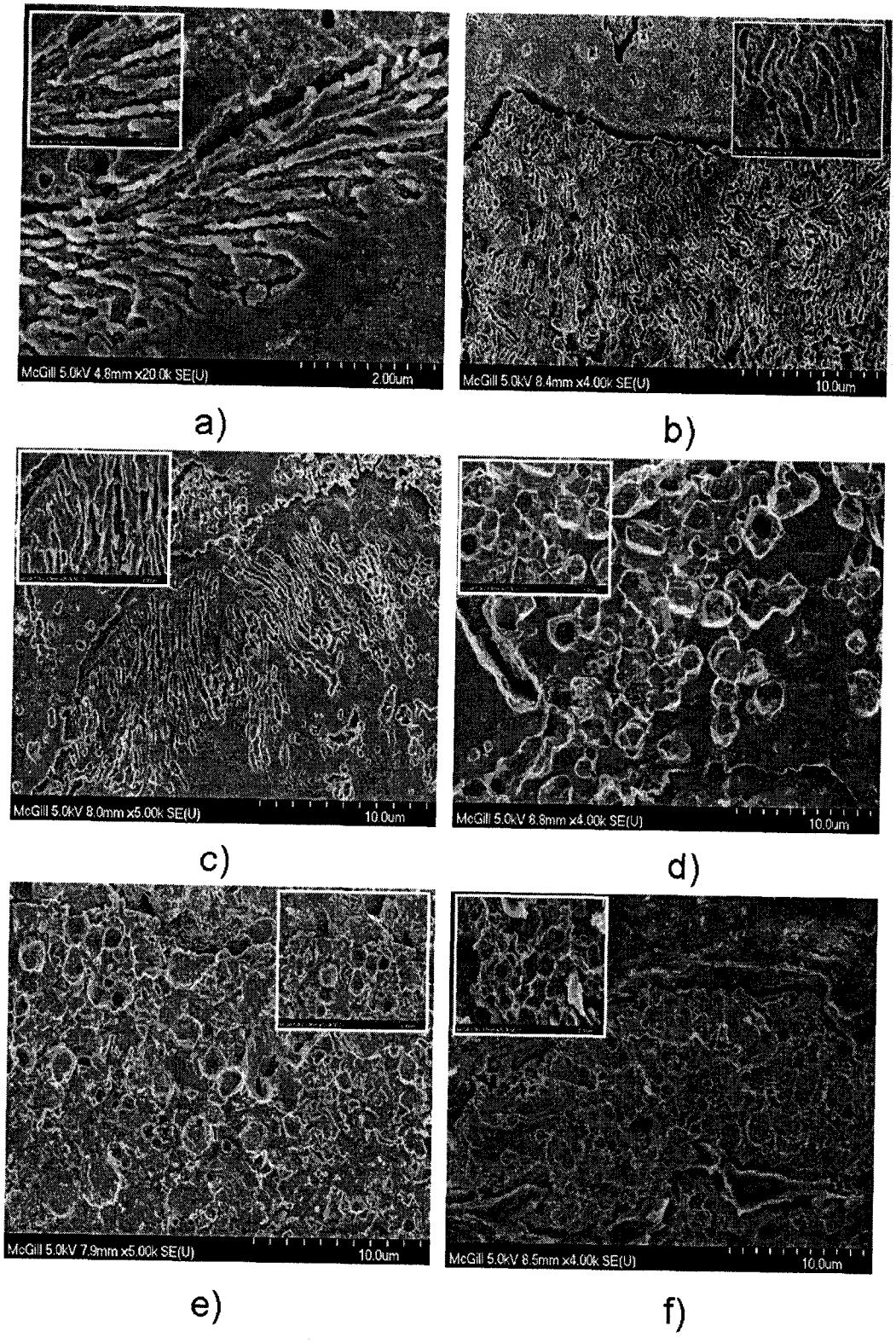

Figure 7.2 SEM pictures of the coating before erosion experiment. a) H-as-sprayed; b) H-300-1; c) H-300-8; d) H-600-1; e) H-600-8 and e) VPS coating.

Table 7.2 Properties of the coatings.

Coating	Grain size [μm]	Grain shape	Porosity [%]	Thermal conductivity [W/mK]
H-as-sprayed	0.1 to 0.3	Well defined columnar	2%	236
H-300-1	05 to 0.7	Columnar	2%	> 236
H-300-8	0.5 to 0.7	Columnar	2%	> 236
H-600-1	2.0 to 3	Near equi-axed	2%	> 236
H-600-8	2.0 to 3	Near equi-axed	2%	> 236
V-as-sprayed	0.9 to 1.5	Near equi-axed	<1%	-
Fully annealed M-Cu	20 to 23	Equi-axed	0%	367

7.3.2.3 Characterization of as-sprayed VPS coatings

Low magnification SEM images (not shown here), show that the VPS-as-sprayed coatings (further referred as V-as-sprayed) were >99% dense. Heavy deformation of the particles from their initially shape was clearly evident. The coatings appeared as stacking of well flattened lamellae with nearly even thickness. A well deformed single splat of the V-as-sprayed coating is shown in figure 7.2f, which is an SEM picture after etching. The fine details seen in figure 7.2f are the grain boundaries. Comparing figure 7.2e and 7.2f, we conclude that the grain shapes of the V-as-sprayed coatings appear recrystallised similar to H-600-8 coatings. The grain sizes of the V-as-sprayed coating ranged from 0.9 to 1.5 μm and the properties of the VPS coatings is summarized in table 7.2.

7.3.3 Arc velocity and erosion results

7.3.3.1 Arc velocity and erosion of central massive Cu cathodes in argon atmosphere

It was only possible to coat the outside of a hollow Cu cylinder. These coated hollow cylinders which were used as central cathodes had a surface roughness of 18.58 μm. Earlier arc erosion studies of Cu from our group [1] were for external cathode geometry and the cathodes used had machine finished surface roughness, Ra =0.06 μm. We have

shown that, in vacuum arcs, the surface roughness of the cathodes affects their erosion rates [28]. It would be expected that the erosion behavior of machine finished external cathode would be different from that of the central cathode reported here because, the cooling intensity for central cathode was different, the Cu used in this study had a slightly different composition, the geometry of the cathode-anode combination was different and also the surface roughness was different. Thus, it was important to carry out erosion experiments with the central cathode geometry using uncoated massive Cu cathodes (further referred as M-Cu). These results could be used as a base line to compare with the arc velocity and erosion rates of various coatings. Central M-Cu cathodes were eroded for two, four, six and eight minutes of arcing time and the arc velocity and overall arc erosion rates were measured. All but one of the cathodes had a normally machined surface with a roughness Ra of 0.06 μm. One test cathode was grit blasted with 708 μm alumina grits and had a roughness Ra of 8.58 μm.

Typical average arc velocities on central M-Cu, for different arcing times is shown in figure 7.3. We see that for all cases arc velocity has two regimes, a first regime in which the arc velocity is high (starts at 50 m/s and is reducing) for the first 120 to 180 s of the experiment followed by a second regime in which the arc velocity is low (6.6 ± 0.6 m/s) for the rest of the experiment. The initial fast velocity regime is due to the presence of a thin layer of native oxide on the cathode which reduces its work function and allows higher arc rotational velocities [6]. This thin native oxide layer is completely eroded in the first 120 to 180 s of the experiment, leaving behind a pure Cu surface for further erosion.

Figure 7.3 also shows the effect of cathode surface roughness on the arc velocity on a central cathode for a four minute experiment. A comparison of the arc velocity curves for four minute machine finished and four minute rougher cathode shows that the rougher cathode had higher initial arc velocities but that both cathodes reached approximately the same steady state velocity after 130 s.

One would expect that, the erosion rate, which is primarily a function of heat removal and arc residence time on the cathode, should be lower when the arc velocities are higher and vice versa. Figure 7.4 shows the overall erosion rates (E_o) of central M-Cu for different arcing times. We see from that the E_o values are low for both two and four minutes of arcing time and high for six and eight minutes of arcing time. These E_o results agree very well with the arc velocity argument presented above.

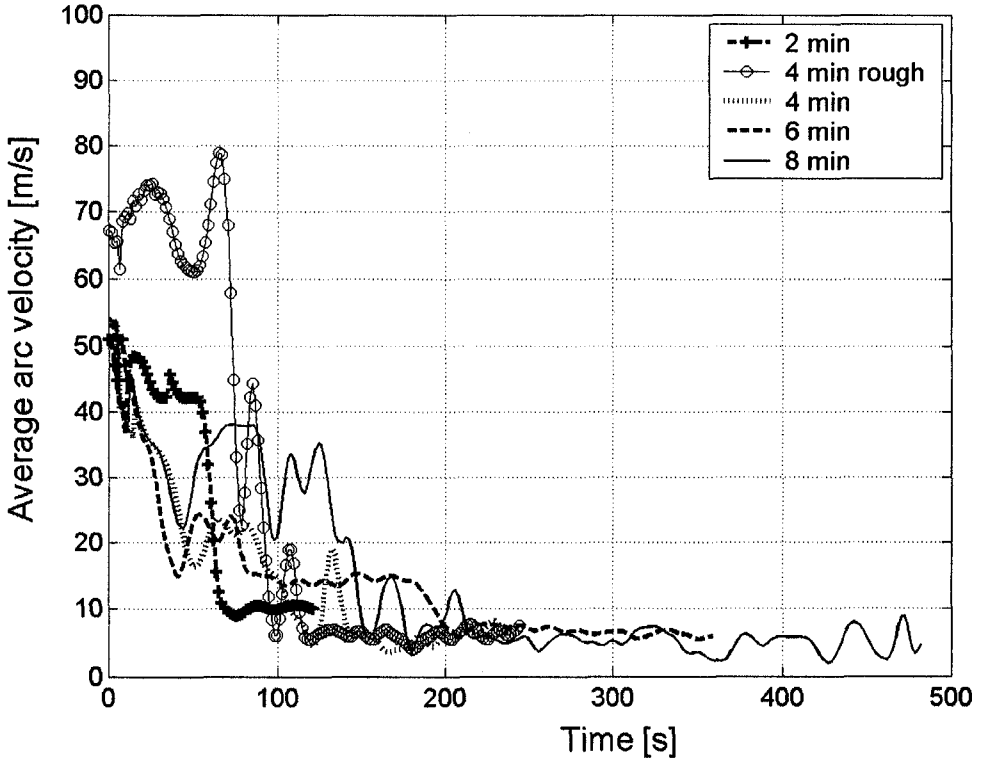

Figure 7.3 Arc rotational velocity of M-Cu for different arcing time. All cathodes except 4 min rough one had machine finished surfaces, Ra = 0.06 μm; 4 min rough cathode was grit blasted, Ra = 8.58 μm.

Figure 7.4 also shows the E_o values of machine finished M-Cu and grit blasted M-Cu. The E_o values for both the cathodes were similar and hence it was concluded that the arc erosion rates was independent of the initial surface roughness of the cathode.

The E_o reported in figure 7.4 was computed by dividing the overall weight loss of the cathode (Δm_o) by the total electric charge transferred ($Q_o = \int I\, dt$). That is,

$$E_o = \frac{\Delta m_o}{\int_0^{t_f} I\,dt} \qquad 7.1$$

Where, I is the arc current and t_f is the total arcing time. But, the Δm_o itself is a combination of two individual weight losses. One, a low weight loss (Δm_n) during the first 120 to 180 s of arcing, where the arc is running faster on a native oxide layer. Second a high weight loss (Δm_c) for the rest of the experiment, where the arc is running slower on a pure Cu surface. The arc velocity on native oxide layer is unsteady and is reducing with time whereas the arc velocity on pure Cu is steady with time. Mathematically,

$$\Delta m_0 = \Delta m_n + \Delta m_c \qquad 7.2$$

The true erosion rate of M-Cu (E_c) is the erosion of pure Cu occurring during the second steady regime where the arc is running on a pure Cu surface but not on a native oxide layer. To obtain E_c, mass of the native oxide lost (Δm_n), occurring during the first unsteady regime, needs to be subtracted from Δm_o reported in figure 7.4. So, rearranging equation 7.2 in terms of erosion rates and charge transfer we get

$$\Delta m_c = \Delta m_o - \Delta m_n \qquad 7.3$$

$$E_c \times \int_{t_n}^{t_f} I dt = E_o \times \int_0^{t_f} I dt - E_n \times \int_0^{t_n} I dt \qquad 7.4$$

Where t_n is the time for which the arc was running on native oxide layer. Knowing I from the recorded arc current data and t_n from the arc velocity results, E_c was computed according to equation 7.4 and was 47 ± 5 μg/C.

Researchers from our group working on external M-Cu have reported an erosion rate of 13.5 ± 1 μg/C [1], whereas we report here an erosion rate of 47 ± 5 μg/C. As mentioned earlier, the reasons for higher erosion rates reported here are: the cooling intensity of the cathode, the chemical composition of the copper used and the anode-cathode geometry. The earlier reports were for external cathode geometry and the cathode used was electrolytic tough pitch copper (99.9% pure) which had ppm levels of silver, iron and

oxygen contamination [29]. The external cathode (39 mm outer diameter) had 105% higher surface area for heat removal compared to the present case of central cathode. The cooling water flow rate for the external cathode was 5 lpm whereas the cooling water flow rate for the central cathode was 2 lpm. Hence the cooling intensity of the central cathode was lower than that of external cathode. It is also known that ppm levels of silver and oxygen contaminants present in the cathode reduces the work function of the cathode and gives higher arc velocities [6]. The cathode used in our case was 99.99% pure oxygen free high conductivity copper, with no detectable contaminants. Due to the combination of these factors, the erosion rates of central M-Cu cathodes were ~3.3 times higher than that of external M-Cu.

In conclusion, the average true erosion rate of central M-Cu cathodes in argon atmosphere was 47 ± 5 μg/C and was independent of initial surface roughness.

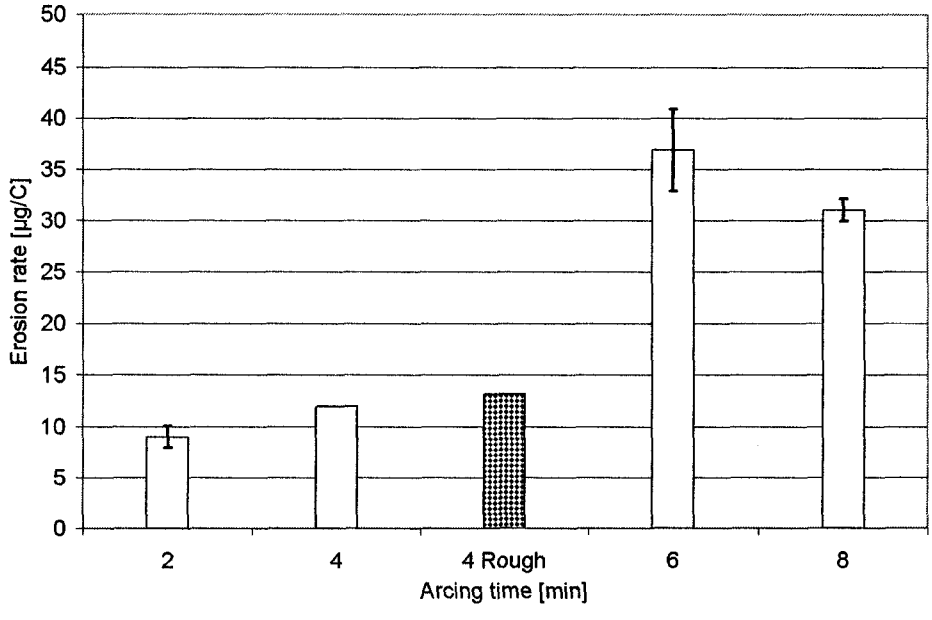

Figure 7.4 Overall erosion rate, Eo of M-Cu for different arcing time. All cathodes except 4 min rough one had machine finished surfaces, Ra = 0.06 μm; 4 min rough cathode was grit blasted, Ra = 8.58 μm. Notice that 4 min rough cathode had same Eo as that of 4 min machine finished.

7.3.3.2 Arc velocity and erosion of central M-Cu cathodes in an oxidizing atmosphere.

Erosion experiments of M-Cu were also performed in central cathode geometry using an oxidizing atmosphere. A mixture of UHP argon and 10% (v/v) extra dry air (< 2 ppm moisture) was used as the plasma forming gas. The purpose of these experiments was to find the effect of microstructure alone by making the oxidizing atmosphere common for both M-Cu and coated cathodes. The erosion of M-Cu cathodes in an oxidizing atmosphere will be used as a base line to compare with the erosion of a coated cathode also in an oxidizing atmosphere. For these experiments, the arc was started using UHP argon and then was switched to a mixture of UHP argon and air after 50 s of operation. The switching of gases took less than 20 s and the total length of the experiment was 6 minutes.

Before calculating the erosion values, the mass build on M-Cu due to oxidation in the presence of O was removed by using the dilute nitric acid treatment [1]. This weight gain was 2% of the total weight loss of the cathode.

Figure 7.5 shows typical arc velocities for M-Cu in an oxidizing atmosphere. The arc velocity on M-Cu started at 55 m/s and reduced in the 50 s while the plasma gas was UHP argon similar to arc velocities shown in figure 7.3. Between 50 and 70 s, the arc velocity increases to 60 m/s as the plasma gas becomes oxidizing. Beyond 70 s, the arc velocity for M-Cu remains high and steady at 60 m/s till the end of experiment. The high velocity seen for M-Cu in an oxidizing atmosphere is attributed to the copper oxide formed on the cathode.

Figure 7.6 shows the E_o values for M-Cu in an oxidizing atmosphere, which is 8.76 ± 0.61 μg/C. This E_o value is similar to the 2 min E_o value reported in figure 7.4 for M-Cu in UHP argon atmosphere (E_o = 8.99 ± 1.07 μg/C). These results clearly show that the presence of copper oxide, whether from the native oxide layer or an oxidizing atmosphere, causes high velocity and gives a low erosion rate.

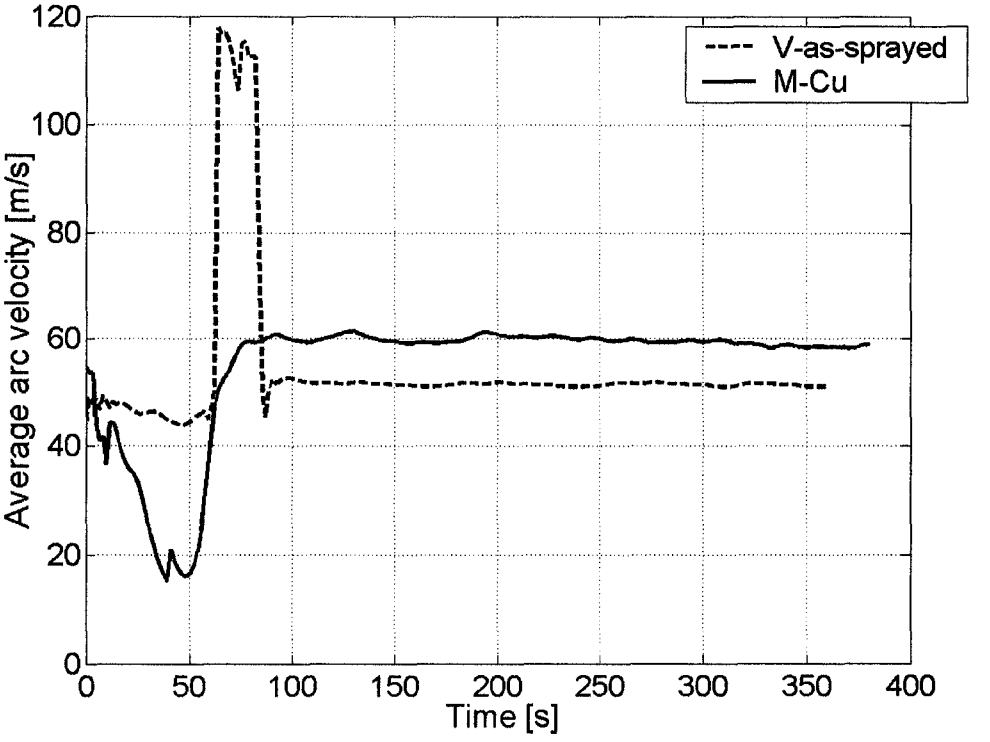

Figure 7.5 Arc velocities of M-Cu and V-as-sprayed cathode in an oxidizing atmosphere.

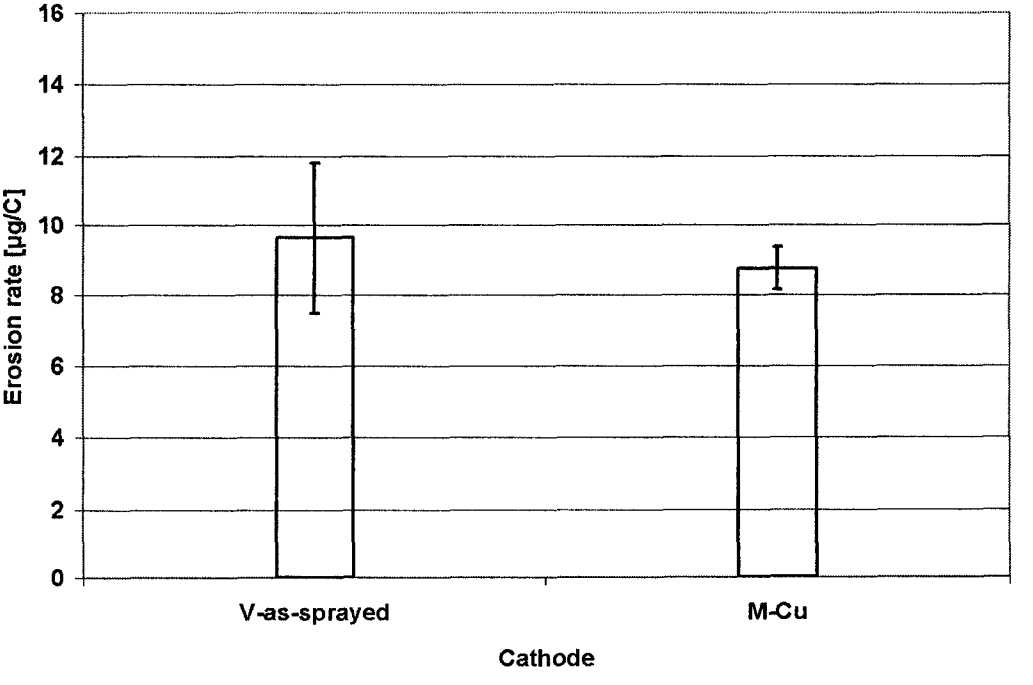

Figure 7.6 Overall erosion rate, Eo of M-Cu and V-as-sprayed cathode after six minutes of arcing time.

7.3.3.3 Arc velocity and erosion of H-as-sprayed coatings in argon

Figure 7.7 shows the typical arc velocity results for H-as-sprayed coating for a four minute arcing experiment. The arcing was stopped after four minutes due to the spalling of the coating. We see from figure 7.7 that, unlike M-Cu, the arc velocity on H-as-sprayed coatings has only one fast regime during first four minutes of arcing and the arc velocity oscillates between 35 and 20 m/s. H-as-sprayed coatings differ from M-Cu cathodes in two ways. The grain size of H-as-sprayed coatings is 100-300 nm whereas the grain size of M-Cu is 20-23 μm. In addition, H-as-sprayed coatings have an oxygen content of ~2 at% [13]. Whereas M-Cu is oxygen free. The high velocity observed on H-as-sprayed coating could have been due to nanostructured grains or the oxygen content or both. H-as-sprayed coatings cannot isolate the effect of grain size alone.

One would expect that the E_o values for H-as-sprayed coatings to be lower than M-Cu because of their higher arc velocities. Figure 7.8 shows the E_o values of H-as-sprayed cathodes after four minute arcing. From figure 7.8, we see that the E_o values of H-as-sprayed coatings were 39 ± 6 μg/C. These E_o values cannot be corrected for arcing on the oxide layer because, unlike M-Cu, the oxide layer for H-as-sprayed coatings is not present as a separate layer, but is present at all inter-splat boundaries throughout the coating. Figure 7.9 shows a picture of the H-as-sprayed cathode before and after an erosion experiment. Severe spalling of the cathode can be clearly seen in figure 7.9. High erosion rates seen on H-as-sprayed coatings were attributed to this high spalling of the coating.

The presence of inter-splat oxide layer at the boundaries of individual splats was believed to cause high spalling of H-as-sprayed cathodes. The inter-spat oxide has higher electrical resistivity than pure Cu [23]. We hypothesis that, when H-as-sprayed coatings were used as current carrying electrodes, the intersplat oxide layers cause local heating and hence reduce the coating adhesion strength leading to heavy spalling of the coating. Further efforts were made to improve the coating adhesive strength.

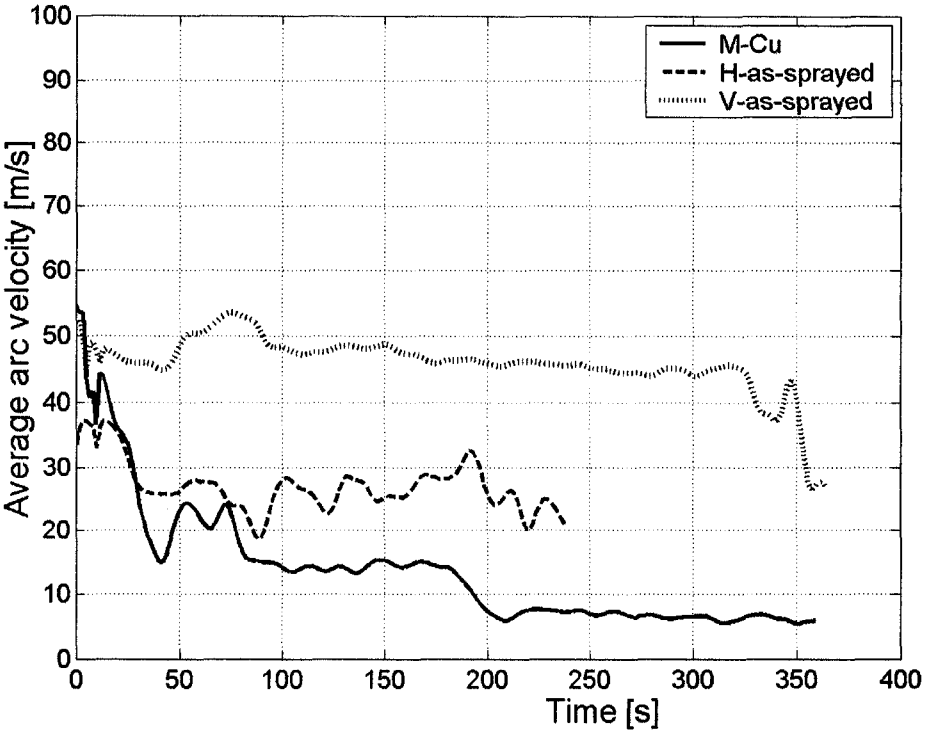

Figure 7.7 Arc rotational velocities of H-as-sprayed and V-as-sprayed coatings.

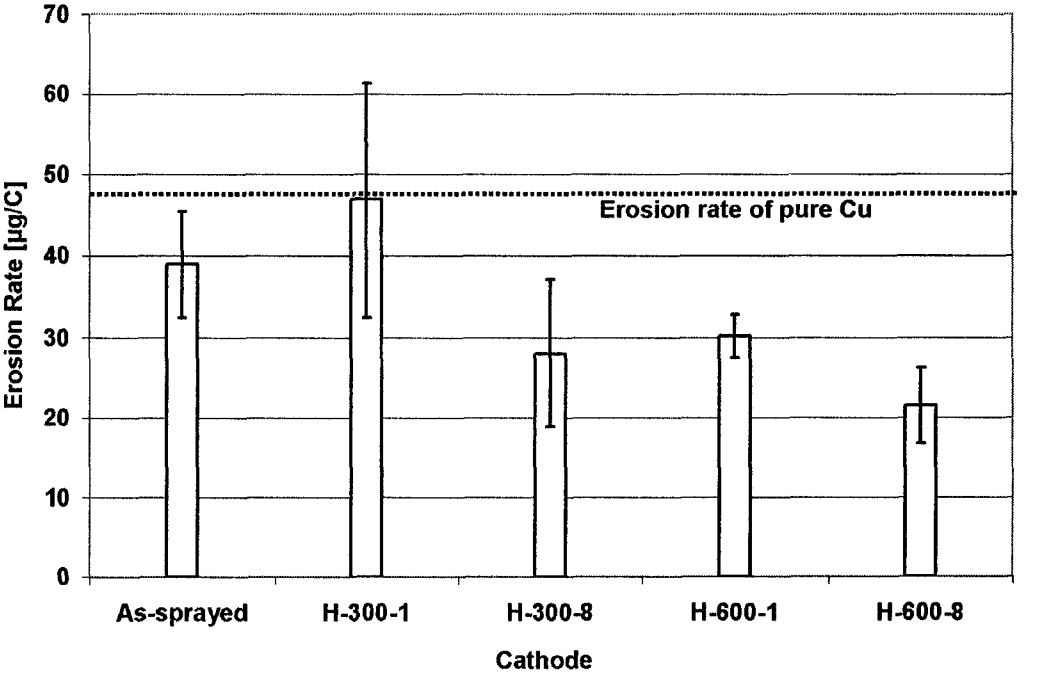

Figure 7.8 Overall erosion rate, Eo of H-as-sprayed and annealed HVOF cathodes.

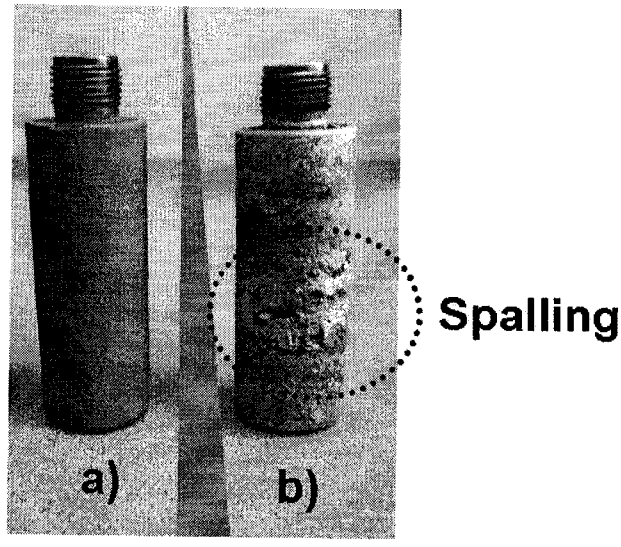

Figure 7.9 Pictures of HVOF cathodes a) before erosion; b) H-as-sprayed after erosion Notice heavy spalling of the cathode.

7.3.3.4 Arc velocity and erosion of annealed HVOF coatings in argon

Annealing of the HVOF coatings is known to improve their adhesive strength as well as their thermal and electrical transport properties [23]. To test the effect of annealing on the erosion behavior, HVOF coatings were annealed at 300 and 600 ^{0}C for both 1 and 8 hrs.

Figure 7.8 also shows the E_o values of all annealed coatings after four minutes of arcing. All coatings except H-600-8 coatings spalled after four minutes of arcing. This spalling is a catastrophic phenomenon. Once it starts, it increases rapidly leading to high E_o values. H-600-8 coatings gave a low erosion rate of 21.5 ± 5 μg/C and were intact at the end of four minutes arcing. Hence only H-600-8 coatings were further investigated.

Effect of coating initial thickness on erosion behavior of H-600-8 coatings: Because H-600-8 coatings were intact after four minutes of arcing, it was thought that the initial thickness of the coating would also affect the overall erosion rate. Six cathodes having different initial thickness (viz., two in the 100-150 μm range, two in the 350-400 μm range and two in the 800-850 μm range) were formed and annealed at 600 ^{0}C for 8 hrs in argon atmosphere. These coatings were eroded in UHP argon for different time lengths between six to ten minutes.

Typical arc velocity results for all three coating thickness range tested are shown in figure 7.10. We see from figure 7.10 that, except for 100-150 μm thick coatings, the general velocity trend for H-600-8 coatings was similar to that of M-Cu coatings. However, the absolute arc velocity values on H-600-8 coatings were higher than those of M-Cu.

For the 112 μm thick coating, visual inspection of the cathode after the erosion experiment showed that the coating was completely eroded. After completely eroding the coating, the arc had started to erode the substrate which was M-Cu. The arc velocity results for 112 μm thick coatings, shown in figure 7.10, corroborate this result. The arc velocity for 112 μm thick coating was high (55 m/s and reducing) in the first 300 s of operation because it was running on the coating. After 300 s of arcing all the coating was eroded and the arc started to run on M-Cu and hence the arc velocities drop to a low value of 6.6 ± 0.6 m/s.

Arc velocity results of annealed HVOF coatings suggest that these coatings behave similar to that of M-Cu. The arc velocity, shown in figure 7.10, for both 350 μm thick coatings and 850 μm thick coating had an initial unsteady fast regime for the first 150 s of arcing followed by a steady slow regime for the rest of the experiment. This is similar to the velocity trend of M-Cu except that the steady state velocity of H-600-8 coatings was about 12 ± 1.2 m/s whereas that of M-Cu was 6.6 ± 0.6 m/s. Again, the higher steady state velocity observed on H-600-8 coatings, would have been due to smaller grains or due to the oxygen content or both.

As the arc velocities for H-600-8 coatings were higher than M-Cu, one would expect lower E_o values for H-600-8 coatings relative to M-Cu. Figure 7.11 shows the E_o values for all the six H-600-8 coatings tested. We see that the E_o values were all lower than M-Cu as expected. All but 100-150 μm thick coatings were intact after arcing. Among three coating thickness ranges tested, the E_o values for 100-150 μm thick coatings were the highest (23 ± 1 μg/C). This agreed very well with the arc velocity results and the final state of the coating after erosion. This E_o value for a 100-150 μm thick coating was a

combination of erosion on coatings and on M-Cu. Hence 100-150 μm thick coating show higher E_o values.

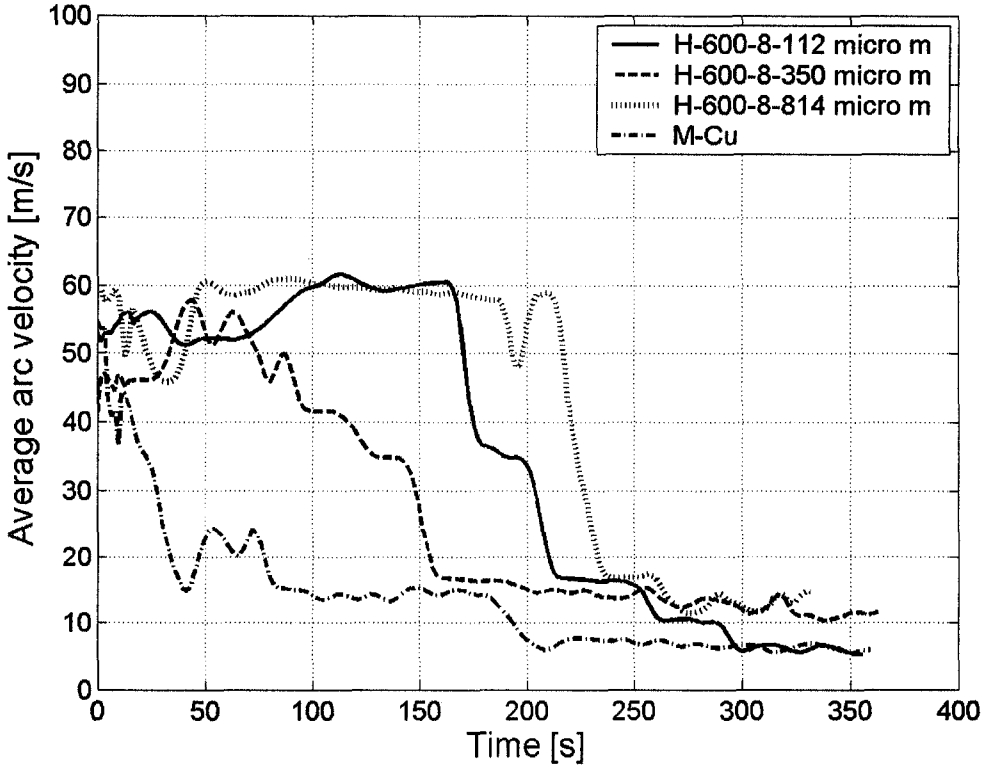

Figure 7.10 Arc rotational velocities for H-600-8 cathodes with different initial thickness. Notice for 112 μm thick cathode, after 300 s, the arc velocity has the same values as M-Cu.

From figure 7.11 we see that the cathodes which had 350-400 μm thick coatings gave lower E_o values compared to the cathodes which had coatings in 800-850 μm thickness range. Erosion rate, which is a chief function of heat removal from the cathode, is expected to be affected by the initial thickness of the coating. If one were to visualize coating as a resistance layer to heat removal, then having a thicker coating should result in poorer heat removal and hence higher erosion rates. The results shown in figure 7.11, agree with this argument.

In summary, we conclude that 300-350 μm thick H-600-8 coatings are a better cathode giving 3.5 times lower E_o than M-Cu. The low E_o values are attributed to the annealing of HVOF coatings. Gartner et al [23] have shown that annealing of HVOF sprayed Cu

coatings causes shperoidization of inter-splat oxide layer. They have demonstrated that during annealing of HVOF sprayed Cu coatings, the copper oxide layer present along the boundaries of an individual splat would precipitate, group together and appear as spheres of copper oxide. Also, they report increased electrical conductivity, thermal conductivity and metallic bonding between the spray splats due to annealing [23]. Hence, annealing HVOF coatings resulted in a coating with near equi axed grains in 2 to 3 μm range, with spheres of oxide distributed in them. We believe that, the reduced grain size caused higher arc velocities and shperoidization of the oxide layer resulted in reduced spalling. Due to a combination of these two factors annealed H-600-8 coatings gave lower erosion rates than M-Cu.

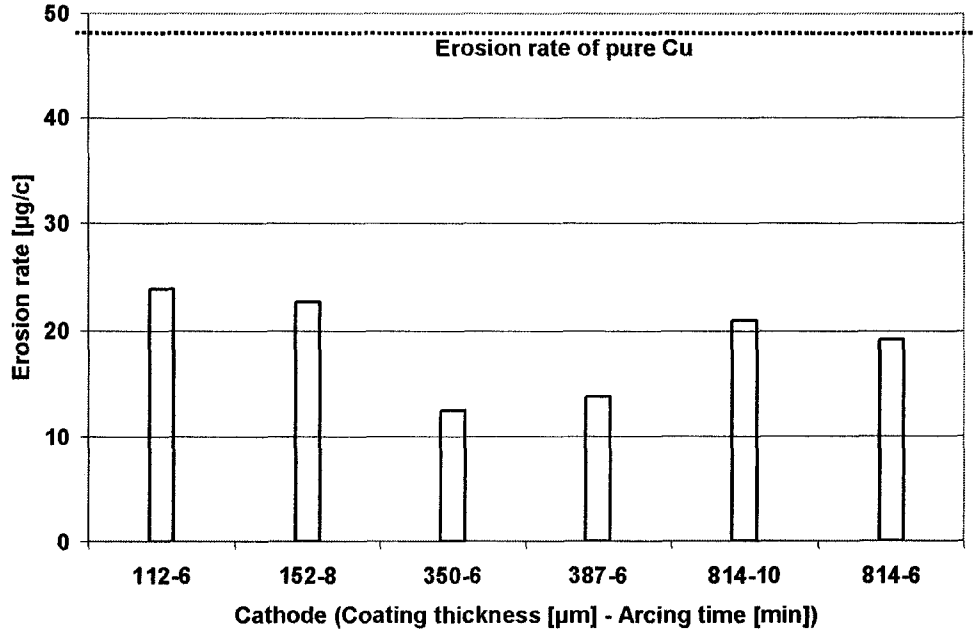

Figure 7.11 Overall erosion rate, Eo vs. initial coating thickness of H-600-8 coatings.

7.3.3.5 Arc velocity and erosion of VPS-as-sprayed cathodes in argon atmosphere

Erosion experiments were also conducted for VPS coatings. Cathodes prepared were having coatings in three different thickness ranges (viz., 100-150 μm, 350-400 μm and 800-850 μm) and were eroded for six or more minutes. VPS coatings differed from HVOF coatings in two ways. The average grain size of the VPS coatings was 0.9 to 1.5

μm whereas that of HVOF coatings was 2 to 3 μm. VPS coatings are known to have zero or minimal oxygen content [30] whereas HVOF coatings had ~2 at% oxygen.

Figure 7.7 also shows the typical arc velocity results for V-as-sprayed coatings. We can see from figure 7.7 that, unlike M-Cu and similar to H-as-sprayed coatings, the arc rotation velocity of VPS coatings show only one fast regime for most of the experiment. On VPS coatings, the arc velocity which started off around 52 m/s remains high for most of the experiment and appears to decay only in the last 30 s of the experiment. VPS coatings differed from M-Cu only in their grain sizes. Hence the reason for the high velocity was attributed to the difference in the microstructure of the cathode. These results show a clear effect of microstructure on arc velocity.

Due to its high velocity, one would expect a low E_o values for VPS coatings. The E_o values for VPS coatings as a function of their initial thickness is shown in figure 7.12. The E_o values obtained for all the VPS cathodes tested were lower than M-Cu. This result is in total agreement with the arc velocity results shown in figure 7.7. All VPS coatings were intact after erosion experiment and very little or no spalling of the coating was observed. Figure 7.13 shows a picture of the VPS cathode before and after an erosion experiment. We see that the highest erosion rate obtained for the VPS coatings was 17 ± 2 μg/C, which is 2.2 times lower than that of M-Cu.

From figure 7.12, we see that lowest erosion rates were obtained for 100-150 μm thick coatings. The erosion rates for both 350-400 μm thick coatings and 800-850 μm thick coatings were similar with overlapping error bars. This result suggests that, having a very thin coating gives the low erosion rates. Increasing the coating thickness beyond 350 μm does not seem to affect the overall erosion rates. For VPS coatings, we see an increase in erosion rates when coating thickness is increased from 150 to 400 μm whereas for HVOF coatings, we see an increase in erosion rates when the coating thickness was increased from 400 to 850 μm.

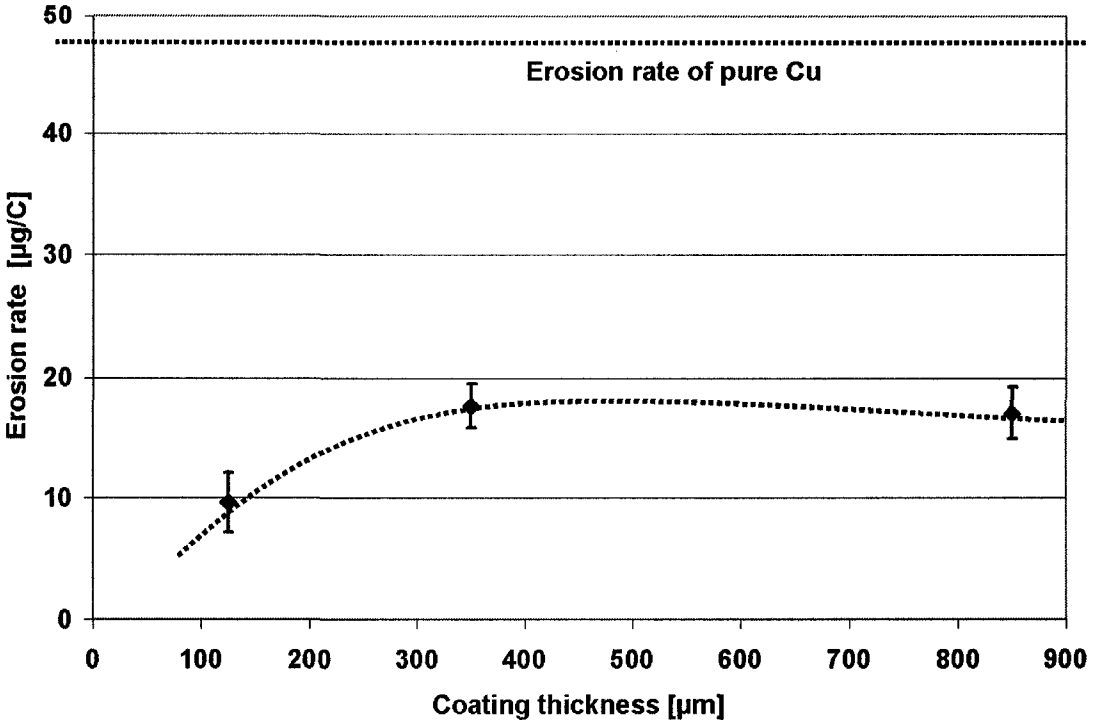

Figure 7.12 Overall erosion rate Eo vs. coating thickness for V-as-sprayed coatings.

7.3.3.6 Arc velocity and erosion of VPS-as-sprayed cathodes in an oxidizing atmosphere

VPS cathodes were eroded in an oxidizing atmosphere (UHP argon and 10% v/v extra dry air, < 2 ppm moisture) and the results obtained were compared with M-Cu cathodes also eroded in an oxidizing atmosphere. This isolates the effect of microstructure by eliminating any effect of oxide. The results obtained are presented below.

Figure 7.5 also shows typical arc velocities on V-as-sprayed coatings in an oxidizing environment. For first 50 s of arcing, while the plasma forming gas was only UHP argon, the arc velocity on V-as-sprayed cathode started at 50 m/s and was steady. Under similar conditions, M-Cu showed a reducing unsteady behavior as shown in figure 7.5. The high steady velocity on V-as-sprayed coatings is attributed to the lower grain size of VPS coatings.

Figure 7.13 Picture of the VPS coated cathodes a) before erosion; b) after erosion.

Between 50 to 70 s, the arc velocity on V-as-sprayed coatings increased to 110 m/s due to the change in plasma gas to an oxidizing atmosphere.. Beyond 70 s, this arc velocity remains high and steady at 52 m/s until the end of experiment. The momentarily high velocity seen during the gas change interval may be due to a combination of the smaller grains of VPS coating and formation of copper oxide. We believe that, during this 20 s time interval, copper oxide formation is in its transient state and the layer formed is very thin. The combination of this thin oxide layer and the smaller grains of the VPS coating favors these very high velocity of 110 m/s. Beyond 70 s, an appreciable layer of copper oxide has formed and the grain size effect no longer influences the arc velocity. The results indicate that once a thick layer of copper oxide is formed, the arc velocity becomes independent of the grain size and hence reach a steady value of 50 m/s similar to M-Cu. Similar observations are reported by Szente et al [1, 3]

Figure 7.6 also shows the E_o values for V-as-sprayed cathodes in an oxidizing atmosphere, which is 9.64 ± 2.16 μg/C. This is similar to the E_o value of M-Cu. Except for the first 70 s of experiment, the arc velocities on both M-Cu and V-as-sprayed

cathodes were steady and high. Hence we see lower erosion rates for both of these cathodes.

7.3.4 Characterization of eroded coatings

Only the cathodes which gave low erosion rates than M-Cu i.e., H-600-8 coatings and VPS coatings were analyzed to check for microstructural changes. In both the coatings, the SEM analysis of the coatings after erosion experiments showed no microstructural changes in the bulk of the coatings. Both of these coatings had similar grain size distributions as the one shown in figure 7.2 and hence are not reported here. Only a thin layer in the outmost splats, which came in direct contact with the arc showed indication of melting and rapid solidification as shown in figure 7.14. This indicates that the initial grain size distribution was preserved even after six to ten minutes of arcing.

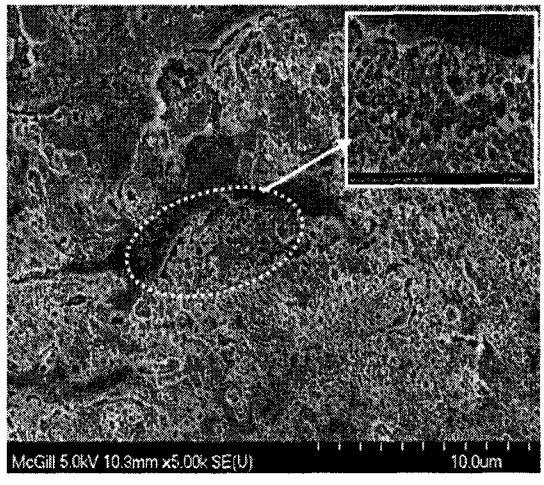

Figure 7.14 SEM image of the V-as-sprayed coating after erosion; inset shows high magnification picture. Notice signs of melting and rapid solidification in the highlighted region.

7.4 Conclusions

In this work we have studied the effect of microstructure on the arc velocity and erosion rate of copper electrodes in a magnetically driven atmospheric pressure arc system. It has been shown that finer microstructure, in the submicron to nanometer range results in higher arc velocities and lower erosion rates.

In argon, VPS coatings which were free of intersplat oxide layers and had 0.9 to 1.5 μm grains gave highest arc rotational velocities (up to 60 m/s) and ~60% lower erosion rates relative to bulk Cu cathodes. VPS coatings which were free from intersplat oxide layer isolate the effect of microstructure alone on the arc velocity and arc erosion rates of copper cathodes. In the case of the VPS coatings, increasing the initial thickness from 100-150 μm to 350-400 μm also increased the erosion rates from 9 ± 2 μg/C to 17 ± 2 μg/C. Beyond 400 μm the coatings initial thickness did not effect the overall erosion rate.

Spalling of the cathodes was the main reason for the higher erosion rates in the case of HVOF coatings. Annealing the HVOF coatings, increased the electrical and thermal transport properties as well as metallic bonding of the coating. Annealing caused spheroidization of intersplat oxide layer which reduced the spalling of the coating and hence reduced the erosion rates. The initial thickness of the HVOF coatings also affected the overall erosion rates. H-600-8 coatings which had an initial thickness in the range of 350-400 μm gave 68% lower erosion rates than bulk Cu.

Experiments conducted with an oxidizing atmosphere could not show a definitive effect of microstructure alone due to formation of copper oxide on both the coated and un-coated cathodes. The arc velocity on both coated and un-coated cathodes were high in the oxidizing atmosphere. However, a small effect of microstructure was seen during a transient period of gas switching. The erosion rates on both types of cathodes were similar with overlapping error bars.

7.5 Acknowledgements

The authors express their gratitude to Dr. Christian Moreau and Dr. Jean-Gabriel Legoux of IMI, Montreal, Canada, for producing the coatings, their valuable suggestions and discussions. The financial support of the Natural Sciences and Engineering Research Council of Canada for the work is gratefully acknowledged.

7.6 References

1. Szente R N, R J Munz and Drouet M G 1992 Electrode erosion in plasma torches *Plasma Chemistry and Plasma Processing* **12** 3 327-343.
2. Guile A E and Hitchcock A H 1981 Effect of transverse magnetic field on erosion rate of cathodes of rotating arcs *Proc. IEE* **128** 117-122.
3. Szente R N, R J Munz and Drouet M G 1987 Effect of low concentrations of a diatomic gas in argon on erosion of copper electrodes in a magnetically rotated arc *Plasma Chemistry and Plasma Processing* 7 349-364.
4. George A P and Hare A L 1983 Arc heater operating characteristics on oxygen and nitrogen, an interim report *Proc. ISPC-6* IUPAC Montreal A-5-2 144-147.
5. Porto D R, C W Kimblin and Tuma R J 1982 *Journal of applied physics* **53** 4740-4749.
6. Szente R N 1989 Erosion of plasma torch electrodes PhD Thesis Department of Chemical Engineering McGill University Montreal Canada.
7. Teste P, T Leblanc, R Andlauer and J P Chabrerie 2001 Copper cathode erosion by an electric arc—the causes of the variations of the erosion rate with the electrode gap *Plasma Sources Sci. Technol.* **10** 2001 10-16.
8. Guile A E and Hitchcock A H 1975 Effect of water cooling on erosion of the copper cathode of a rotating arc *Proc. IEE* **122** 579-580
9. Guile A E and Hitchcock A H 1975 Erosion of copper cathodes by moving arcs at currents of 45-800 A *Proc. IEE* **122** 763-764
10. Guile A E and Hitchcock A H 1978 The erosion of copper cathodes from vacuum to atmospheric pressure arcs *Journal of applied physics* **49** 7 4275-4276
11. Fu Y H and Smeets R P P 1989 The influence of contact surface microstructure on vacuum arc stability and voltage *IEEE Transactions on plasma science* **17** 5 727-729
12. Fu Y H 1989 The influence of cathode surface microstructure on DC vacuum arcs *J. Phys. D: Appl. Phys* **22** 94-102.

13. Lakshminarayana Rao, Munz R J and Meunier J-L 2007 Vacuum arc velocity and erosion rate measurements on nanostructured plasma and HVOF spray coatings *J. Phys. D: Appl. Phy* **40** 4192-4201.
14. Fu Y H and Smeets R P P 1989 The influence of contact surface microstructure on vacuum arc stability and voltage *IEEE Transactions on plasma science* **17** 5 727-729.
15. Schmoll R 1998 Analysis of the interaction of cathode micro protrusions with low-temperature plasmas *J. Phys. D: Appl. Phys.* **31** 1841-1851.
16. Farrall G A 1985 Electrical breakdown in vacuum *IEEE Transaction on electrical insulation* 20 815-841.
17. Juttner B, Pursch H and Shilo V A 1984 The influence of surface roughness and surface temperature on arc spots movement in vacuum *J. Phys. D: Appl. Phys* **17** L31-L34.
18. Daalder J E and Vos C W M 1972 Distribution functions of the spot diameter for single and multi cathode discharges in vacuum Eindhoven University of Technology Eindhoven Netherlands Rep 72-E-32.
19. Ding B, Yang Z and Wang X 1996 Influence of microstructure on dielectric strength of CuCr contact materials in vacuum *IEEE Transactions on Components, Packaging and Manufacturing Technology Part-A* **19** 1 76-81.
20. Wang Y P and Ding B J 1999 The preparation and their properties of microcrystalline and nanocrystalline CuCr contact materials *IEEE Transactions. CPT* **22** 467–72.
21. Wang Y, Zhang C, Zhang H, Ding B and Lu K 2003 Effect of the microstructure of electrode materials on arc cathode spot dynamics *J. Phys. D: Appl. Phys.* 36 2649-2654.
22. Zhang C, Yang Z, Wang Y and Ding B 2003 Cathode spot propagation on the surface of amorphous, nanocrystalline and crystalline $Cu_{60}Zr_{28}Ti_{12}$ cathodes *Physics Letters A* **318** 435–439.
23. F Gartner, T Stoltenhoff, J Voyer, H Kreye, S Riekehr and Koçak M 2006 Mechanical properties of cold-sprayed and thermally sprayed copper coatings *Surface Coatings and Technology* **200** 6770-6782.

24. S Sampath, X Y Jiang, J Matejicek, L Prchlik, A Kulkarni, and Vaidya A 2004 Role of thermal spray processing method on the microstructure, residual stress and properties of coatings: an integrated study for Ni–5 wt% Al bond coats Materials Science and Engineering A **364** 216–231.
25. Houlbert A S, Cielo P, Moreau C and Lamontange M 1994 Measurement of thermal diffusivity and anisotropy of plasma sprayed coatings *International Journal of Thermophysics* **15** 3 525-546
26. Dent A H, Horlock A J, McCartney D G and Harris S J 2001 Microstructural characterization of a Ni-Cr-B-C based alloy coating produced by high velocity oxy-fuel thermal spraying *Surface and Coatings Technology* **39** 244-250
27. Edris H and Mccartney D G 1997 Microstructural characterization of high velocity oxy-fuel sprayed coatings of Inconel 625 *Journal Of Materials Science* **32** 863-872
28. Rao L 2007 Effect of cathode microstructure on erosion of copper cathodes-an experimental study PhD Thesis Department of Chemical Engineering McGill University Montreal Canada.
29. Szente R N, R J Munz and Drouet M G 1989 Cathode erosion in inert gases: the importance of electrode erosion *Plasma Chemistry and Plasma Processing* **9** 1 121-132.
30. T N McKechnie, Y K Liaw, F R Zimmerman and Poorman R M 1994 Metallurgical and process comparison of vacuum plasma spray forming on internal and external surfaces-a technical note **3** 3 270-274.

Chapter 8 Effect of cathode microstructure on arc velocity and erosion rate of cold-sprayed copper cathodes in magnetically rotated atmospheric pressure arcs

This chapter presents the erosion behavior of cold sprayed Cu coatings in atmospheric pressure arc setup. The characterization of the powder and the method used to produce cold sprayed coatings is presented along with coating characterization. Erosion rates of these coatings in their as-sprayed and annealed state are presented.

Results presented in this chapter corroborate the results presented in chapter 7. Cold sprayed coatings had grains in the micrometer range and were free from the oxide content. These coatings gave higher velocities showing a clear effect of microstructure. However due to poor thermal properties as-sprayed coatings severely spalled under the arc and resulted in higher erosion rates. Annealing improved the thermal properties and reduced spalling which lead to lower erosion rates.

Abstract

Atmospheric pressure arc velocity and erosion measurements were performed on cold-sprayed cathodes in a continuously running arc system. Ultra-high purity (UHP), 99.99% pure, argon was used as plasma forming gas. An external magnetic field of 0.10 T was used to rotate the arc, which was operated at a constant power of 6 kW (40 V and 150 A). Cathodes having microstructures with different grain sizes, ranging from 1.12 μm to 3.06 μm, were produced using cold spraying (CS) and annealing methods. CS cathodes were tested for arc velocity and erosion in their as-sprayed state and also after annealing them at 300 and 600 ^{0}C for 1 and 8 hr durations in an inert argon atmosphere. Annealing CS coatings at 600 ^{0}C for 1 hr, produced near equi-axed grains of 2.29 μm average size. These coatings gave 60% higher steady state arc velocities and up to 50% lower erosion rates than massive copper cathodes having 20 to 23 μm average grain size. The results show a clear effect of cathode microstructure on arc velocity and on arc erosion rates.

8.1 Introduction

Thermal plasma technology plays an important role in materials processing and waste treatment [1]. Plasma-torches using cold cathodes in tubular geometry are used for high-power applications such as melting, cutting and spraying [2]. Erosion of electrodes limits the application of these torches into many industries. The erosion of electrodes results in their short lifetimes and frequent replacement, thereby increasing the operating cost of a plasma system. Previous studies on cold cathode plasma-torches have shown that the degree of erosion of the cathode is far greater than that of the anode [1, 3]. Thus, much importance has been placed on finding methods to reduce cathode erosion.

Cathode erosion is a complex process affected by many operating parameters, such as the magnetic field strength used to rotate the arc, plasma gas chemistry, arc current and voltage as well as characteristics of the electrodes, such as the electrode chemistry, geometry and the cathode microstructure [3-6]. Researchers have shown an effect of cathode microstructure on arc attachment, movement and on its erosion rates [7]. Wang et al., working with nanostructured CuCr alloy cathodes and $Cu_{60}Zr_{28}Ti_{12}$ cathodes, observed that the erosion rates on these electrodes were lower compared to conventional cathodes (4%-20% less than massive Cu) [7].

An earlier study in our group has shown that, for vacuum arcs, nano-structured cathodes produced by atmospheric pressure plasma spraying (PS) and high velocity oxy-fuel (HVOF) spraying give lower erosion rates than massive copper cathodes with relatively large grain sizes [6]. In addition to their nano-structured grains, electrodes produced by PS and HVOF methods have inter-splat oxygen content of ~2 at%. It is known that the presence of oxygen in the cathode reduces its erosion rate [8]. Hence, the low degree of erosion reported by Rao et al. may be due to the nanostructure of the coatings and/or the oxide content of the coated cathode [6]. Isolating the effect of microstructure from the oxide content and studying its effect on arc erosion is of fundamental interest. Cold spraying (CS) can produce oxide-free coatings having grain sizes in the micro-scale rather than nano-metric range [9]. Hence, cold-sprayed cathodes are ideal for isolating the

effect of microstructure only on erosion behaviour.

Rao has shown that cathodes with small grain sizes have higher arc velocities and hence, low erosion rates [6, 10]. Therefore, cold-sprayed coatings having smaller grain sizes than massive copper cathodes are expected to have higher arc velocities and, possibly, lower erosion rates than massive copper. However, due to weak inter-splat bonding and substrate-coating bonding, CS as-sprayed coatings have lower electrical and thermal conductivities than pure copper [11]. As erosion of cathodes is primarily controlled by heat removal from the cathode, having a low thermal conductivity coating may not reduce erosion. However, heat treatment of CS coatings is known to improve the electrical and thermal transport properties as well as the metallic bonding of the coating [11]. Wen-Ya Li et. al have shown that, for CS copper coatings sprayed on Cu substrates, annealing enhances adhesion of the coating to its substrate as well as metallic bonding between the splats [11].

In this paper, we report on the effect of microstructure on the arc erosion behaviour of copper cathodes. CS copper coatings having submicron to a few micron grain sizes in their as-sprayed and annealed state were tested for arc erosion behaviour. The results obtained were compared with massive copper (M-Cu), having 20-23 μm grain size. Erosion behaviour was characterized by the erosion rates, arc rotation velocities and morphology of eroded cathodes.

8.2 Materials and experimental methods

8.2.1 Characterization of powders

Amperit 190 (gas-atomized, 99.99% pure copper powder, oxygen content 500 ppm max; further referred to as A-190) was used as the spray powder for cold-spraying. The morphology of the powder was studied using field emission scanning electron microscopy (SEM), whereas the particle size distribution was determined using the Mastersizer-2000 particle size analyzer (PSA) with distilled water as the dispersant. Energy dispersive spectroscopy (EDS) and inductively coupled plasma mass

spectroscopy (ICP) were used to determine the chemical composition of A-190.

8.2.2 Preparation of cathodes

Two different substrates viz., square copper plates (60mm × 60mm × 2.5mm), and oxygen-free, high conductivity, 99.99% pure copper hollow cylinders (25 mm outer diameter, 65 mm length) were used for CS spraying. All the substrates were grit blasted with 708 μm alumina grits, just before coating and had a surface roughness Ra of 8.58 μm. The spraying process was carried out with the Kinetics 3000 cold-spray gun (Cold Gas Technology Gmbh), at a chamber pressure of 32 bar and 500 °C.

The CS coated hollow cylinders and copper plates were annealed in an argon atmosphere in a tubular furnace. A full factorial two temperature (viz., 300 ^{0}C and 600 ^{0}C), two annealing times (viz., 1 hr and 8 hrs) experimental design was chosen for annealing. Before starting the annealing procedure, the specimens were placed inside the tubular furnace and the furnace was flushed with ~90 furnace volumes of 99.99% pure argon gas flowing at 3 slpm. After purging, the heating was started, maintaining the argon flow rate to reach the desired annealing temperature. It took less than 10 minutes to reach the desired annealing temperature. The specimens were held at this temperature for either 1 hr or 8 hrs. Then the heating was stopped and the specimens were allowed to cool to room temperature inside the furnace, while still maintaining the argon flow. Annealed cylinders were used as cathodes for erosion studies whereas Cu plates were used for microscopic analysis.

For microscopic analysis, the coatings on Cu plates were cut using a Struers 'Secotom-10' universal precision cut off machine and vacuum mounted in cold setting resin. The mounted specimens were wet ground using SiC paper #800, 1200 and 4000 under running tap water. The ground samples were the polished using 3 μm and 0.04 μm silica suspensions. The polished samples were etched with a $FeCl_3$ etchant (2.5 g of $FeCl_3$ + 10 ml of HCl + 50 ml of ethanol) for 5 seconds. The etched coatings were examined under optical microscope and SEM to determine their microstructure. To determine the porosity

of the coatings, as many as 10 SEM pictures of polished coatings (prior to etching) were taken at regular intervals on each of the coatings and the porosity of individual pictures was measured by an image analysis technique. An average of these numbers were calculated and reported as porosity with a standard deviation of ± 5% of the average. SEM pictures of etched coatings were used to calculate grain sizes. An average and standard deviation of the grain size measurements taken from multiple SEM pictures of a given coating was calculated and are reported here.

8.2.3 Erosion setup and procedure

Figure 8.1 is a schematic diagram of the erosion apparatus. Figure 8.1a shows an overview of the setup while figure 8.1b gives the electrode dimensions. It was only practical to coat hollow cylinders externally, so the water cooled coated hollow cylinder was used as the cathode, surrounded by a sleeve anode, with a minimum annular gap of 4 mm. Both electrodes were water-cooled. A water-cooled solenoid around the electrode assembly was used to apply an axial magnetic field of 0.10 T, to rotate the arc. The axial magnetic field strength varied less than 3% radially and 5% axially within the test cathode. The arc was ignited by a high-frequency trigger pulse and powered by a welding power supply (maximum power and current of 78 kW and 500 A, respectively). An average power of 6 kW (40 V and 150 A) was maintained throughout the experiment. Experiments were conducted using ultrahigh purity (99.99% pure) argon as the plasma forming gas, which circulated from the lower end of the reactor to the top end at a flow rate of 23 slpm, under atmospheric pressure.

The cathode was weighed, to an accuracy of $\pm 5\times10^{-4}$ g, and installed in the reactor. An optical detector as shown in figure 8.1a was used to capture the arc rotation frequency. It consisted of a photodiode and a collimating lens assembly having a narrow field of view of 3 mm. The optical detector assembly was aligned to view the arc between the electrodes and gave a positive voltage output when the arc passed its field of view. This optical voltage output, the arc current and arc voltage waveforms were recorded simultaneously onto a computer using LabVIEW, at 10 kHz sampling rate. After the

erosion experiment, the cathode was removed from the reactor and dried of cooling water completely before recording its final weight. The erosion rate values in grams per coulomb were calculated by dividing the weight difference of the cathode before and after arcing by the total electric charge, $Q = \int I\, dt$, passing through the cathode. The arc rotation frequency was calculated from the recorded optical voltage data using windowed fast Fourier transform analysis. For each type of cathode, two individual experiments were performed and an average erosion rate and standard deviation were determined and reported.

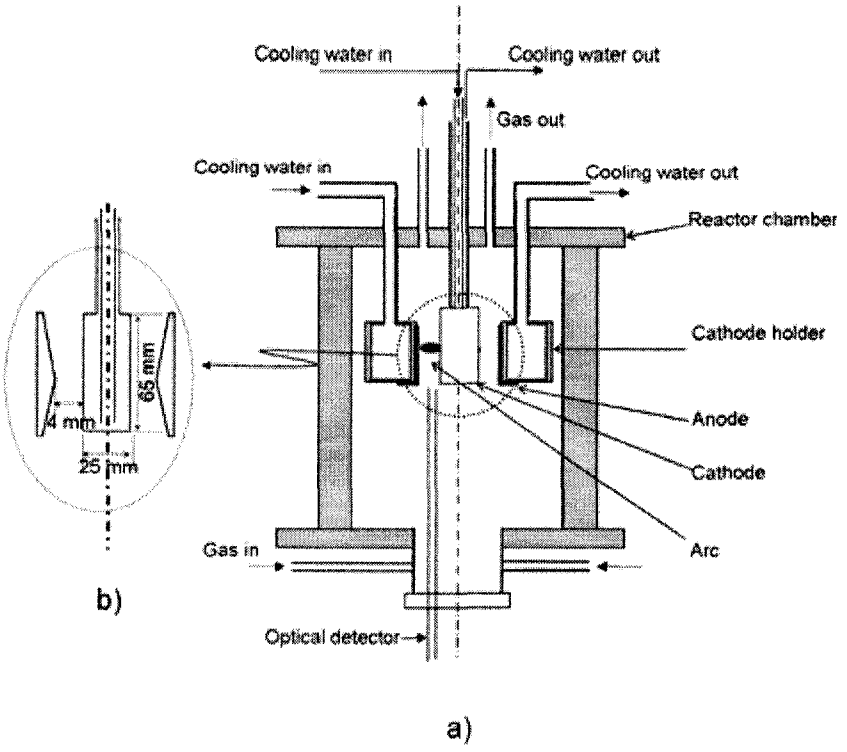

Figure 8.1 Schematic diagrams of a) the continuous-arc reactor and b) the electrode setup

8.3 Results and Discussion

8.3.1 Characterization of powders

Figure 8.2a shows an SEM image A-190. The main picture shows the morphology of the powder and the inset shows an individual particle. We see that, most particles were spheroids and only a few appeared as agglomerates. The energy dispersive spectrum, shown in figure 8.2b, revealed only peaks for Cu and O. The oxygen peak was attributed

to surface oxidation of copper. The particle size distribution, shown in figure 8.2c, was log normal ranging between 7 to 50 μm, with a peak at 20 μm.. ICP analysis of the powder revealed it to be 99.99% pure copper, with no detectable contaminants.

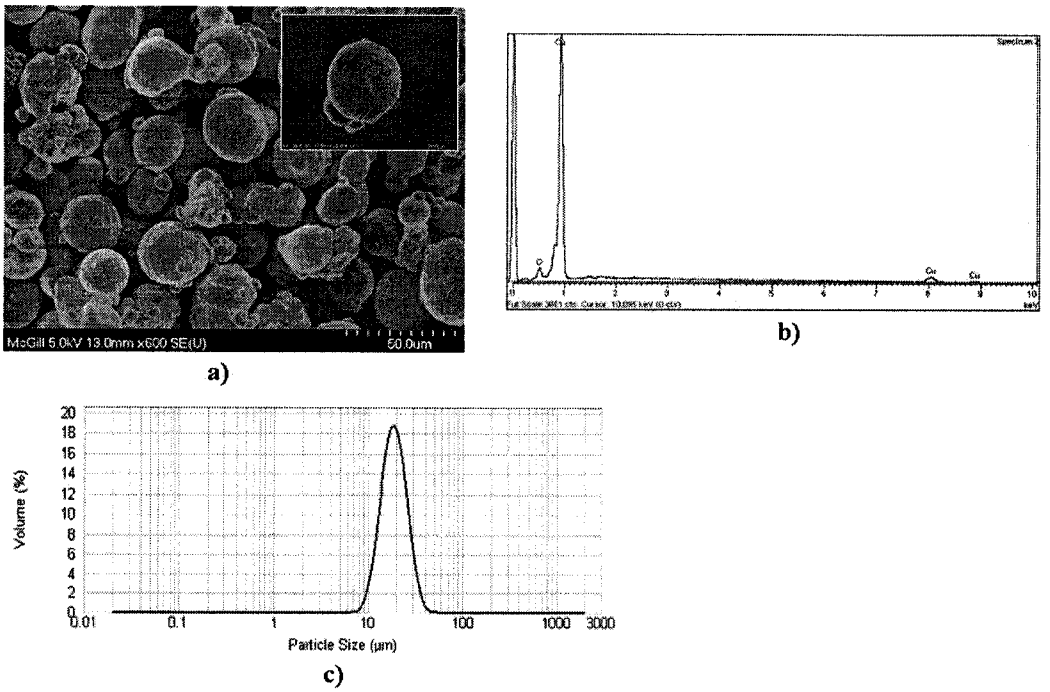

Figure 8.2 Characterization of A-190 particles - a) Morphology and an individual particle (inset), b) energy dispersive spectrum and c) particle size distribution

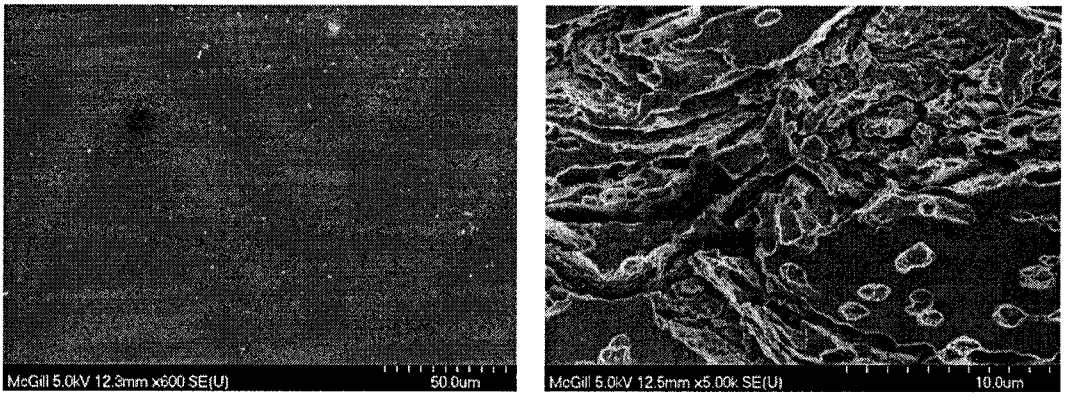

Figure 8.3 SEM images of as-sprayed coatings a) Un-etched cross-section ; b) etched cross-section.

8.3.2 Characterization of as-sprayed coatings

Porosity and grain size: Figure 8.3a shows an SEM image of an un-etched cross-section of CS as-sprayed coatings. We see that the CS-as-sprayed coating was dense and had a coating porosity of <1%. After etching, the inter-splat boundaries and the grain boundaries were visible as shown in figure 8.3b. Grain size measurement of CS-as-sprayed coatings showed that the average grains of CS-as-sprayed coatings were 1.17 ± 0.26 μm. Average grain sizes of as-sprayed coatings are shown in figure 8.4.

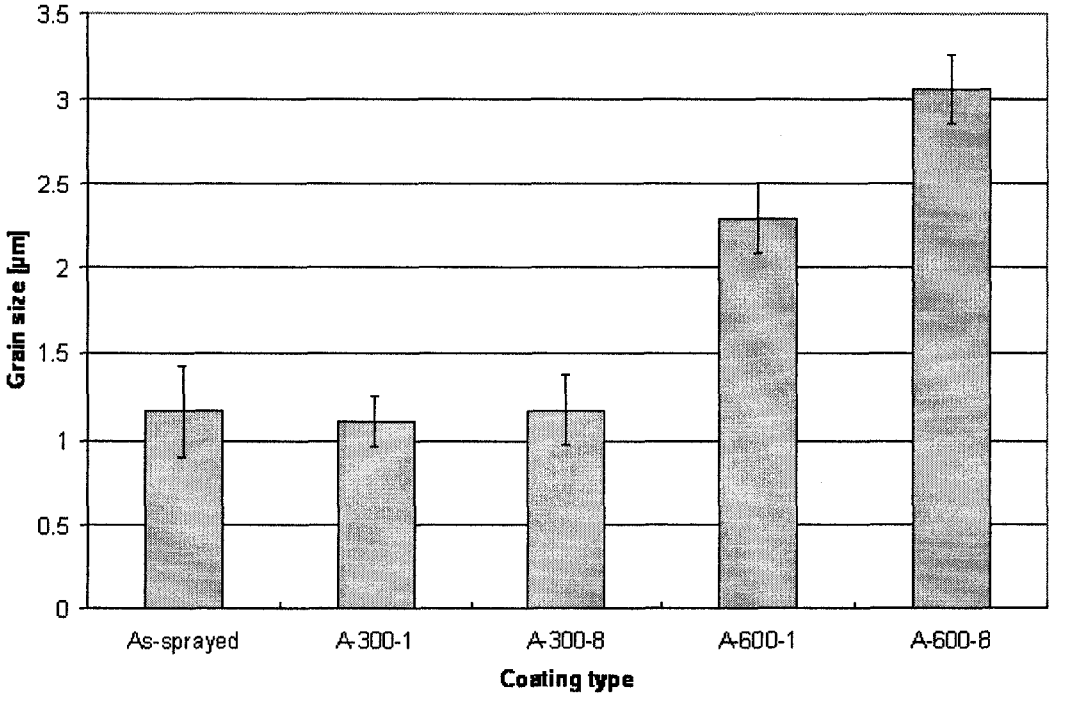

Figure 8.4 Average grain size measurements for as-sprayed and annealed coatings

Oxygen content: To check the O content in the coating, EDS spot analysis was performed on CS coatings, by holding the electron beam at a single spot on the inter-splat boundary. The result obtained was compared with a similar analysis on HVOF coatings and is shown in figure 8.5. We see that, both CS and HVOF coatings had carbon, copper and oxygen peaks. The carbon peak was attributed to carbon contamination within microscope and the O peak to the native oxide layer present on the Cu powder used to make the coatings. A closer look at the oxygen peak, shown in the inset of figure 8.5, reveals that, CS coatings had a small oxygen peak compared to HVOF coatings, which

had ~2 at% of O. This small O peak was in agreement with the O content quoted by the manufacturer, which was 500 ppm max. Low oxide content is typical of CS coatings since the CS coatings were formed without melting of the copper particles.

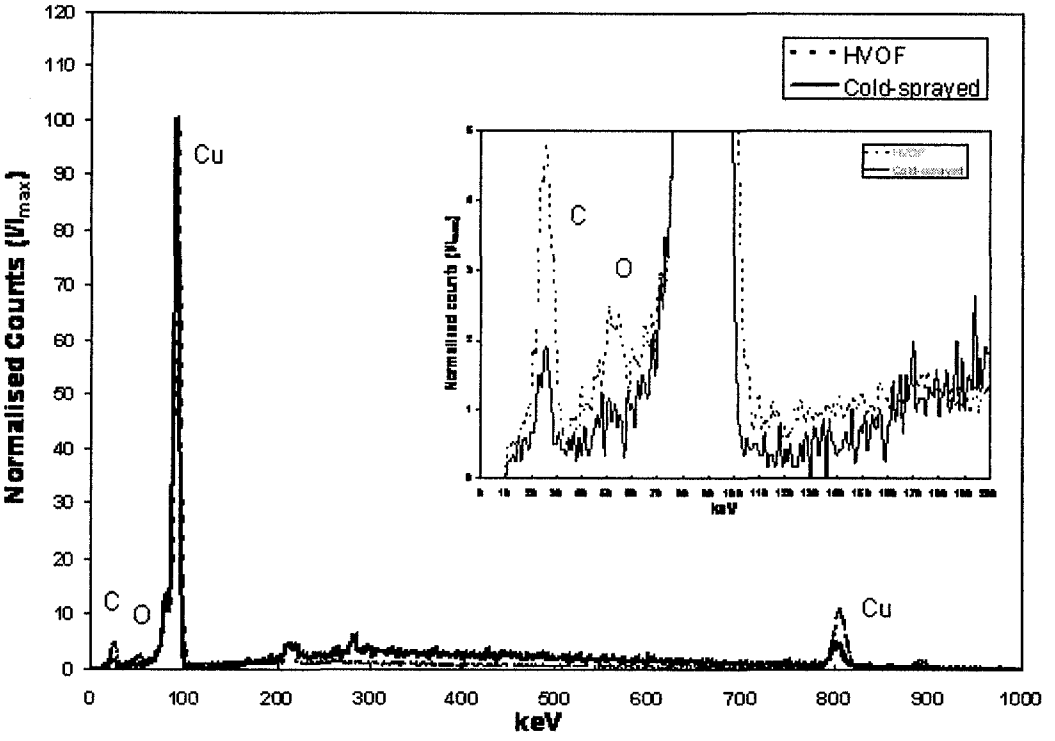

Figure 8.5 EDS spot analyses of HVOF and CS coatings showing Carbon, Oxygen and Copper peaks. Notice the higher oxygen peak for HVOF coatings than CS coatings (inset).

8.3.3 Characterization of annealed coatings

Figure 8.6 shows an SEM image of an un-etched CS coating annealed at 300 °C for 1 hour (referred to as A-300-1). Similar images were taken of A-300-8, A-600-1 and A-600-8, all showing a dense coating with porosities of <1 %. Based on these results, it was concluded that heat treatment did not increase the porosity of cold-sprayed coatings.

Figures 8.7a to 8.7d are SEM images of etched A-300-1, A-300-8, A-600-1 and A-600-8, coatings respectively. Average grain-size measurements taken from similar images are reported in figure 8.4. We can see a clear effect of annealing at high temperatures on the micro-structure of these coatings. Figures 8.4 and 8.7 show that annealing at 300 °C does not promote grain growth through diffusion. Hence, the grain sizes reported for as-

sprayed, A-300-1 and A-300-8 coatings are similar (1.17 ± 0.26 μm, 1.11 ± 0.14 μm and 1.17 ± 0.20 μm, respectively). Annealing at 600 °C, however, induces significant grain growth. We also see that coatings annealed for 8 hours had grains which were 33% larger than those annealed for 1 hour only.

Figure 8.6 Un-etched cross-section of an A-300-1 coating.

Average grain sizes for A-600-1 and A-600-8 coatings were 2.29 ± 0.21 μm and 3.06 ± 0.21 μm, respectively. As shown in figure 8.7, the grains formed on all the coatings were equi-axed. Figure 8.4 summarizes the average grain measurement of all the coatings. Among all the coatings formed, A-600-8 coatings had the largest grains; measuring 3.06 ± 0.21 μm. Our observations are similar to the findings of Wen-Ya Li et al [11].

8.3.4 Arc velocity and erosion results

8.3.4.1 Arc velocity and erosion results for central M-Cu cathodes

Since the central cathode geometry was used for cold-sprayed cathodes, it was necessary to obtain erosion results for M-Cu in a similar setup. These results could be used as a base line to compare with the arc velocity and erosion rates of CS coatings. The full details of the erosion measurement on central M-Cu are presented elsewhere [12]. The erosion rate of M-Cu cathodes in argon atmosphere for an arc time of 6 minutes is 47 ± 5 μg/C.

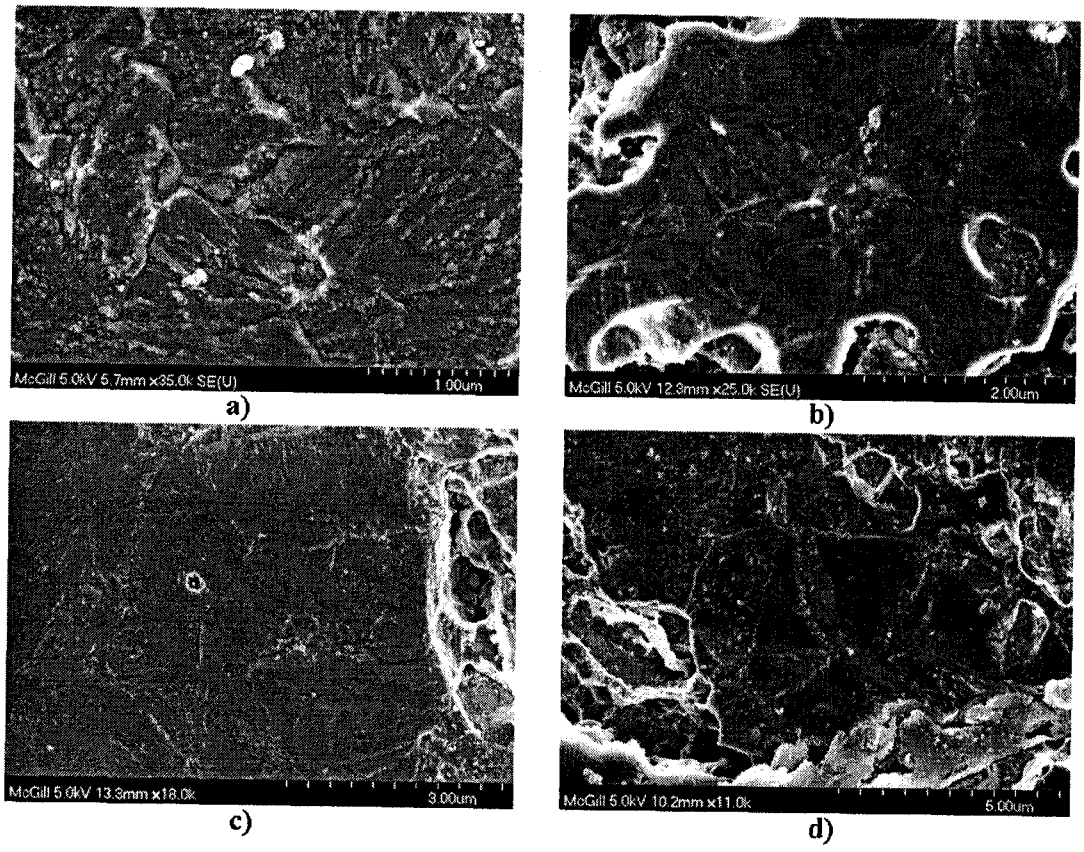

Figure 8.7 SEM Images of annealed coatings a) A-300-1, b) A-300-8, c) A-600-1 and d) A-600-8 c

8.3.4.2 Arc velocity and erosion results of as-sprayed and annealed CS cathodes

Figure 8.8 shows typical arc velocities of as-sprayed cathodes after four minutes of arcing. Arcing was stopped after four minutes due to spalling of the coating. We see from figure 8.8 that, unlike M-Cu, the arc velocity on as-sprayed coatings has only one unsteady regime where it oscillates between 45 and 10 m/s. For M-Cu, the arc rotation velocity starts off at 55 m/s but eventually drops below 6.6 ± 0.6 m/s after 200 s of arcing. Figure 8.9 shows an eroded, as-sprayed cathode. Severe spalling of the coating is evident from figure 8.9. This spalling, which is catastrophic in nature, is believed to be the reason for the unsteady velocities seen on as-sprayed coatings. Although the mean arc velocities on as-sprayed coatings were higher than that of M-Cu, we cannot draw any conclusion on the effect of microstructure on arc velocity and erosion rates, due to severe spalling of the coating. The erosion rates for as-sprayed coatings, after four minutes of arcing, are shown in figure 8.10. Severe spalling was the reason for higher erosion values

on these CS-as-sprayed cathodes. Hence, further efforts were made to reduce spalling of the coatings by annealing.

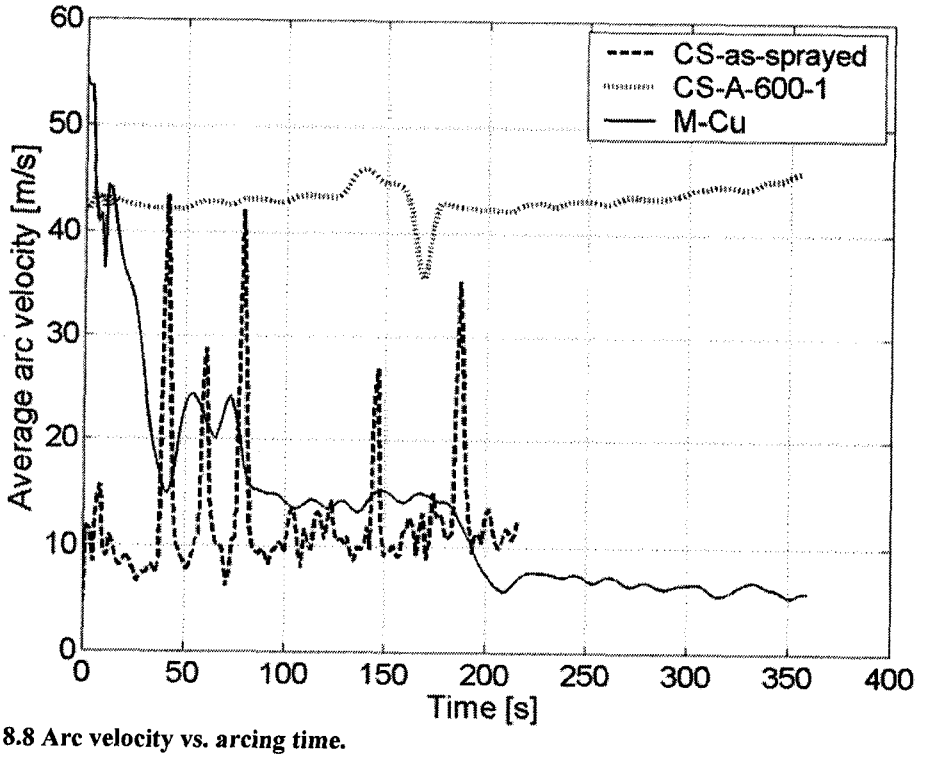

Figure 8.8 Arc velocity vs. arcing time.

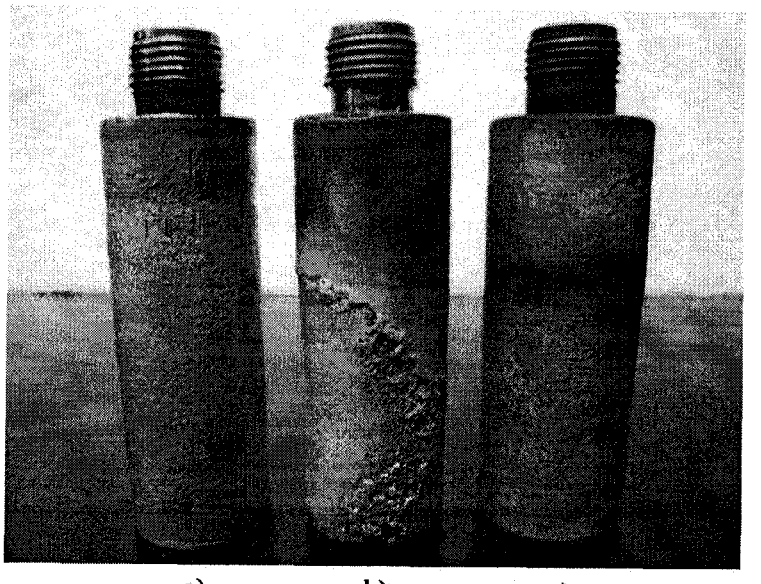

a) b) c)

Figure 8.9 Pictures of the cathode after erosion a) M-Cu, b) as-sprayed and c) A-600-1 cathodes. Notice the severe spalling of the as-sprayed cathode. Both M-Cu and A-600-1 cathodes remained intact after erosion.

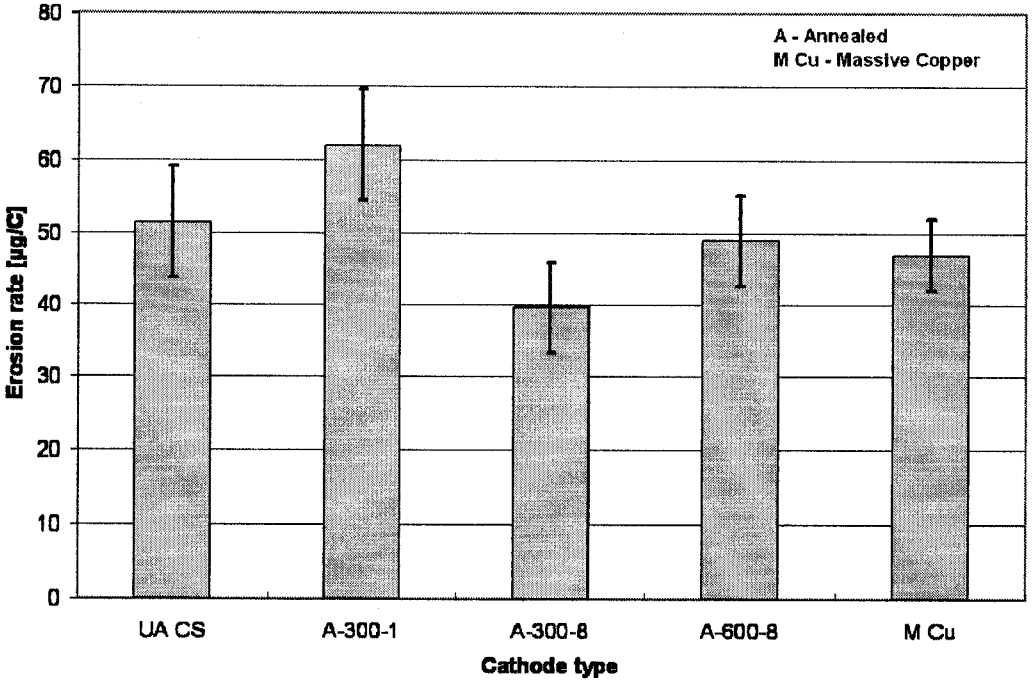

Figure 8.10Average erosion rates for coated and M-Cu cathodes.

a) b)

Figure 8.11 Pictures of the cathode before erosion a) As-sprayed and b) A-600-8 cathodes before erosion. Notice the swelling of the coating after annealing at 600 °C for 8 hours.

To test the effect of annealing, CS coatings were annealed at 300 and 600 ^{0}C for 1 hr and 8 hr duration. Annealing at 600 ^{0}C for 8 hrs caused swelling of the coating and blister formation on the cathodes, as shown in figure 8.11. We believe that gases trapped in the pores of the coating caused blistering upon annealing. Blistering was only observed for A-600-8 case.

Figure 8.12 shows the annealed cathodes after 4 min of arcing. As can be seen from figure 8.12, all coatings except A-600-1 coatings spalled. Figure 8.10 shows the erosion rates of annealed cathodes. Again, high erosion rates were due to severe spalling of the coatings. The results suggest that annealing at 300 ^{0}C for both 1 and 8 hr do not reduce spalling. Annealing at 600 ^{0}C for 8 hrs caused blistering of the coating, thereby increasing the contact resistance between the coating and substrate. This leads to higher erosion rates. However, cathodes annealed at 600 ^{0}C for 1 hr show low spalling. Hence these coatings were arced for a length of six minutes.

Figure 8.8 shows typical arc velocity results for A-600-1 coatings. The arc velocity for A-600-1 cathodes had one fast steady regime (arc velocity of ~ 43 m/s), unlike M-Cu. A-600-1 cathodes (average grain size of 2.29 μm) differed from M-Cu cathodes (average grain size of 21.5 μm) only in their grain sizes. Hence, the high arc velocity was attributed to the difference in the microstructure of the cathode. These results show a clear effect of microstructure on arc velocity. As a result of a high arc velocity, A-600-1 cathodes had lower erosion rates than M-Cu. These erosion results are presented in figure 8.13. For an arc time of 6 minutes, the average erosion rate for A-600-1 cathodes was 21.92 ± 5.38 μg/C, which is 35% lower than that of M-Cu.

From figures 8.4 and 8.8, it is clear that even though A-600-1 cathodes had larger grain sizes than as-sprayed cathodes, they had higher arc velocities. This contradicts the argument that small grain sizes result in high arc velocities. However, on paying close attention to figure 8.8, one can observe large fluctuations in the arc velocity for as-sprayed cathodes, from 10 m/s to levels reported for A-600-1 cathodes. This leads us to believe that as-sprayed cathodes do have high arc rotation velocities, which cannot be

reached due to spalling of the coating (shown in figure 8.12). The heat treatment applied to A-600-1 cathodes improved inter-splat and coating-substrate adhesion and hence, prevented spalling and maintained high arc velocities.

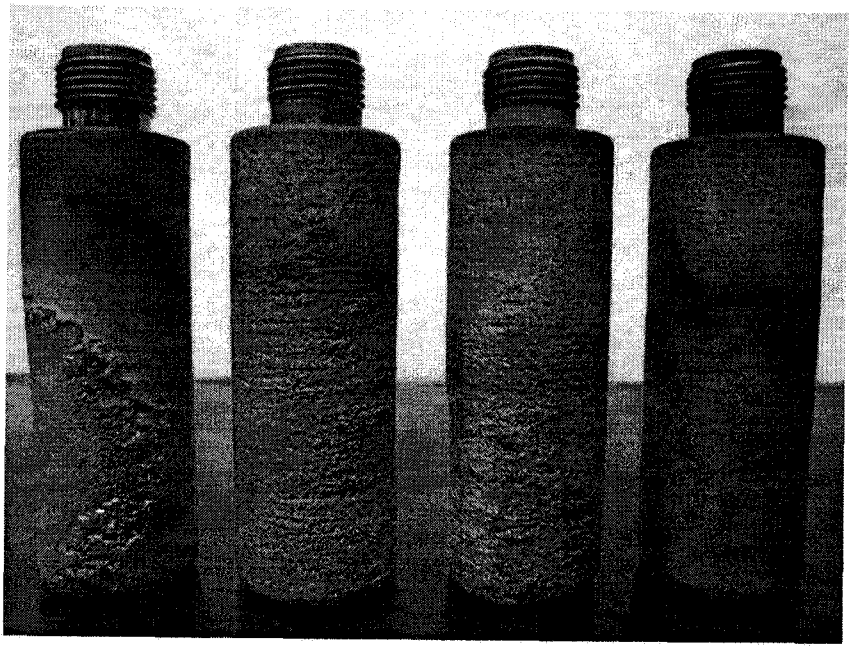

Figure 8.12 Pictures of the cathode after erosion a) As-sprayed, b) A-300-1, c) A-300-8 and d) A-600-1. Notice the spalling on all cathodes except A-600-1.

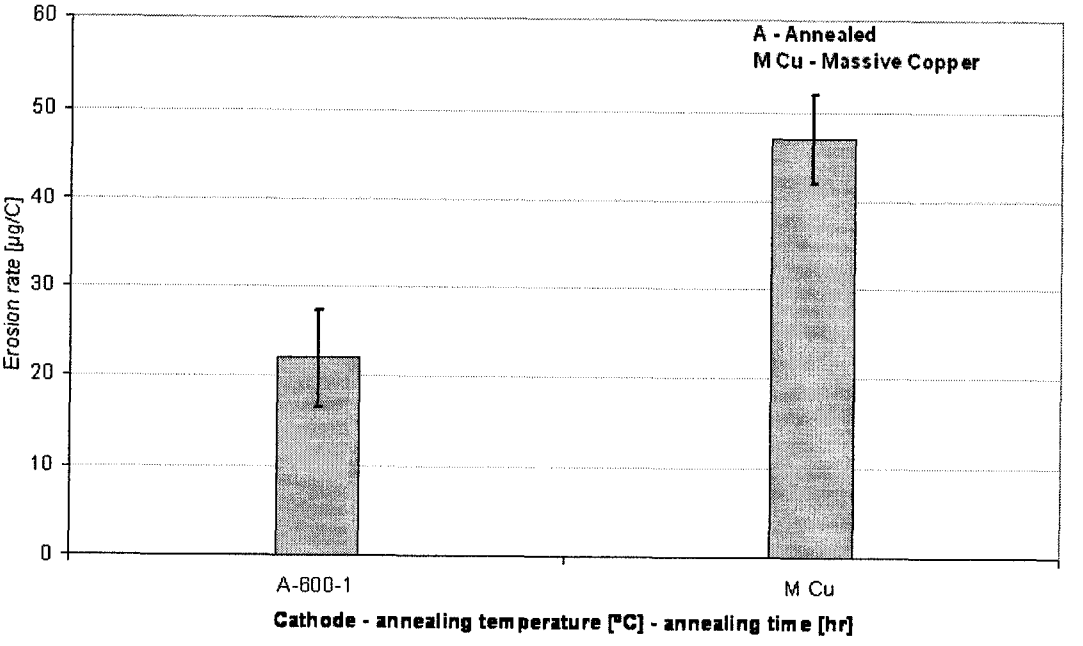

Figure 8.13Average erosion rates for M-Cu and A-600-1 cathodes.

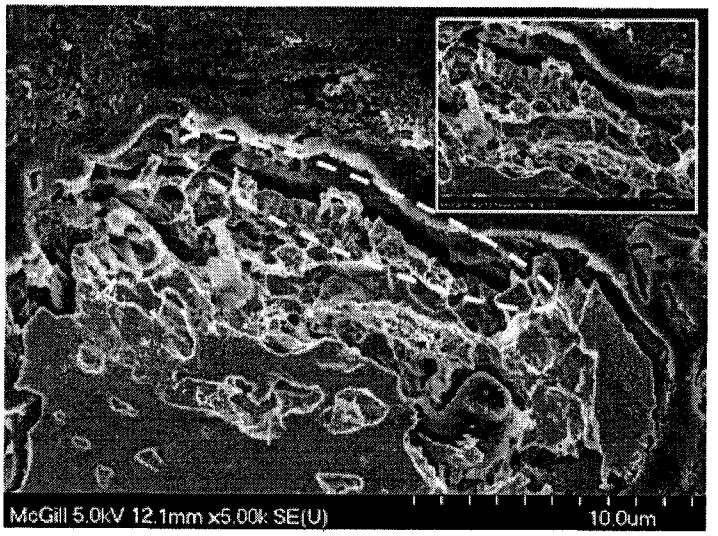

Figure 8.14 Etched cross-section of an eroded, as-sprayed coating. The highlighted area shows an arced region.

8.3.5 Characterization of eroded cathodes

SEM analysis of cold-sprayed cathodes showed no changes in grain sizes in the bulk of the coatings. Hence, the same grain sizes as those given in figure 8.4 were measured for eroded cathodes as well. However, only a thin layer in the outmost splats, which came in direct contact with the arc showed smaller grains, indicating melting and rapid solidification. Figure 8.14 shows an outmost splat of an eroded A-600-1 coating. This region contains smaller grains than bulk of the coating. Since the bulk of the coating was unaffected by arcing, it was concluded that the initial microstructure was preserved even after erosion experiments.

8.4 Conclusions

Cold-sprayed cathodes were tested in a continuous arc chamber to study the effect of microstructure on erosion. The analysis of the coatings formed show that CS cathodes had insignificant oxide content and hence, could be used to isolate the effect of microstructure on erosion. Arc velocities on CS-as-sprayed coatings were fluctuating and spalling is believed to be the reason for such fluctuations in arc velocity. CS cathodes

annealed at 600 °C for 1 hr gave low erosion rates due to their improved transport properties and metallic bonding. These cathodes which had smaller grains than M-Cu gave higher arc velocities and lower erosion rates.

The results show a clear effect of cathode microstructure on erosion behaviour of cold cathodes. We conclude that the microstructure of the cathode affects the arc rotation velocity in a magnetically driven atmospheric pressure arc system. Having grain size distribution in the submicron and/or nanometric range results in higher arc velocities and hence gives lower erosion rates.

8.5 Acknowledgements

The authors would like to thank Dr. Christian Moreau and Dr. Jean-Gabriel Legoux of IMI, Montreal, Canada, for producing the coatings and providing valuable knowledge on the subject matter, and the EUL funds for their financial support.

8.6 References

[1] R. N. Szente, R. J. Munz and M. G. Drouet, Electrode erosion in plasma torches, *Plasma Chem. Plasma Proc.*, 1992, 12 (3), p 327-343, in English

[2] P. Fauchais, A. Vardelle, Thermal Plasmas, *IEEE Trans. Plasma Sci.*, 1997, 25 (6), p 1258-1280, in English

[3] R. N. Szente, R. J. Munz and M. G. Drouet, The Effect of Low Concentrations of a Polyatomic Gas in Argon on Erosion on Copper Cathodes in a Magnetically Rotated Arc, *Plasma Chem. Plasma Proc.*, 1987, 7 (3), p 349-364, in English

[4] P. Tsantrizos, W. H. Gauvin, Cathode Erosion Phenomena In a Transferred-Arc Plasma Reactor, *Plasma Chem. Plasma Proc.*, 1992, 12 (1), p 17-33, in English

[5] J. E. Harry, The Measurement of the Erosion Rate at the Electrodes of an Arc Rotated by a Transverse Magnetic Field, *J. Appl. Phys.*, 1969, 40 (1), p 265-270, in English

[6] L. Rao, R. J. Munz and J. Meunier, Vacuum Arc Velocity and Erosion Rate Measurements, *J. Phys. D: Appl. Phys.*, 2007, 40 (14), p 4192-4201, in English

[7] C. Zhang, Z. Yang, Y. Wang, B. Ding, Cathode Spot Propagation on the Surface of Amorphous, Nanocrystalline and Crystalline $Cu_{60}Zr_{28}Ti_{12}$ Cathodes, *Phys. Lett. A*, 2003, 318 (4), p 435-439, in English

[8] R. N. Szente, R. J. Munz and M. G. Drouet, Cathode Erosion in Inert Gases: The Importance of Electrode Contamination, *Plasma Chem. Plasma Proc.*, 1989, 9 (1), p 121-132, in English

[9] F. Gartner, T. Stoltenhoff, J. Voyer, H. Kreye, S. Riekehr and M. Koçak, Mechanical Properties of Cold-sprayed and Thermally Sprayed Copper Coatings, *Surf. Coat. Technol.*, 2006, 200 (24), p 6770-6782, in English

[10] L. Rao, Chapter 6, *Effect of Cathode Microstructure on Erosion of Copper Cathodes – An Experimental Study*, McGill University, Montreal, Quebec, Canada, 2007

[11] W. Li, C. Li and H. Liao, Effect of Annealing Treatment on the Microstructure and Properties of Cold-sprayed Cu Coating, *J. Therm. Spray Technol.*, 2006, 15 (2), p 206-211. in English

[12] L. Rao, Chapter 7, Effect of cathode microstructure on erosion of copper cathodes-an experimental study, McGill Univerisity, Montreal, Canada.

Chapter 9 Observation of atmospheric pressure arc on cold cathode

In this chapter the arc attachment and rotational behavior of atmospheric pressure arcs on copper cathodes is presented. High temporal and high spatial resolution high speed camera pictures show how arc root attachment changes with arcing time. The clear evidence of arc root alignment with B-field can be seen from the high speed movies. The arc rotational velocity and the arc voltage data are correlated.

Abstract

Pictures of the atmospheric pressure arc between two concentric copper electrodes at different external magnetic fields (B-field) were taken using a charge-coupled device camera (CCD-C) and a complementary metal–oxide–semiconductor camera (CMOS-C). Pictures reveal, splitting of the arc column into a column with multiple arc roots (i.e. cathode spots), repulsion of cathode spots due to their self-induced B-fields, and grouping of cathode spots under the influence of B-field. Power frequency spectra analysis of the voltage fluctuations was also performed.

9.1 Introduction

The cathode region is the most active and complex part of an electric arc. Efforts to understand arc root attachment and movement on the cathode have been extensive [1-7]. Cathode spots (an ensemble of a hot surface zone with maximum luminosity and a dense plasma cloud [8]) constitute the attachment points of the arc on cathodes [1]. These spots are small, 50-100 μm diameter, and rapidly moving entities (surface diffusivity of the order of 10^{-3} m^2/s) with smaller internal fragments. Cathode spot movement is known to be two folded: the extinction of the spot followed by the ignition of a next one at a neighboring location [1]. The dying spot contributes to the formation of the next one through the establishment of plasma forming conditions near the cathode surface favoring electron emission and thus, the ignition of a next spot. Their displacement dynamic depends strongly on the cathode material and microstructure, the presence or absence of surface contaminants, the intensity of the applied external magnetic field (B-field) and their mutual influence caused by self-induced magnetic fields.

A considerable amount of optical observations on vacuum arcs [1, 2] are available in the literature. High spatial and/or temporal resolution optical observations of high pressure arcs are scarce due its high luminosity [1]. Under high pressure conditions, the mode of arc attachment on the cathode depends heavily on the arc current, cathode material and geometry. Refractory cathodes such as tungsten exhibit two modes of arc attachment: diffuse and constricted, depending on the cathode's ability to maintain thermionic emission conditions over large surface areas or not. On non-refractory cathodes such as iron and copper, the arc attachment is always constricted, independent of the cathode thermal design, and is argued to be similar to vacumm arcs [8]. On non-refractory cathodes, the conditions inside a cathode spot must favor a strong thermo-field emission [9,10] required from the cathode which melts and vaporizes at modest temperatures. Unlike vacuum arcs, in high pressure arcs the nature and movement (dynamics) of a cathode spot are strongly influenced by the ambient gas, since at a certain distance from the spot center, the metal vapor plasma expansion is hindered [1]. In spite of these differences, it is argued that the internal pressure of a vacuum arc spot exceeds the

atmospheric pressure and the basic spot processes such as evaporation and current transfer remain unchanged under high pressure conditions [1].

The motivations for this work were :(i) to collect reliable data on the shape and dynamics of an atmospheric pressure arc moving on a copper cathode under the influence of B-field using high-speed cameras;(ii) to provide evidence for the theories used to explain the atmospheric pressure arc cathode spot dynamics, which are mainly drawn from vacuum arcs observations.

9.2 Experimental methods

Figures 9.1a and 9.1b show a schematic drawing of the setup and an end on picture of the electrodes assembly, whose detailed description is given elsewhere [11]. Concentric electrode geometry with a water-cooled Cu anode centered within a water-cooled sleeve Cu cathode was used. The anode has a raised portion, shown in Fig. 9.1c, to localize the arc. A current adjustable solenoid was used to obtain different axial B-field in the inter-electrode gap, to force arc rotation in the Amperian direction [11]. The arc was ignited by a high frequency trigger and was powered by a welding power supply. An average power of 4.4 kW (40 V and 110 A) was maintained throughout the experiments. Argon (99.99% pure) was circulated from the lower to the top end of the reactor at a flow rate of 23 slpm under atmospheric pressure.

Just before an experiment, the cathode was cleaned with 5% dilute nitric acid to remove the native oxide layer and was immediately installed into the reactor. Pictures of the arc were taken using a DIACAM-PRO CCD-C and a PCO-1200 HS CMOS-C, both supplied by Optikon Corporation. The CCD-C was used at 10 frames per second (fps) with an exposure time of 10 ns while the CMOS-C was used at 1250 fps with an exposure time of 1μs. The CCD-C pictures were taken under a 0.05 T B-field, while the CMOS-C pictures were taken at 0.01, 0.05, 0.10 and 0.15 T. An unused cathode was used for each B-field setting and two sets of pictures were taken for each cathode. The first set was taken within the first 10-20 s of arc ignition, when the arc was rotating quickly due to the

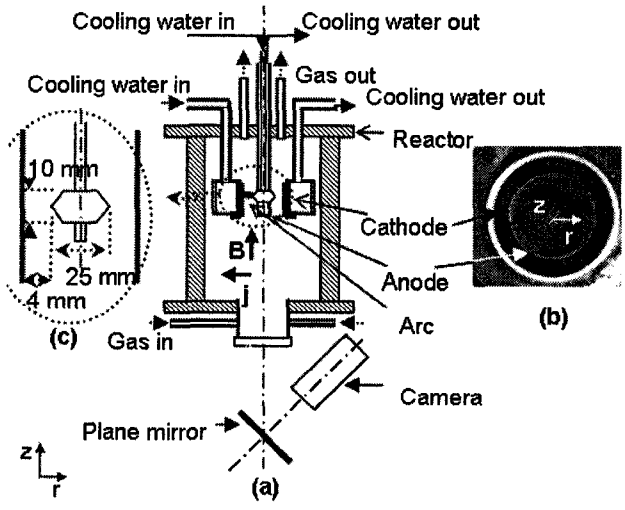

Figure 9.1 a) Schematic of the experimental setup, b) Picture of the electrodes assembly taken with the CCD-C.; end on view, c) Raised portion of the electrode assembly

presence of the thin native oxide layer [12, 13]. The second set was taken ~150 s after arc ignition (referred later as steady state arc condition), when the arc was moving slowly on the cleaned Cu surface, which had lost its native oxide layer due to erosion. From each set of CMOS-C pictures, the rotational arc velocities were calculated. The arc voltage and current waveforms were recorded at 10 kHz sampling rate and analyzed.

9.3 Results and discussion

Figure 9.2 shows CCD-C pictures of the arc taken with 10 ns exposure time at 10 fps. The direction of arc rotation was clockwise. The time when the picture was taken, rounded to the first decimal place, is shown in the inset. An analysis of the pictures suggests that, at ignition when the cathode is at room temperature, the arc starts off as a thin discharge of spoke-like shape as shown in Fig. 9.2a. With arcing time, the arc starts to expand both in length and thickness as shown in Fig. 9.2b and the arc attachment at the cathode covers a large surface area by stretching in the Amperian direction. We hypothesize that, with arcing time, the local temperature of the cathode increases and this local heating facilitates attachment over a larger surface area of the cathode surface. The

stretching in the Amperian direction, confirms that the magnetic force acting on the arc column overcomes the local displacement forces which lead to a retrograde motion under vacuum [2]. With increasing time, the single root attachment splits into several attachment points or arc roots, as evidenced with Fig. 9.2c-e. Siemroth et al [7] reported that, for vacuum arcs on pure Cu cathodes, the mean lifetime of the cathode sub-spots is about 3 μs. Since the CCD-C pictures were taken with an exposure time of 10 ns, we believe that the bright spots appearing clearly in Fig. 9.2c-e are individual arc roots, and not the images of the single arc root moving in a time interval of 10 ns. This phenomena of splitting of a single arc column into a column with many roots (arc splitting) is reported earlier for vacuum arcs [1,3-8] and has been extended to high pressure arcs [14] without direct experimental evidence. Here, we report experimental evidence for arc splitting for high pressure arcs.

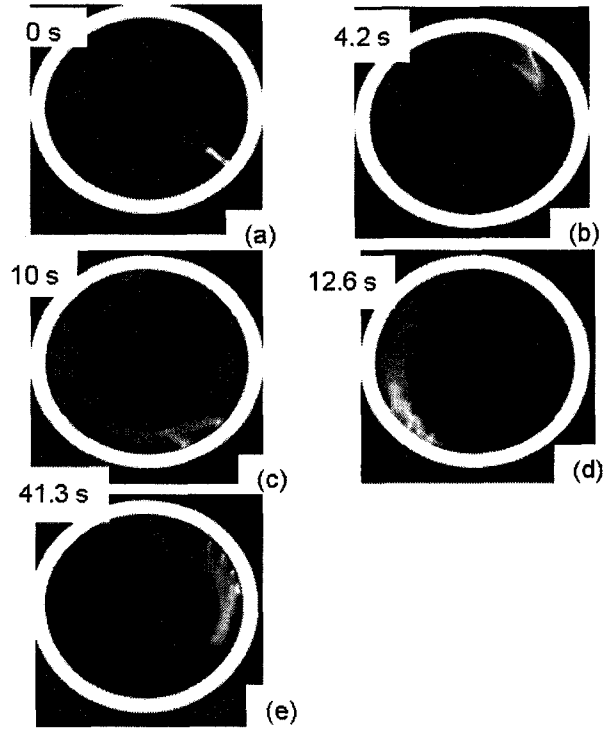

Figure 9.2 a) to e) CCD-C pictures of the arc; end on view. Exposure time =10 ns. Inset shows time of picture. The direction of arc rotation is clockwise.

Figure 9.3 shows a set of typical pictures of the arc taken with the CMOS-C at different B-field values under steady state operating conditions of the arc. Figs. 9.3a-d correspond to B-field values of 0.01, 0.05, 0.10 and 0.15 T, respectively. At lower B-field values, the arc is expanded into a fat column, whereas at higher B-field values the arc is constricted and appears more spoke-like. From the pictures we believe that, at higher B-field values, the arc roots align in the direction of the B-field (in the **z** direction) and hence, the arc appears as a spoke-like discharge when viewed end on. This is similar to the observations made by Drouet [15], who has shown alignment of vacuum arc cathode spots along the B-field. Also from Fig. 9.3, we can see that the arc splitting is more apparent at lower B-fields than at higher B-fields.

It is proven with vacuum arcs that the cathode macro-spots comprise of micro-spots and that these sub-spots repel each other due to their self-induced B-fields. Sherman et al [6] showed that when a high-current vacuum arc is ignited, the numerous cathode spots, originally created over a small area of the cathode surface, move radially outwards. We observed a similar behavior with the high-pressure arc system. Figures 9.4a-c shows a series of pictures taken by the CMOS-C at 0.01 T B-field. We see that the arc column, which started to split into a column with many arc roots (Fig. 9.4a), has displaced into a next attachment (Fig. 9.4b), with the arc roots clearly separated. The two successive pictures of Fig. 9.4b and 9.4c show that the arc roots move away from one another and appear to repel one another. We conclude that, a fat arc column with single arc root splits into a column with many arc roots while moving from one attachment site to the next. During subsequent re-attachments, these multiple arc roots repel one another and attach as an arc with separated roots i.e., the newly ignited macro-spot has arc roots that are more spread apart than the previous one.

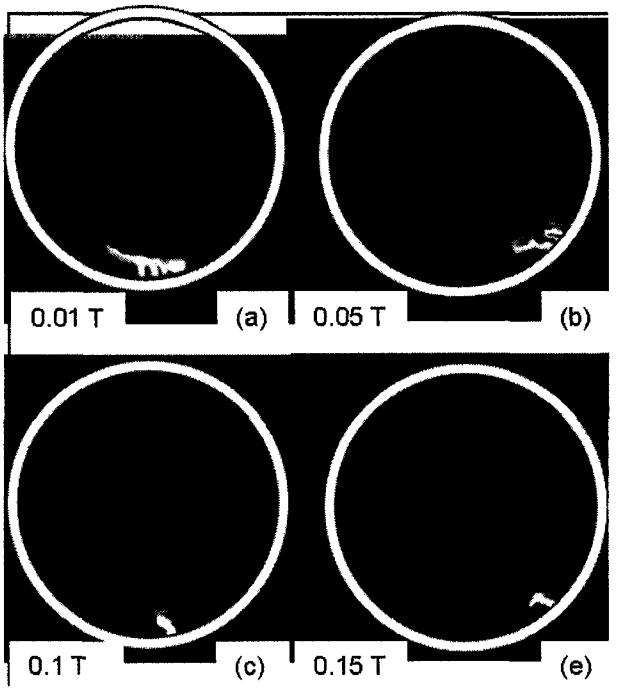

Figure 9.3 a) to e) Typical CMOS-C pictures of the arc under steady state operating conditions; end on view. exposure time = 1 μs. Inset shows B-field The direction of arc rotation is clockwise.

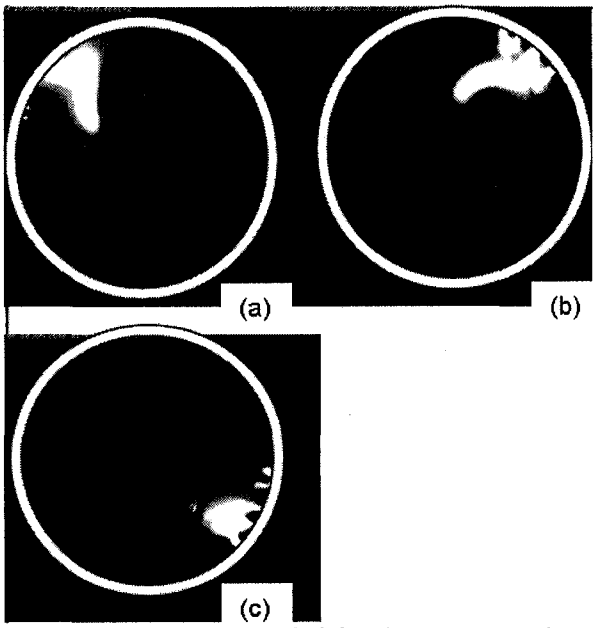

Figure 9.4 a) to e) A series of CMOS-C pictures; 1250 fps, 1 μs exposure time; end on view. B-field = 0.01T. Notice the separation of the arc roots from a) to c). The direction of arc rotation is clockwise.

All experiments were conducted at constant power setting and the arc voltage, further referred to as V, and the arc current, further referred to as I, were recorded. For all cases,

the mean arc voltage and arc current were constant. The mean arc voltage varied dominantly with the arc rotational velocity. In contrast to a slow moving arc (arc velocity ~2 m/s) which is sustained at a relatively low mean arc voltage (~40 V), a fast moving arc (arc velocity ~12 m/s), operated at a higher mean arc voltage (~65 V). This increase in the mean arc voltage at higher arc velocities is attributed to the higher convective heat losses of the arc plasma.

The fast Fourier transforms (FFT) of both the V and I signals were computed and the frequency power spectra (FPS) was obtained. For all B-field cases, the FPS for the current signal showed a unique characteristic frequency component at 331 Hz proving that the 331 Hz is a characteristic of the power supply but not of the arc itself. Figure 9.5a and 9.5b shows the normalized I and V signals and the FPS of the V signal for 0.15T B-field. Except for B=0.01 T, similar single dominant frequency characteristics were seen for all other cases. From Fig. 9.5b an FPS plot at 0.15T, shows a dominant discrete frequency at 42 Hz, in addition to other weak high frequency components. FPS data for B=0.01T,.when plotted on a log-log scale (Fig. 9.5c), showed a $\sim 1/f^2$ characteristic, implying Brownian motion [16,17] Such frequency signature is known as a characteristic of the scaling limit of the random walk dynamics. It is concluded that, in the absence of an external B-field or at low B-field conditions, such as 0.01 T, the cathode spots are left to their inherent displacement characteristics, which are brownian in nature [1]. At higher B-field values, a direction and speed are imposed on the arc movement. CMOS-C pictures corroborate the above conclusion.

For the B = 0.15, 0.10 and 0.05T experiments, the mean arc rotational frequencies calculated by visual observation of the CMOS-C pictures correlate well with the dominant frequencies obtained from the FPS results. These results are tabulated in Table 9.1.

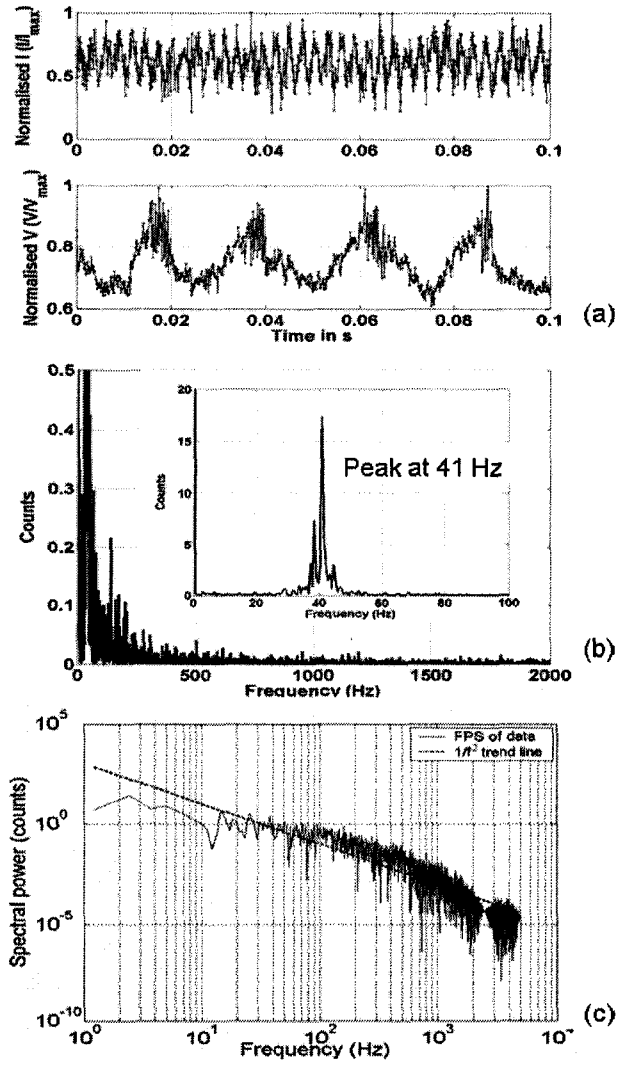

Figure 9.5 a) Normalized I and V data, B = 0.15 T; b) FPS of the V signal, B = 0.15 T; c) FPS of the V signal in log-log scale, B = 0.01 T.

Table 9.1 Arc rotational frequency at different B-field.

B-field (T)	Mean frequency of arc rotation from visual observation of CMOS-C pictures (Hz)	Dominant frequency from the FPS of the V signal (Hz)
0.15	41.6 – 35.6	41.0
0.10	124.8 – 84.1	96.0
0.05	20.8 – 20.1	22.0

9.4 Conclusions

We conclude that: (i) the high-pressure arc column which starts off like a thin spoke-like object with a single arc attachment point on the cathode expands into a fat arc column of irregular shape covering a larger surface area on the cathode as the cathode temperature increases. With arcing time, the single arc column splits into an arc with multiple arc roots at the cathode, which co-exist simultaneously and repel each other during their subsequent re-attachment; (ii) the arc root repulsion is more apparent at lower B-field values. As the magnitude of the B-field increases, the arc attachment area on the cathode becomes smaller;(iii) at low B-field values, the arc displacement dynamics tends to return to its brownian motion, which is a limiting step of the random walk with $1/f^2$ dependency in the FPS. At higher B values, the arc spot displacements become directed, with a FPS showing an unique arc stretching (i.e. arc spot jumping) frequency.

9.5 Acknowledgements

We acknowledge Dr. Philip Servio from the Department of Chemical Engineering, McGill University, for lending us the CMOS-C. The financial support was provided by the Natural Sciences and Engineering Research Council of Canada (NSERC) and McGill University.

9.6 References

1. B. Jüttner, J. Phys. D: Appl. Phys. **34,** R103 (2001) (and reference there in)
2. M. G. Drouet, IEEE Trans. Plasma. Sci. **PS-13**, 235 (1985)
3. B. E. Djakov and B. Jüttner, J. Phys. D: Appl. Phys. **35,** 2570 (2002)
4. K. D. Froome, Proc. Phys. Soc. **B62**, 805 (1949)
5. M. S. Agarwal and R. Holmes, J. Phys. D: Appl. Phys. **17**, 743 (1984)
6. J. C. Sherman, R. Webster, J. E. Jenkins, and R. Holmes, J. Phys. D: Appl. Phys. **8**, 696 (1975)
7. P. Siemroth, T. Schulke and T. Witke IEEE Trans. Plasma. Sci. **PS-23**, 919 (1985)
8. B Jüttner, IEEE Trans. Plasma. Sci. **PS-15**, 474 (1987)
9. E.L. Murphy and R.H. Good, Phys. Rev. **102**, 1465 (1956).
10. G. Ecker Ergebn. Exackt. Naturw. **33**, 1 (1955).
11. R. N. Szente, R. J. Munz and M. G. Drouet, Plasma Chem. and Plasma Process. **7**, 349 (1992)
12. A.E. Guile and A.H. Hitchcock, Proc. IEE **124**, 148 (1977).
13. R.N. Szente, R.J. Munz and M.G. Drouet Plasma Chem. Plasma Process. **12,** 3 (1992).
14. M. S. Benilov and A. Marotta, J. Phys. D: Appl. Phys. **28**, 1869 (1995)
15. M. G. Drouet Japan J. Appl. Physic. **20,** 10270 (1981)
16. A. Anders E. M. Oks and G. Y. Yushkov, Appl. Phys. Lett. **86**, 211503 (2005)
17. A. Anders, IEEE Trans. Plasma Sci. 33 1456 (2005)

Chapter 10 Carbon nanotubes as nanoparticles collector

This chapter presents applications for nano particles produced in the continuous running atmospheric pressure arc setup. Experimental setup and procedure for growing of carbon nanotubes (CNT) using thermal chemical vapor deposition is presented. A method to use these CNT to capture and characterize nanoparticles is presented. Possible applications of nanoparticles dispersed on CNTs are discussed.

Abstract

This communication reports on a new method for the collection of nanoparticles using carbon nanotubes (CNT) as collecting surfaces, by which the problem of agglomeration of nanoparticles can be circumvented. CNT (10 to 50 nm in diameter, 1 to 10 μm in length) grown by thermal CVD at 923 K in a 7 v/v% C_2H_2 in N_2 mixture on electroless nickel-plated copper transmission electron microscopy (TEM) grids and Monel coupons. These samples were then placed downstream of an arc plasma reactor to collect individual copper nanoparticles (5-30 nm in diameter). It was observed that the Cu nanoparticles preferentially adhere onto CNT and that the macro-particles (diameter > 1 μm), a usual co-product obtained with metal nanoparticles in the arc plasma synthesis, are not collected. Cu-Ni nanoparticles, a catalyst for CNT growth, were deposited on CNT to grow multibranched CNT. CNT-embedded thin films were produced by re-melting the deposited nanoparticles.

10.1 Introduction

The design and development of nanosized components have required the synthesis of nanoparticulate materials (i.e., nanoparticles) having physical, chemical and biological properties tailor made to specific applications. Critical to the technological advances in the production and use of nanoparticles is the development of efficient collection methods enabling the study of individual nanoparticles and agglomerates, particle morphology and chemical composition by high-resolution transmission electron microscopy (TEM) and/or scanning electron microscopy (SEM) coupled with micro-analyzers and atomic force microscopy [Saltiel et. al., 2000].

It is a common laboratory practice to use thin metallic mesh/grids, also known as transmission electron microscopy grids (TEM grids), to collect nanoparticles [Malyavantham et. al., 2004]. In this approach, a TEM grid is exposed to a stream of nanoparticles and some of the nanoparticles adhere to it. In the case where the nanoparticles are electrically-charged (ex. electrostatic precipitation), a bias is applied to the TEM grid to enhance the collection efficiency. Though these collection approaches work, the collection efficiency is very low. Furthermore, because of their high surface energy, nanoparticles tend to agglomerate on the grid making it impossible to analyze individual nanoparticles. Even at very high resolution, it is very cumbersome to distinguish if a particle is thin and dish-like or has a 3-D structure [Saltiel et. al., 2000]. In addition to the above difficulties, the substrate itself (i.e., the TEM grid), hinders elemental chemical analyses such as EDS and XPS, and characteristic peaks of the grid material cannot be avoided in the final EDS spectra.

With their high aspect ratio, high surface area and unique structural, chemical and physical properties, carbon nanotubes (CNT) find applications in molecular electronics and logic circuits, as electrode materials, chemical sensors and catalyst supports (Frackowiak et al., 1999; Barisci et al., 2000; Claye et al., 2000; Kong et al., 2000; Odom et al., 2000; An et al., 2001; Bachtold et al., 2001; Guo & Li., 2004). In this work, we

exploit the surface properties of CNT and metal nanoparticles and propose an efficient method of collecting nanoparticles suspended in a gaseous stream.

10.2 Experimental methods

CNT were grown on nickel-coated TEM copper grids of 300 mesh and on Monel coupons (65% Ni, 35% Cu). The electroless coating technique was used to coat the Ni catalyst on the Cu TEM grids. An all Chloride, alkaline bath having the composition given in Table 10.1 was used as the coating solution.

Table 10.1 Electroless coating solution composition [Parthasaradhy N. V., 1989]

Nickel chloride	45 g
Sodium hypophosphite	11 g
Sodium citrate	100 g
Ammonium chloride	50 g
Water	1 L
pH	8.5 to 9.0
Temperature	363 to 373 K
Ammonium hydroxide	Buffer to increase the pH

TEM grids made of pure Copper, were cleaned with acetone in an ultrasonic bath for 20 min and they were further activated by dipping in a solution of 0.1 g/L Pd and 1 mL 37% HCl before electroless deposition. The electroless coating solution as per Table 10.1 was prepared in a 100 mL glass beaker, heated to 368 K on a hot plate and stirred continuously by a magnetic stirrer. The electroless plating was done for different times (30 to 120 sec). The Ni-coated Cu TEM grids and as-received Monel coupons (1 cm × 1 cm × 0.8 mm) were used as substrates to grow CNT in a tubular furnace by thermal chemical vapor deposition at 923 K. A mixture of 7 v/v% C_2H_2 in N_2 was used as the carbon source. A detailed description of the experimental procedure is given elsewhere [Reddy N.K. et al., 2006].

Copper nanoparticles were produced in an arc evaporation/condensation process whereby the copper cathode of an atmospheric pressure magnetically-driven DC arc is thermally eroded. A detailed description of the plasma reactor is given elsewhere [Szente et al.]. In essence, a dense cloud of metallic vapors is formed at the arc attachment points on the copper cathode (ie. the cathode spots) and rapidly cooled by a stream of inert gas (argon) forcing supersaturation of the metal vapors, and subsequent formation of metal nanoparticles. Figure 10.1 shows a schematic drawing of the arc plasma-based nanoparticle synthesis reactor. The reactor uses a concentric electrode geometry whereby the water-cooled anode is along the centerline while the water-cooled sleeve cathode surrounds it, thus defining an annular gap of 4 mm. A water-cooled magnet which surrounds the electrodes assembly is used to apply an axial magnetic field (0.05 T), forcing the arc into rotation. The DC arc is ignited by a high-frequency trigger pulse and powered by a welding power supply (maximum power and current of 20 kW and 500 A, respectively). An average power of 4.4 kW (40 V and 110 A) was maintained throughout the experiments. Ultrahigh purity (99.99% pure) argon circulated from the lower end of the reactor to the top end at a flow rate of 23 SLPM under atmospheric pressure. The nanoparticles produced from the erosion of the cathode are carried away by the flowing gas and deposit on the water-cooled reactor walls and on the TEM grids or Monel coupons placed downstream, as shown in Fig. 10.1. Nanoparticles were also collected on bare TEM grids for comparison. The plasma reactor was run for 5-6 mins.

The morphology and size of the nanoparticles were characterized by a JEOL JEM- 2011 a transmission electron microscope (TEM) operating at 200 kV and also by Hitachi F-4700 field-effect scanning electron microscope (FESEM), operating in the secondary electron (SE), backscattered electron (BSE) and scanning transmission electron (STEM) modes. Energy Dispersive Spectra (EDS) of the individual particles adhered to the CNT were collected and the elemental composition analyzed.

10.3 Results and Discussion

Figure 10.2a shows a SE image of CNT grown on a Ni-coated TEM grid before the collection of the Cu nanoparticles. From the SE images taken at different locations on the TEM grid we noticed that the growth of CNT is well distributed on the grid (images not shown). The CNT growth onto the metallic mesh extends into the voids between the mesh lines. As CNT grow into the voids of the mesh, the nanoparticles adhere onto CNT.

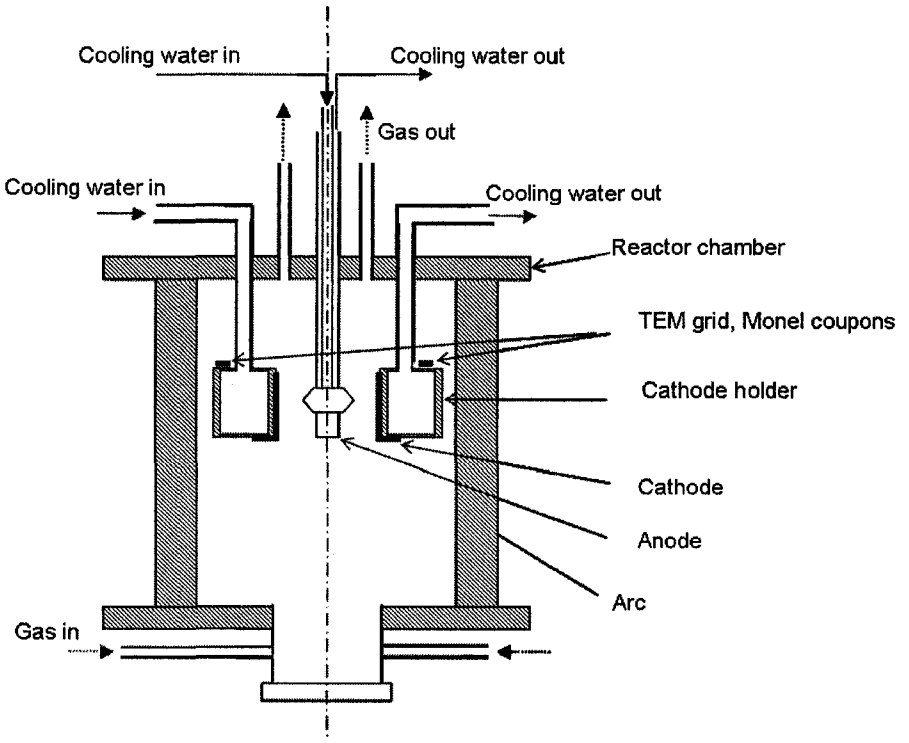

Figure 10.1 Schematic of the magnetically driven arc system.

Figures 10.2b and 10.2c show SE images of copper nanoparticles collected under identical conditions on a bare TEM grid and a TEM grid covered with CNT, respectively. Figures 10.2d and 10.2e are STEM and BSE images of nanoparticles collected on CNT, respectively. Figure 10.2f is a high magnification image of nanoparticles deposited on CNT grown on a Monel substrate. Comparing Fig. 10.2b and 10.2c, it is clear that more nanoparticles are collected on the CNT-covered TEM grids as compared to the bare ones. CNT-covered TEM grids have a larger surface area of collection and also, the surface forces acting between the CNT and the metal nanoparticle aid towards the increased

nanoparticle collection. Due to this combined effect of higher surface area and surface forces, the collection of nanoparticles on CNT-covered TEM grids increases drastically.

As CNT are grown in the voids of the mesh, the imaging of metal nanoparticles under high resolution in different modes (including STEM) and at different angles becomes possible (i.e., it is easy to tilt the specimen and image the nanoparticles at different angles). Figure 10.2d is one such image of nanoparticles obtained in the STEM mode. On a bare TEM grid the nanoparticles sit on the mesh, masking half or more of their surface area from analysis and making the 3-D structure determination difficult. Nanoparticles adhered onto CNT have a much reduced surface area of contact with the collecting surface in comparison with uncovered TEM grids. Hence imaging the nanoparticles at different angles gives more information on its 3-D structure.

In addition to using CNT-covered TEM grids as nanoparticle collectors, CNT grown on Monel coupons were also used to collect nanoparticles (Fig. 10.2f). From Fig. 10.2f, it can be seen that individual nanoparticles are well-distributed along the length of the CNT grown on Monel coupons. Some other researchers refer to this structure as decorated carbon nanotubes [Chen J. et. al., 2006] and self-assemblies of nanoparticles [Shi J. et al., 2006].

Figure 10.3a and 10.3b are the TEM images of the nanoparticles collected on CNT covered TEM grid. From fig 10.3a we see nanoparticles distributed on CNT. Fig 10.3b is a higher magnification image of the same in which individual nano particles (size ranging from 5 to 20 nm) adhered on to CNT can be seen.

Figure 10.4 is an EDS spectrum of nanoparticles deposited on a CNT-covered TEM grid. Characteristic peaks of carbon, oxygen and copper are seen in the EDS spectrum. This confirms the presence of Cu material deposited onto the CNT. Copper, when reduced to the nano-size, readily forms a copper oxide upon exposure to air thus justifying the oxygen peak. It should be noted that in the analysis of this deposit, we have observed less counts per second of X-rays being generated/received by the detector as compared to a

regular EDS analysis (i.e., the dead time of the detector was only 10% instead of being 30%, which is normal for the bulk solid surface). This is attributed to very small interaction volume of the electron beam with the suspended nanoparticles. Because of the low dead time, only qualitative analysis of the particles is possible.

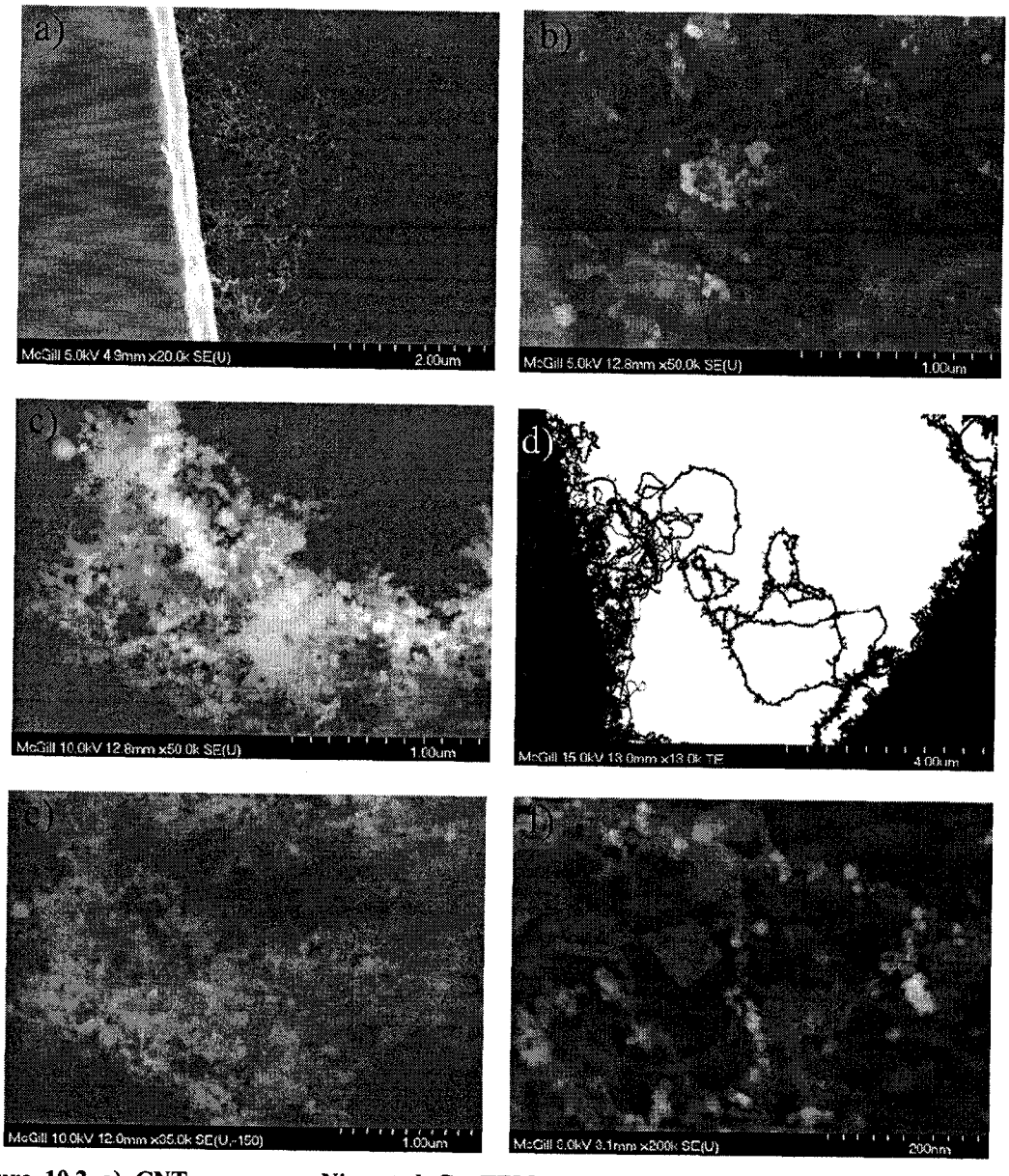

Figure 10.2 a) CNT grown on Ni-coated Cu TEM grid before nanoparticle deposition; b) Cu nanoparticles on bare TEM grid; c) Cu nanoparticles on CNT grown on Ni-coated Cu TEM grid; d) STEM image of nanoparticles on CNT; e) Compositional contrast of nanoparticles; f) High magnification image of nanoparticles on CNT grown on Monel substrate.

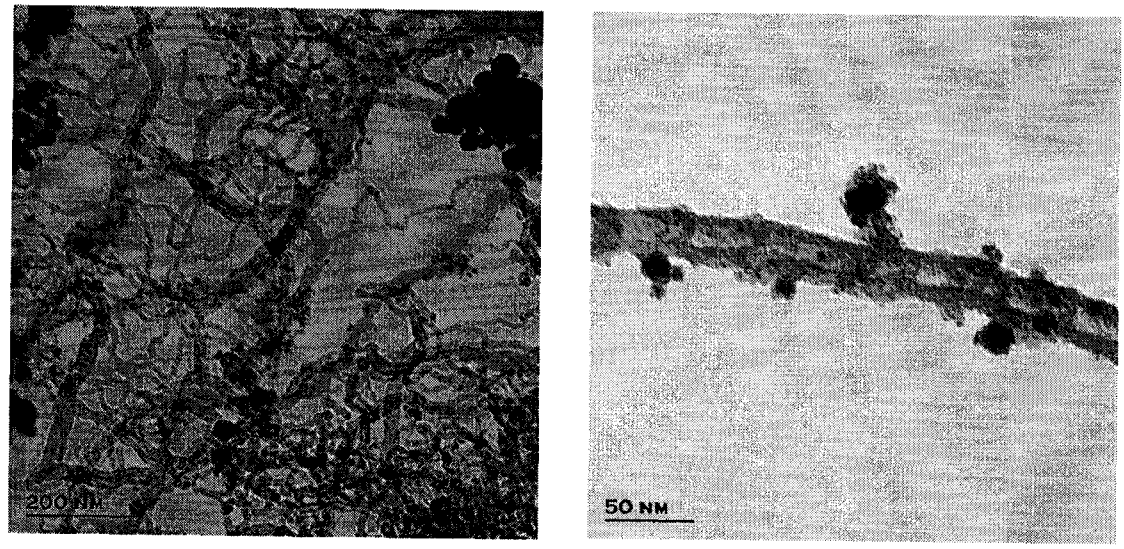

Figure 10.3 a) TEM image of nanoparticles collected on CNT covered TEM grid; b) higher magnification TEM image, showing individual nanoparticles adhered on to the surface of CNT.

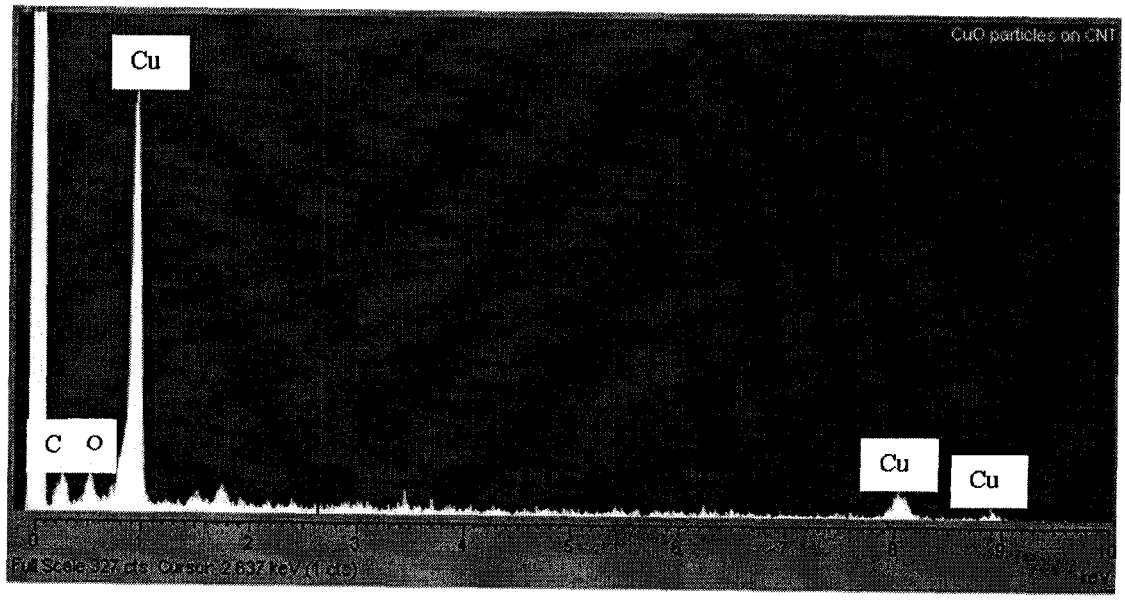

Figure 10.4 EDS spectrum of Cu/Copper oxide nanoparticles on CNTs.

The deposition of nanoparticles onto CNT has many potential applications [Male K.B., et al., 2004]. Depending on the choice of cathode material and plasma gas used with the arc plasma-based nanoparticle synthesis system, nanoparticles of different chemical compositions can be synthesized and deposited onto the CNT. For example, if a Cu-Ni

alloy is used as the cathode material with an inert gas, Cu-Ni nanoparticles can be deposited onto CNT. Such nanoparticles could then be used as catalyst to grow second generation CNT, branching out from the original ones. Figure 10.4 shows a SE image of one such CNT-based structure. The Cu-Ni nanoparticles deposited on the first generation CNT were used as catalysts to grow the second generation of CNT. The new CNT grow on the previous generation CNT, producing a multibranched 3-D structure. Three important planes have been identified on Fig 10.5: plane 'A' is the Monel substrate itself; plane 'B', which is more distant from the surface than plane 'A' hosts the first generation CNT onto which Cu-Ni nanoparticles were deposited. Even further from the surface is plane 'C', where we can recognize second generation CNT which grew onto the first generation CNT, thus creating the multibranched CNT-based structure. The fact that no nanoparticles are attached to those CNT confirms that they are from the second generation.

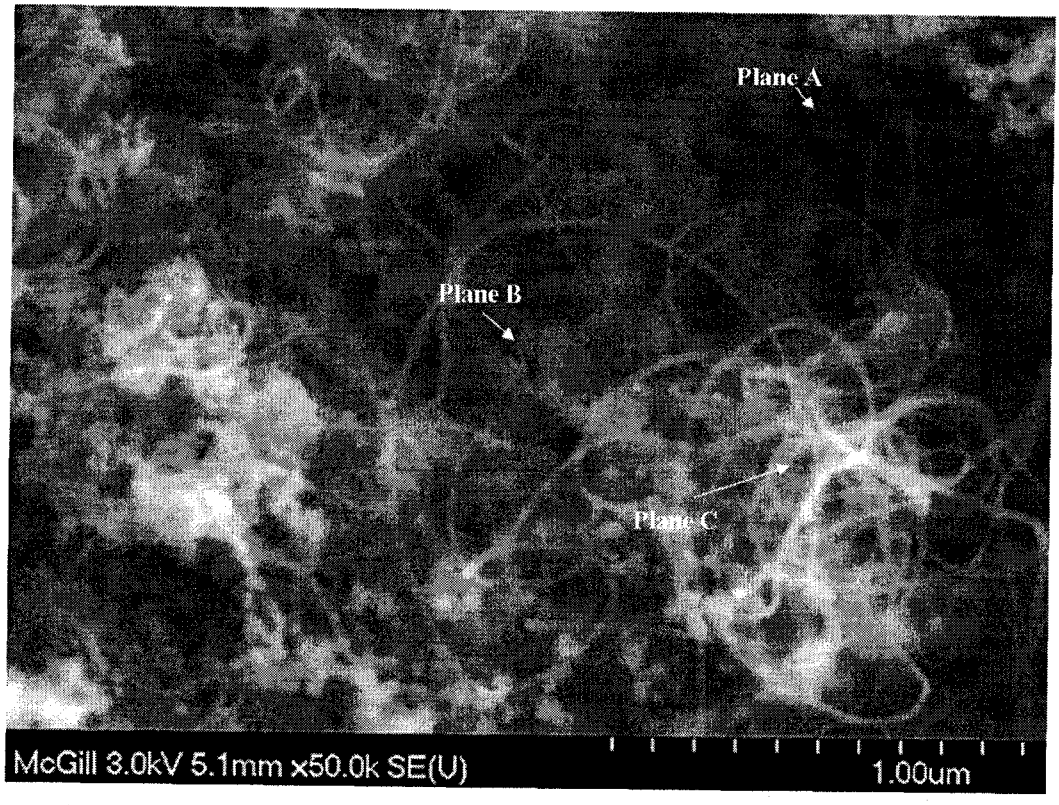

Figure 10.5 Multibranched CNT. Plane A: the Monel substrate; Plane B: the first generation CNT decorated with Cu-Ni nanoparticles; Plane C: the second generation CNT grown on first generation CNT creating a 3-D structure of multibranched CNT.

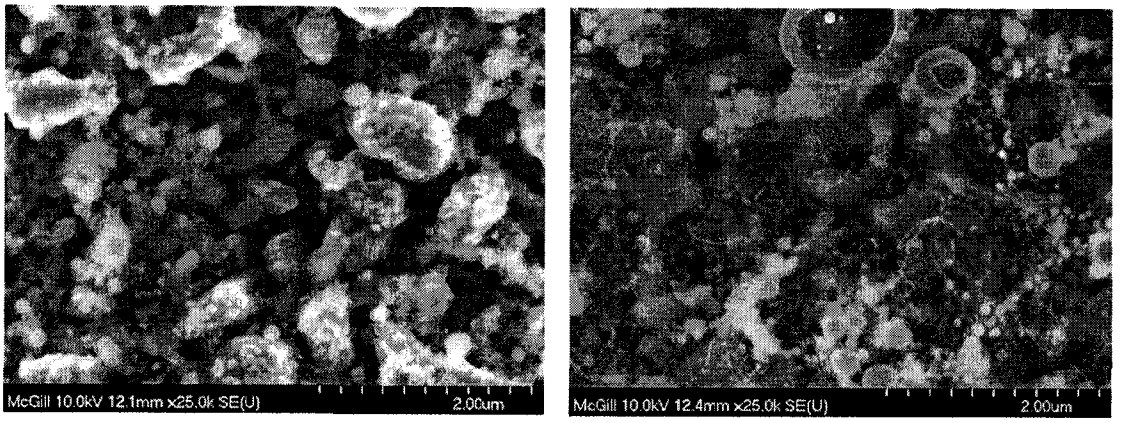

a) b)

Figure 10.6 a) CNT embedded in a porous matrix of copper/copper-oxide film. Notice clusters of nanoparticles which melted and coalesced to form a porous matrix. b) CNT visible inside the porous matrix.

If a sufficient amount of nanoparticles are collected on the CNT grown on the metal catalyst substrate, it is then possible to coat these CNT with nanoparticles and embed them in a thin film of metal/metal-oxide, by further heat-treating the deposited nanoparticles. One such experiment was conducted in which a considerable amount of copper/copper-oxide nanoparticles were deposited on CNT grown on Monel substrate, and further heated to 923 K in a tubular furnace for 45 minutes under N_2 atmosphere. We have observed that the deposited copper/copper-oxide nanoparticles melt at 923 K, which is well below the melting temperature of pure (bulk) copper and copper oxide (1357.8 K and 1508-1599 K, respectively). For Cu-O system no eutectic below 1508 K has been reported in literature. Upon melting, a film containing embedded CNT is produced. Figures 10.6a and 10.6b present SE images of such film. From Fig. 10.6a we observe that the film formed is quite porous. Fig. 10.6b clearly reveals the CNT embedded into the film. A profilometric analysis of the film surface using a DEKTAK[3] profilometer revealed that the film has a mean thickness of 6 μm.

10.4 Conclusions

From the results presented in this communication, it can be concluded that CNT grown on metal substrates can be used as efficient metal nanoparticles collector, thus facilitating their morphological and chemical analyses. The growth of CNT by thermal CVD on Ni-coated Cu TEM grids and Monel coupons is a fairly simple and cheap process, requiring modest equipments. Furthermore, different metal catalyst nanoparticles can be deposited onto CNT for various applications, including the growth of multibranched CNT creating 3-D structures. CNT can also be embedded into metal matrix to form nanocomposite thin films.

10.5 References

1. An K.H., W.S. Kim, Y.S. Park, Y.C. Choi, S.M. Lee and D.C. Chung, et al., 2001. Supercapacitors using single-walled carbon nanotube electrodes. Adv. Mater. 13(7), 497–500.
2. Bachtold A., P. Hadley, T. Nakanishi and C. Dekker, 2001. Logic circuits with carbon nanotube transistors. Science 294, 1317–1320.
3. Barisci J.N., G.G. Wallace & R.H. Baughman, 2000. Electrochemical studies of single-wall carbon nanotubes in aqueous solutions. J. Electro anal. Chem. 488(2), 92–98.
4. Chen J. and G. Lu. 2006. Controlled decoration of carbon nanotubes with nanoparticles. Nanotechnology 17. 2891–2894.
5. Claye A.S., J.E. Fischer, C.B. Huffman, A.G. Rinzler and R.E. Smalley, 2000. Solid-State electrochemistry of the Li single wall carbon nanotube system. J. Electrochem. Soc. 147(8), 2845–2852.
6. Frackowiak E., S. Gautier, H. Gaucher, S. Bonnamy and F. Beguin, 1999. Electrochemical storage of lithium in multiwalled carbon nanotubes. Carbon 37(1), 61–69.
7. Guo D.J. and H.L. Li, 2004. High dispersion and electro catalytic properties of Pt nanoparticles on SWNT bundles. J. Electro anal. Chem. 573(1), 197–202.
8. Kong J., N.R. Franklin, C. Zhou, M.G. Chapline, S. Peng and K.Cho, et al., 2000. Nanotube molecular wires as chemical sensors. Science 287, 622–625.
9. Male K. B., S. Hrapovic, Y. Liu, D. Wang and J. H.T. Luong. 2004. Electrochemical detection of carbohydrates using copper nanoparticles and carbon nanotubes. Analytica Chimica Acta 516. 35–41.
10. Malyavantham Gokul, D. T. O'Brien, M. F. Becker, J. W. Keto and D. Kovar. 2004. Au–Cu nanoparticles produced by laser ablation of mixtures of Au and Cu microparticles. Journal of Nanoparticle Research 6. 661-664.
11. Odom T.W., J.L. Huang, P. Kim and C.M. Lieber, 2000.Structure and electronic properties of carbon nanotubes. J. Phys. Chem. B 104(13), 2794–2809.

12. Parthasaradhy N.V. 1989. Practical electroplating handbook. Englewood Cliffs, N.J. Prentice Hall
13. Reddy N.K., J.L. Meunier and S. Coulombe. 2006. Growth of carbon nanotubes directly on a nickel surface by thermal CVD. Materials Letters. In press, corrected proof.
14. Saltiel Craig and H. Giesche., 2000. Needs and opportunities for nanoparticle characterization. Journal of Nanoparticle Research **2.** 325–326.
15. Shi J., Z. Wang and H. Li. 2006. Selfassembly of gold nanoparticles onto the surface of multiwall carbon nanotubes functionalized with mercaptobenzene moieties. Journal of Nanoparticle Research.
16. Szente. R. N., R. J. Munz and M. G. Drouet. 1992. The effect of low concentrations of a polyatomic gas in argon on erosion on copper cathodes in a magnetically rotated arc. Plasma Chemistry and Plasma Processing 7. 349–364.

Chpter 11 Conclusions

This chapter summarizes the conclusions from this study. All the thesis objectives were achieved.

The most relevant conclusions in this study are the following:

11.1 Vacuum arc experiments-conclusions

1 Both surface roughness and surface patterns affect the erosion rates. Reducing surface roughness reduce erosion rates. Cathodes with perpendicular patterns give lower erosion rates due to a broader arc attachment. This results in reduced local heating and better heat dissipation on the cathode surface.

2 Erosion rates depend chiefly on the nature of arc attachment and arc movement on the cathode. At any roughness level, having regular patterns in the direction of arc movement, results in overlapping craters and higher erosion rates. Isotropic surfaces promote random motion and hence give lower erosion rates.

3 Nanostructured coatings produced by plasma spraying (PS) and high velocity oxygen fuel spraying (HVOF) methods have 100 to 300 nm grain sizes and ~2 atomic % intersplat oxygen content. These coatings give up to 50% lower erosion rates relative to massive Cu having relatively larger grains. Coatings preserve their initial nanostructure even after passing as many as 135 arc pulses, each of which was 500 μs long at an arc current of 125 A

11.2 Atmospheric arc experiments-conclusions

1 Hard drawn electrodes having smaller grain sizes (6 ± 1 μm) in the direction perpendicular to the direction of drawing and arc motion showed 16% lower

erosion rates than fully annealed electrodes with equi-axed grains (21 ± 2 μm). The results demonstrate an effect of grain size on erosion rate.

2 HVOF coatings and cold sprayed coatings in their as-sprayed state with average grain sizes of 300 nm and 1.12 μm respectively, showed higher arc velocities due to their reduced grain sizes. Although the velocities were higher, the erosion rates were also higher due to severe spalling of the coatings. These coatings spalled as their electrical and thermal conductivity were lower than massive Cu.

3 Annealing these coatings is known to increase the coating strength as well as their electrical and thermal conductivities. Even though these properties come at the expense of some grain growth, annealed HVOF and CS coatings having 2-4 μm grains gave up to 60% higher steady state arc velocities and up to 68% lower erosion rates compared to massive copper cathodes having 20 to 23 μm average grain size.

4 Vacuum plasma spray (VPS) coatings having 0.9 to 1.5 μm average grain size gave up to 60% higher arc velocities and up to 70% lower erosion rates when compared to massive copper cathodes.

5 VPS coatings and cold sprayed coatings were free from oxygen content and hence clearly isolated the effect of microstructure alone. Both of these coatings had smaller grains and showed lower erosion rates than massive Cu.

6 The initial microstructure of the coatings remained intact after erosion experiments.

11.3 Peripheral work-conclusions

1. High temporal and spatial resolution pictures of the atmospheric pressure magnetically rotated arcs reveal, splitting of the arc column into a column

with multiple arc roots (i.e., cathode spots), repulsion of cathode spots due to their self-induced B-fields and grouping of cathode spots under the influence of external B-field.

2. Carbon nanotubes grown on metal substrates are efficient metal nano-particle collectors. In addition to nano particle collection, carbon nanotubes also facilitate morphological and chemical analyses of nanoparticles.

11.4 Original contributions

The most relevant original contributions in this study are listed below:

The most relevant original contributions in this study are listed below:

- Quantitative and qualitative correlation of cathode microstructure, surface roughness/pattern with vacuum and atmospheric pressure arc velocities, and arc erosion rates.

- Characterization of thermal and cold spray coatings for their thermal properties and grain size measurements pre/post erosion experiments.

- Developing a better understanding of the atmospheric pressure arc, its attachment and arc movement, on copper cathodes using high speed, high resolution cameras.

- Development of new technique to characterize nanoparticles using nanotubes.

Chpter 12 Future work and recommendations

The following two future works are proposed:

12.1 Erosion studies on VPS coatings-experimental work

VPS coatings showed up to 60 % higher arc velocities and 70 % lower erosion rates and remained intact even after 10 minutes of arcing at a 6 kW power setting. These results were obtained for a B-field setting of 0.10T, and a gas flow rate of 23 slpm. More experiments should be performed on coatings with the following conditions to further determine their erosion behavior

- Keeping all conditions constant, the B-field can be varied from 0.01 T to 0.15 T
- Keeping all conditions constant, the arc current can be varied from 50 A to 250 A
- Run erosion experiment for longer time periods (> 10 minutes) with constant operating conditions.

Developing and testing internally sprayed coatings would be more useful from an industrial point of view. Raymor industries (located at 3765 La Verendrye, Boisbriand, Quebec, J7H 1R8, Canada, and Phone: 1-450-434-1004) produce VPS coatings.

It is proposed to capture high speed and high resolution images of the arc running on VPS coatings using the CCD camera available with Dr. Meunier and CMOS camera available with Dr. Servio. These images would reveal precise information on arc attachment and arc movement on cathodes having smaller grain sizes.

12.2 Erosion studies on cathodes formed from nano powders-experimental work

To further understand the effect of microstructure on arc velocity and arc erosion, it is proposed to conduct erosion studies on cathodes formed from nano powders. These cathodes would be formed entirely using nano powders and is expected to have better thermal and electrical properties.

Dr. M. Brochu of the Department of Mining and Materials Engineering Mcgill has expertise on forming solid rods and coupons starting from nanopowders using the explosive bonding technique. He has also facilities for cryogenic milling. It is hypothesized that cathodes formed by explosion forming methods starting from cryo-milled pure copper powders having nanometric grains give lower erosion rates because of enhanced arc velocities.